2021

Photonic quantum information processing based on directionally-unbiased linear-optical multiports

BOSTON UNIVERSITY

COLLEGE OF ENGINEERING

Dissertation

PHOTONIC QUANTUM INFORMATION PROCESSING BASED ON DIRECTIONALLY-UNBIASED LINEAR-OPTICAL MULTIPORTS

by

SHUTO OSAWA

B.A., Greenville University, 2016
M.S., Boston University, 2020

Submitted in partial fulfillment of the

requirements for the degree of

Doctor of Philosophy

2021

Approved by

First Reader

Alexander V. Sergienko, PhD
Professor of Electrical and Computer Engineering
Professor of Physics

Second Reader

Luca Dal Negro, PhD
Professor of Electrical and Computer Engineering
Professor of Materials Science and Engineering
Professor of Physics

Third Reader

Roberto Paiella, PhD
Professor of Electrical and Computer Engineering
Professor of Materials Science and Engineering

Fourth Reader

Miloš A. Popović, PhD
Associate Professor of Electrical and Computer Engineering

Never try to outstubborn a cat. Robert A. Heinlein

Acknowledgments

My highest gratitude goes to my advisor Professor Alexander Sergienko, whose expertise was invaluable in formulating the research questions and methodology. His continuous support and insightful feedback helped me to sharpen my thinking, and I was able to push my scientific knowledge further.

My gratitude also goes to Professor David Simon who served as my second advisor throughout my grad school career at BU. I am delighted that I was able to participate in both experimental and theoretical quantum information science thanks to my advisors.

I wish to thank the members of my defense committee, Professor Luca Dal Negro, Professor Roberto Paiella, and Professor Miloš Popović. I have learned a great deal in both a classroom setting and general discussions from them.

I would like to acknowledge my colleagues Prof. Gregg Jaeger, Dr. Casey Fitzpatrick, Dr. Andrew Fraine, Dr. Mackenzie Van Camp, Dr. Abu Thomas, Dr. Olga Minaeva, Dr. John Snyder. Guang Yang, Conor Lyons, Anthony Manni, and Zach Furman for having engaging discussions with me.

I would like to thank my friends Yuya Kurohara, Spencer Jaquet, and Xiaotong (Toni) Zheng for bringing me joy all the time.

I am greatful to Dr. Hyung Choi at Greenville University for opening the door for me to start research activities in quantum information science.

I cannot thank my parents and my brother enough for their support of my journey in the US for almost a decade. I would not be able to make it this far without their support and unconditional love.

Many thanks to the Silvia and Wilcox families for all the support I have received before and during the pandemic.

My wife, Serena has been extremely supportive of me throughout my career. I am lucky to have her as my wife, and I am excited to start a new chapter of our life together.

Figure 0·1: Tofu the cat.

Finally, my furball friend Tofu asks for some attention in this acknowledgment. She claims that she contributed to elucidate quantum mechanics and demands a picture to be placed in return.

Shuto Osawa

PHOTONIC QUANTUM INFORMATION PROCESSING BASED ON DIRECTIONALLY-UNBIASED LINEAR-OPTICAL MULTIPORTS

SHUTO OSAWA

Boston University, College of Engineering, 2021

Major Professor: Alexander V. Sergienko, PhD
Professor of Electrical and Computer Engineering
Professor of Physics

ABSTRACT

The progress in modern quantum information processing (QIP) strongly depends on new algorithms and on the development of novel quantum entanglement processing elements enabling to perform quantum computation and quantum simulation effectively. Several examples of quantum information processing applications based on freshly designed linear-optics devices are presented.

A beam splitter (BS) is a central device in linear-optical quantum information processing because it can split the incoming photon amplitudes into spatially distinct modes to establish conditions for quantum superposition. The BS naturally possesses directional-bias in a sense that incoming photons can only propagate in a forward manner. When the execution of certain quantum information tasks would require multiple operations, this directionality condition becomes a serious obstacle by creating significant overhead in the number of needed elements and other supporting devices. We introduce a family of amplitude-controllable fully-reversible linear-optical quantum information processors, called directionally-unbiased linear-optical multiports, in order to achieve significant reduction in the number of required

hardware. The theoretical analysis of the device design as well as the experimental realization of three-port unit using bulk linear optics is demonstrated. These devices offer several fresh approaches in quantum-walk-based applications such as quantum simulation of solid-state Hamiltonians, topological protection of polarization qubits against errors, and quantum communication. Topological photonics is an emerging and actively developing field because of its capability to stabilize and protect some quantum states from perturbation errors by ensuring the environment carries a distinct topological signature. Topology-dependent quantum information processing is globally stable due to the entire system being engaged in the information manipulation. We demonstrate suppression of quantum amplitude transfer between two distinct bulk regions of a system. This results in error avoidance for a two-photon polarization-entangled state under specific conditions.

The goal of modern quantum communication is a reliable distribution of quantum entanglement between multiple nodes performing quantum operations such as quantum memories and quantum computers. We demonstrated that local quantum information processing using new fully-reversible four-port linear-optical structures could find an immediate application in quantum communication. A quantum information routing device is introduced based on the use of four-dimensional Grover matrices and beam splitters. Several multiport-based units are developed to demonstrate new higher-dimensional Hong-Ou-Mandel (HOM) effect and directionally-controllable entangled state distribution while changing only phases in a waveguided unit. Several such operational elements could be linked to form a reconfigurable network of quantum users without losing control of quantum amplitudes. This allows controllable routing of entangled photons and sharing entanglement between any designated users in the future quantum computational networks.

Contents

List of Tables

List of Figures

List of Abbreviations

APD	.....	Avalanche Photodiode
BS	.....	Beam Splitter
CS	.....	Chiral Symmetry
CTQW	.....	Continuous-Time Quantum Walk
DTQW	.....	Discrete-Time Quantum Walk
GHZ	.....	Greenberger-Horne-Zeilinger (state)
H	.....	Horizontal (polarization)
HOM	.....	Hong-Ou-Mandel
KLM	.....	Knill-Laflamme-Milburn (protocol)
MZ	.....	Mach-Zehnder
QW	.....	Quantum Walk
SPDC	.....	Spontaneous Parametric Down Conversion
SSH	.....	Su-Schrieffer–Heeger
V	.....	Vertical (polarization)

Chapter 1

Introduction

1.1 Motivation

A tremendous amount of effort has been devoted to quantum information processing with the ultimate goal of making a quantum computer (Nielsen and Chuang, 2002). Quantum information science is diverse. In fact, multidisciplinary efforts have been incorporated into this area, ranging from physics, computer science, mathematics, and chemistry, among others. Classical systems are simulated through classical computers. Similarly, quantum systems should be simulated through quantum computers rather than classical ones (Feynman, 1982). Though it may seem straightforward to achieve this implementation of a quantum computer task, it faces many hurdles to be overcome.

1. Quantum systems are fragile. Quantum systems do not survive for an extended amount of time. This is because a quantum state couples to an environment and the information becomes inaccessible. This is known as decoherence.

2. Cloning of a state is not allowed. The no-cloning theorem prohibits cloning of an arbitrary quantum state (Wootters and Zurek, 1982). This implies that arbitrary manipulation and amplification of quantum states are difficult to achieve.

3. Entangled state generation. Significant amount of entangled qubits are necessary to achieve computation in a quantum computer. However, this generation of photonic qubits turned out to be a very arduous task. Low number entanglements are readily available nowadays (Kim et al., 2006; Kwiat et al., 1995), yet its robust scaling is an important task to be solved.

To actually implement such a computer, there are several architectures to be selected such as photonics, cold atoms, and superconducting systems, in which quantum information processing can be performed. Both photonics and quantum systems are an exceptional match for performing quantum information processing. This is due to the fact that photons do not suffer from thermal noise, therefore there is no need for extreme cooling for experiments. Even so, photonic systems face difficulties in the stable production of entangled photons, particularly with high photon numbers. This is a result of photons not interacting under linear operations. This indicates that the production of entangled photonic states relies on quadratic effects coming from nonlinear optical devices (Boyd, 2020). Spontaneous parametric down-conversion (SPDC) is often used for two- and three-entangled photonic state generation (Klyshko et al., 1970; Kwiat et al., 1995; Bouwmeester et al., 1999b). However, the generation of entangled photons is probabilistic, meaning one needs to wait for the event to occur. The wait time becomes astronomically longer as the number of entangled photons scales. To circumvent this, linear optical quantum computation has been introduced and measurement-based feed-forward systems attract attention as a result of the shorter waiting period for a desirable event to occur (Knill et al., 2001). The price to pay for needing nonlinear operations is rapidly escalating apparatus size.

This dissertation will focus on quantum information processing using only linear optical devices for state manipulation such as beam splitters, phase shifters, and mirrors. By combining these basic devices, higher-dimensional linear optical multiports can be formed to access higher dimensional quantum states (Reck et al., 1994). Unlike previously introduced multiports, we introduce a new reversible linear optical system by re-using optical elements. This device offers a variety of applications in photonics-based quantum information processing. By combining multiple copies of them, we can form a quantum walk and a state transfer system which is essential for quantum communication (Ekert, 1991; Briegel et al., 1998). In quantum information processing, a quantum state needs to be prepared, propagated, and

then measured. This dissertation tackles the problem of state preparation and distribution utilizing linear optical devices based on quantum walk approaches.

1.2 Structure of This Dissertation

The rest of chapter 1 introduces background knowledge on quantum state manipulation. Chapter 2 introduces basic building blocks used in optics such as interferometers as a quantum information processing tool. Chapter 3 introduces a new type of interferometer based quantum information processor called directionally-unbiased linear-optical multiports by introducing propagation reversibility in the system. The experimental demonstration of the device is originally reported in (Osawa et al., 2018). Theoretical description (Simon et al., 2016) and bulk optics based experimental results are provided to demonstrate its operation. A review of multiple directional and directionally-unbiased devices designs is originally provided in (Osawa et al., 2019). Chapter 4 introduces quantum walks in optics by utilizing both basic linear-optical devices and reversible multiport devices introduced in chapter 3. Chapter 5 introduces topological photonic information processing using reversible devices. Application of directionally-unbiased linear-optical multiports in topological photonics is originally reported in (Simon et al., 2017a; Simon et al., 2017b; Simon et al., 2018a; Simon et al., 2018b). Topological photonics manipulates information in a global manner. Chapter 6 introduces multiphoton quantum state processing based on the combination of multiple multiport devices. This application is originally demonstrated in (Simon et al., 2020; Osawa et al., 2020). In addition to the previous chapter, we also explore a local information processing. Clustering of two photons in quantum walks and transportation of a quantum state is introduced. Chapter 7 summarizes the dissertation and formulates potential future works based on the new effects introduced in previous chapters.

1.3 Quantum Information Processing

To perform computation with the help of quantum mechanics, the classical bits, $|0\rangle$ and $|1\rangle$, are modified to quantum bits known as "Qubit". Qubits are described using unit ket vectors $|0\rangle$ and $|1\rangle$. For a two-mode system, this is analogous to a classical "bit" representation.

$$|0\rangle = \begin{pmatrix} 1 \\ 0 \end{pmatrix}, |1\rangle = \begin{pmatrix} 0 \\ 1 \end{pmatrix}. \tag{1.1}$$

This matrix is not the only choice of basis. Another basis can be used as long as $|0\rangle$ and $|1\rangle$ are orthogonal.

$$|0\rangle = \frac{1}{\sqrt{2}} \begin{pmatrix} 1 \\ 1 \end{pmatrix}, |1\rangle = \frac{1}{\sqrt{2}} \begin{pmatrix} 1 \\ -1 \end{pmatrix} \tag{1.2}$$

can be another choice of a basis.

An obvious qubit is a single qubit state defined as

$$|\psi\rangle = \alpha|0\rangle + \beta|1\rangle, \tag{1.3}$$

where α and β are complex numbers satisfying $|\alpha|^2 + |\beta|^2 = 1$. This state is in a superposition of 0 and 1. The information is revealed when a measurement is performed. The qubit takes the value $|0\rangle$ with probability equal to $|\alpha|^2$ and $|1\rangle$ with probability equal to $|\beta|^2$. Unlike classical bits, we can add a relative phase between the two orthogonal basis of qubits, and this plays an important role in quantum interference. The qubit can be understood geometrically by parametrizing the quantum state using spherical coordinates. Most commonly used parametrized representation of a qubit is,

$$|\psi\rangle = cos\frac{\theta}{2}|0\rangle + e^{i\phi} sin\frac{\theta}{2}|1\rangle. \tag{1.4}$$

This state resides on a sphere and an arbitrary state can be obtained by applying pauli matrices introduced in the next subsection.

1.3.1 Single Qubit Gates

Pauli matrices are defined by

$$\sigma_X = \begin{pmatrix} 0 & 1 \\ 1 & 0 \end{pmatrix}, \sigma_Y = \begin{pmatrix} 0 & -i \\ i & 0 \end{pmatrix}, \sigma_Z = \begin{pmatrix} 1 & 0 \\ 0 & -1 \end{pmatrix}. \tag{1.5}$$

Bloch sphere enables graphical representation of qubits. Single qubit gates work as rotation of a state on the Bloch sphere shown in Fig. 1·1. We can take an arbitrary qubit state $|\psi\rangle = \alpha|0\rangle + \beta|1\rangle$. Rotation with respect to each axes can be performed by applying pauli matrices. Rotation around x-axis is performed by applying pauli-X gate on $|\psi\rangle$. The graphical representation is provided in Fig. 1·1 (a).

$$\sigma_X|\psi\rangle \rightarrow \begin{pmatrix} 0 & 1 \\ 1 & 0 \end{pmatrix}(\alpha|0\rangle + \beta|1\rangle) = \alpha|1\rangle + \beta|0\rangle. \tag{1.6}$$

Pauli-X flips the qubit value from $|0\rangle$ to $|1\rangle$ and $|1\rangle$ to $|0\rangle$. Rotation around z-axis is performed in the following manner. The graphical representation is provided in Fig. 1·1 (b).

$$\sigma_Z|\psi\rangle \rightarrow \begin{pmatrix} 1 & 0 \\ 0 & -1 \end{pmatrix}(\alpha|0\rangle + \beta|1\rangle) = \alpha|0\rangle - \beta|1\rangle. \tag{1.7}$$

This pauli-Z gate flips the phase between two orthogonal basis from +1 to -1.

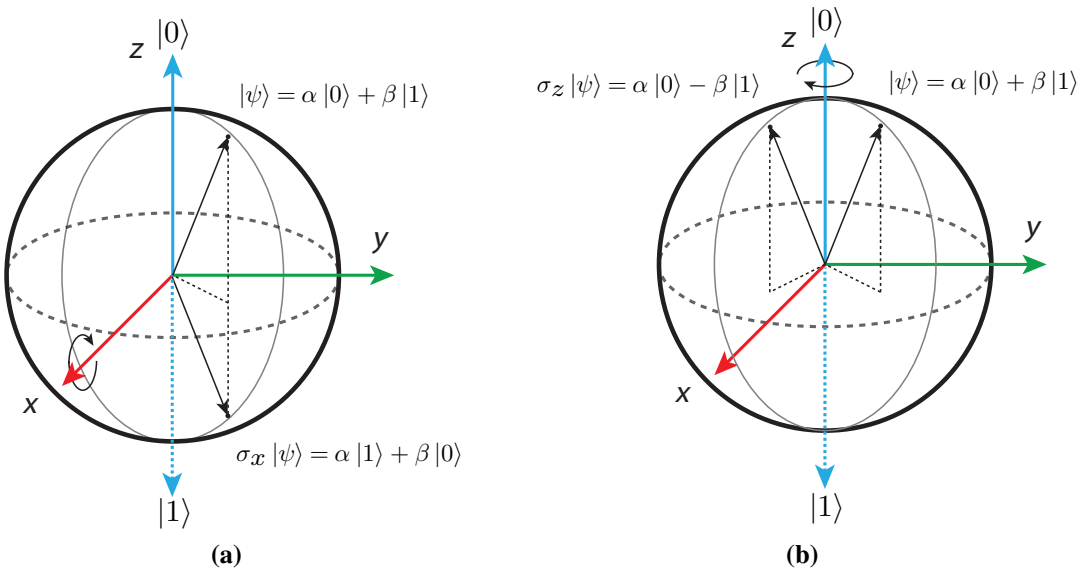

Figure 1·1: (a) Rotation around x-axis (b) Rotation around z-axiz When pauli-X is applied to the qubit, it flips the qubit value from $|0\rangle$ to $|1\rangle$ and $|1\rangle$ to $|0\rangle$. When pauli-Z is applied, relative phase between qubit $|0\rangle$ and $|1\rangle$ is fliped from $+1$ to -1.

There are some other important single qubit gates and they are the Hadamard gate H, phase rotation and $\frac{\pi}{8}$ rotations respectively.

$$H = \frac{1}{\sqrt{2}}\begin{pmatrix}1 & 1\\ 1 & -1\end{pmatrix}, phase = \begin{pmatrix}1 & 0\\ 0 & e^{i\phi}\end{pmatrix}, R_{\frac{\pi}{8}} = \begin{pmatrix}1 & 0\\ 0 & e^{i\frac{\pi}{4}}\end{pmatrix}. \tag{1.8}$$

1.3.2 Density Matrix

Density matrices are another way of representing a quantum state. A full picture of a quantum state is given through density matrices. The density matrix allows to describe states on both the surface (pure state) and inside of the Bloch sphere (mixed state). A mixed state shows a statistical mixture of two or more states which describes a classical coin-toss type of phenomenon and such state resides in a sphere not just on the surface. The significant difference appears when we explicitly compare a mixture of $|0\rangle$ and $|1\rangle$, and the

superposition of these two.

$$\rho_{mix} = \frac{1}{2}|0\rangle\langle 0| + \frac{1}{2}|1\rangle\langle 1| = \begin{pmatrix} \frac{1}{2} & 0 \\ 0 & \frac{1}{2} \end{pmatrix}, \tag{1.9}$$

$$\rho_{superposition} = \frac{1}{2}|0\rangle\langle 0| + \frac{1}{2}|0\rangle\langle 1| + \frac{1}{2}|1\rangle\langle 0| + \frac{1}{2}|1\rangle\langle 1| = \begin{pmatrix} \frac{1}{2} & \frac{1}{2} \\ \frac{1}{2} & \frac{1}{2} \end{pmatrix}. \tag{1.10}$$

A pure state has off-diagonal terms in the matrix and $\rho^2 = \rho$ holds. This is not true for a mixed state and cannot be described using only ket vectors. Define

$$|\psi\rangle = \begin{pmatrix} \alpha \\ \beta \end{pmatrix}, \langle\psi| = \begin{pmatrix} \alpha^* & \beta^* \end{pmatrix}, |\psi\rangle\langle\psi| = \begin{pmatrix} \alpha \\ \beta \end{pmatrix}\begin{pmatrix} \alpha^* & \beta^* \end{pmatrix} = \begin{pmatrix} \alpha\alpha^* & \alpha\beta^* \\ \beta\alpha^* & \beta\beta^* \end{pmatrix}. \tag{1.11}$$

This density matrix approach is useful when decoherence comes into play. Qubits can be extended to a multi-mode system and they are often called "qudits".

$$|\psi\rangle = a_0|0\rangle + a_1|1\rangle + \cdots + a_d|d\rangle, \tag{1.12}$$

where $|a_0|^2 + |a_1|^2 + \cdots + |a_d|^2 = 1$. A transformation done by the multiport devices on a single photon is introduced in later chapters and it follows this qudit representation.

1.3.3 Two Qubit Gate

Controlled-not (CNOT) gate is a two-qubit gate and it acts on a two-qubit state. Pick a basis for the two qubit state as $\{|0\rangle\otimes|0\rangle, |0\rangle\otimes|1\rangle, |1\rangle\otimes|0\rangle, |1\rangle\otimes|1\rangle\}$. The tensor product of the two qubits are given in a matrix form,

$$|00\rangle = |0\rangle\otimes|0\rangle = \begin{pmatrix} 1 \\ 0 \end{pmatrix}\otimes\begin{pmatrix} 1 \\ 0 \end{pmatrix} = \begin{pmatrix} 1 \\ 0 \\ 0 \\ 0 \end{pmatrix}. \tag{1.13}$$

The rest of the states in the basis follow the same rule.

The CNOT gate changes the state of a second qubit depending on the first qubit.

$$CNOT = \begin{pmatrix} 1 & 0 & 0 & 0 \\ 0 & 1 & 0 & 0 \\ 0 & 0 & 0 & 1 \\ 0 & 0 & 1 & 0 \end{pmatrix}. \tag{1.14}$$

The CNOT gate acts on two qubit state $(|00\rangle, |01\rangle, |10\rangle, |11\rangle)^T$ and if the first qubit is $|1\rangle$ then, the CNOT gate flips the second qubit.

The set of single qubit gates, as well as the CNOT gate, are essential sets to perform universal quantum computation because an appropriate combination of these gates can simulate any other quantum gates with arbitrary accuracy (Gottesman, 1998). The generalized two-qubit state is written as

$$|\psi\rangle = \frac{1}{\sqrt{2}}(a_{00}|00\rangle + a_{01}|01\rangle + a_{10}|10\rangle + a_{11}|11\rangle), \tag{1.15}$$

and CNOT transforms the state into

$$U_{CNOT}|\psi\rangle = \frac{1}{\sqrt{2}}(a_{00}|00\rangle + a_{01}|01\rangle + a_{10}|11\rangle + a_{11}|10\rangle). \tag{1.16}$$

1.4 Qubit Encoding in Optics

A single qubit can be defined physically by giving two distinct levels. The traditional encoding methods are path and polarization degrees of freedom. A photon has a polarization, and it is stable when a photon is propagated through the system. We can give two orthogonal logical bits for them.

$$|0\rangle_L = |H\rangle = a_H|0\rangle, |1\rangle_L = |V\rangle = a_V|0\rangle. \tag{1.17}$$

Similarly, we can introduce other basis,

$$|0\rangle_L = |D\rangle = \frac{1}{\sqrt{2}}(|H\rangle + |V\rangle), |1\rangle_L = |A\rangle = \frac{1}{\sqrt{2}}(|H\rangle - |V\rangle), \tag{1.18}$$

$$|0\rangle_L = |R\rangle = \frac{1}{\sqrt{2}}(|H\rangle + i|V\rangle), |1\rangle_L = |L\rangle = \frac{1}{\sqrt{2}}(|H\rangle - i|V\rangle). \tag{1.19}$$

The rotation of quantum states in optics can be done using waveplates. For example, a half-wave plate can introduce rotation of polarization ($|H\rangle \rightarrow |D\rangle$) without destroying photons, while a quarter-wave plate can introduce $\frac{\pi}{2}$ phase shift between the two orthogonal polarizations ($|H\rangle \rightarrow |R\rangle$). A polarizer acts as a projection device meaning if the input state is $|D\rangle = \frac{1}{\sqrt{2}}(|H\rangle + |V\rangle)$, then a polarizer angled to only pass $|H\rangle$ picks up horizontal part of the state with 50% intensity reduction. The final detection of a photon is performed by a photodetector. Detection of a photon is not reversible, hence the operation destroys the photon. Representing the same logical qubit representation in different ways has some advantages. We have three basis for a two-level system, and they are called mutually unbiased basis. This is particularly useful in quantum key distribution type of applications (Bennett and Brassard, 1984; Ekert, 1991) because projective measurement on one basis does not reveal information of a state on any other basis.

1.5 Photon Number State

We introduce a photon number state derived from the quantization of the single mode electromagnetic field. The single mode photon number state formalism can be extended to a multimode photon number state since the state is a product of all the modes (Gerry et al., 2005). A single mode electromagnetic field can be quantized by introducing canonical position and momentum making classical electromagnetic Hamiltonian equivalent to a harmonic oscillator. Traditionally, the Hamiltonian using creation $\hat{a}^\dagger$ and annihilation $\hat{a}$

operator take the following form.

$$\hat{H} = \hbar\omega\left(\hat{a}^{\dagger}\hat{a} + \frac{1}{2}\right). \tag{1.20}$$

A product of creation and annihilation operator $\hat{n} = \hat{a}^{\dagger}\hat{a}$ is called number operator and the associated eigenstate $|n\rangle$ for the Hamiltonian is

$$\begin{aligned}\hat{H}|n\rangle &= \hbar\omega\left(\hat{a}^{\dagger}\hat{a} + \tfrac{1}{2}\right)|n\rangle \\ &= E_n|n\rangle .\end{aligned} \tag{1.21}$$

Following equations are obtained by applying a creation operator from the left on Eq. 1.21.

$$\hat{a}^{\dagger}\hat{H}|n\rangle = \hat{a}^{\dagger}E_n|n\rangle , \tag{1.22}$$

$$\hbar\omega\left(\hat{a}^{\dagger}\hat{a} + \tfrac{1}{2}\right)(\hat{a}^{\dagger}|n\rangle) = (E_n + \hbar\omega)(\hat{a}^{\dagger}|n\rangle). \tag{1.23}$$

This implies that the creation operator increases the energy eigenvalue by $\hbar\omega$. Loosely speaking, a photon of energy $\hbar\omega$ is created by $\hat{a}^{\dagger}$. Similarly, $\hat{a}$ lowers the energy eigenvalue by $\hbar\omega$. We obtain the following for the number operator

$$\hat{n}|n\rangle = n|n\rangle . \tag{1.24}$$

The number state representation is convenient to describe the manipulation of photon numbers.

$$\hat{a}|n\rangle = \sqrt{n-1}\,|n-1\rangle , \tag{1.25}$$

$$\hat{a}^{\dagger}|n\rangle = \sqrt{n+1}\,|n+1\rangle . \tag{1.26}$$

The creation and annihilation operators have some other properties.

$$[\hat{a}, \hat{a}^{\dagger}] = 1. \tag{1.27}$$

Operator representation of having n photons in a single mode is given by,

$$|n\rangle = \frac{(\hat{a}^{\dagger})^n}{\sqrt{n!}}|0\rangle . \tag{1.28}$$

1.6 Entangled States

One of the most interesting states in a two-qubit system is entangled states. Entanglement is often associated with Einstein's "Spooky-action at a distance" to the general public, and Einstein-Podolsky-Rosen's paper (Einstein et al., 1935) became a centerpiece of quantum theory on entanglement. The two qubit system is relatively simple because the characterization of two-qubit entangled state does not require extensive measurements. Entangled states can be realized using optical polarization. Polarization does not need to be the only degree of freedom. Other degrees of freedom such as energy-time (Franson, 1989), orbital angular momentum (Mair et al., 2001) and so forth, can also realize quantum entanglement. All the distinct degrees of freedom can be applied at once to generate hyper-entangled photonic states as well (Barreiro et al., 2005). In principle, single photons and a beam splitter with some measurements can produce an entangled state. This procedure is called a post-selection (Zeilinger et al., 1997; Ou and Mandel, 1988; Kiess et al., 1993). Post-selection free entanglement generation (Kwiat et al., 1995) is introduced by spontaneous-parametric down-conversion (SPDC) (Klyshko et al., 1970) via non-linear crystal.

1.6.1 Bell States

$$|\psi^{\pm}\rangle = \frac{1}{\sqrt{2}}(|H\rangle_1 |V\rangle_2 \pm |V\rangle_1 |H\rangle_2), \tag{1.29}$$

$$|\phi^{\pm}\rangle = \frac{1}{\sqrt{2}}(|H\rangle_1 |H\rangle_2 \pm |V\rangle_1 |V\rangle_2). \tag{1.30}$$

Bell states are two-qubit maximally entangled states. They are entangled because they cannot be factored out using two independent single-qubit states. In photonics, SPDC is a

common technique to generate such states. The observation of Bell states is often performed by Bell's inequality (Bell, 1964) and witness operators (Horodecki, 1997). Quantum state tomography provides a full picture of a generated state by reconstructing the quantum state through a sufficient amount of different projective measurements (Chuang and Nielsen, 1997; Poyatos et al., 1997; Altepeter et al., 2003). The procedure for state tomography becomes expensive rapidly as the number of photons increases.

1.6.2 GHZ and W States

Greenberger–Horne–Zeilinger (GHZ) and W states are often mentioned when maximally entangled three-photon states are considered (Greenberger et al., 1989; Dür et al., 2000).

$$|GHZ\rangle = \frac{1}{\sqrt{2}}(|HHH\rangle \pm |VVV\rangle), \tag{1.31}$$

$$|W\rangle = \frac{1}{\sqrt{3}}(|HVV\rangle + |HVH\rangle + |VVH\rangle). \tag{1.32}$$

The difficulty of a high number entangled state generation increases significantly because high number entangled states require multiple low number entangled states with some operations (Zhong et al., 2018; Lu et al., 2007). Direct generation of a multi-photon entangled state is possible in principle; however this requires very low-probability higher-order non-linear effects in order to execute the state generation (Armstrong et al., 1962; Hamel et al., 2014). Multiple low-loss error-free quantum operations are needed to achieve the desired task.

Chapter 2

Linear Optics

2.1 Linear Optical Devices for Information Processing

Two-dimensional devices including interferometers are the main building blocks for any applications in classical and quantum optics. Unitary transformations on spatial modes are often used to employ quantum information processing. The dimensionality of information processing needs to be increased and it has been shown that high-dimensional unitary matrices can be decomposed using $U(2)$ matrices (Murnaghan, 1962). This indicates that a sequence of two-dimensional devices can implement higher dimensional devices. Flexibility is important due to the necessity of amplitude manipulation between the input and output fields. In principle, this could be achieved in two ways in optics:

1. by some kind of dynamic change in the input/output splitting ratio of a single beam splitter (BS).

2. by forming an interferometer with several beam splitters, thus offering tunability between output ports.

In this section, we start with the basic properties of a beam splitter implementing the $U(2)$ operation and discuss its features as a directionally-biased coupler. It will be followed by the consideration of integrated waveguided couplers and some well-known interferometers for implementing 2×2 transformations. Several higher dimensional unitary matrices are implemented and large unitary matrices decomposition methods are introduced as well.

2.1.1 Lossless Optical Beam Splitter

A lossless BS introduced in Fig. 2·1 redirects incoming photons into two outgoing ports while maintaining energy conservation (Loudon, 2000; Saleh et al., 1991). A BS can be represented using a 2×2 matrix, acting on two input and two output ports, denoted as E_1, E_2 and E_3, E_4, as indicated in Fig. 2·1. The transformation of the fields E_1, E_2 is given by:

$$\begin{pmatrix} E_3 \\ E_4 \end{pmatrix} = \begin{pmatrix} T_{13} & R_{23} \\ R_{14} & T_{24} \end{pmatrix} \begin{pmatrix} E_1 \\ E_2 \end{pmatrix}, \tag{2.1}$$

where T_{13}, T_{24} are the transmission from port 1 to 3 and 2 to 4 and R_{23}, R_{14} are reflection for port 2 to 3 and port 1 to 4, respectively. The probability conservation relation between the input and output is:

$$|E_3|^2 + |E_4|^2 = |E_1|^2 + |E_2|^2. \tag{2.2}$$

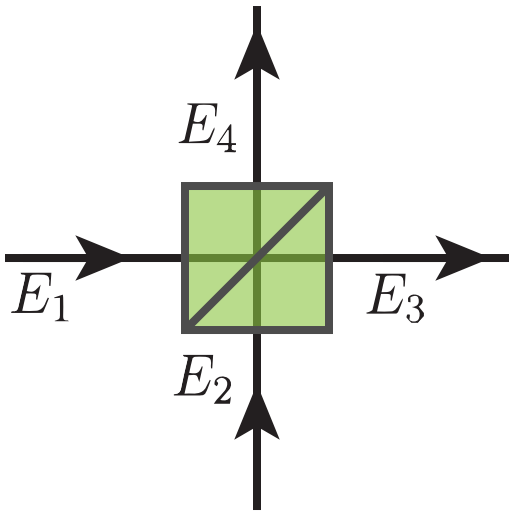

Figure 2·1: Description of a beam splitter. A beam splitter is a device with two input and two output ports. A photon can enter port E_1 and/or E_2 and will leave the port E_3 and/or E_4.

By substituting Eq. 2.1 in Eq. 2.2,

$$\begin{aligned} |E_3|^2+|E_4|^2 &= (|T_{13}|^2+|R_{14}|^2)|E_1|^2+(|T_{24}|^2+|R_{23}|^2)|E_2|^2 \\ &+ T_{13}R_{23}^*E_1E_2^*+R_{23}T_{13}^*E_2E_1^*+T_{24}R_{14}^*E_2E_1^*+R_{14}T_{24}^*E_1E_2^*, \end{aligned} \quad (2.3)$$

and by comparing the result with Eq. 2.2:

$$\begin{aligned} |T_{13}|^2+|R_{14}|^2 = |T_{24}|^2+|R_{23}|^2 = 1, \\ T_{13}R_{23}^*+R_{14}T_{24}^* = R_{23}T_{13}^*+T_{24}R_{14}^* = 0. \end{aligned} \quad (2.4)$$

Transmission and reflection coefficients T and R can be rewritten using amplitude and phase. Define $T_{13} = |T_{13}|e^{i\phi_{13}}$, and so on, for all the transmission and reflection coefficients. Then, Eq. 2.4 is reduced to:

$$\frac{|R_{23}|}{|T_{24}|} = -\frac{|R_{14}|}{|T_{13}|}e^{i(\phi_{14}+\phi_{23}-\phi_{24}-\phi_{13})}. \quad (2.5)$$

In order to satisfy Eq. 2.5, the phase values must be: $\phi_{14}+\phi_{23}-\phi_{24}-\phi_{13} = \pm\pi$. This phase relation offers some flexibility in choosing the phase settings. Two different phase settings often appear in the literature for a BS with a 50/50 power splitting ratio. When $|R_{23}| = |R_{14}| = |R| = \frac{1}{\sqrt{2}}, |T_{13}| = |T_{24}| = |T| = \frac{1}{\sqrt{2}}$, one could choose $\phi_{14} = \phi_{13} = \phi_{23} = 0, \phi_{24} = \pi$ as an example. Other splitting ratios can be chosen as long as $|T|^2+|R|^2 = 1$ is satisfied. Some different forms of BS show up in literature. Two such examples are given below. Example 1 is often pointed to a model with plate based beam splitters and example 2 is often used when cube beam splitters are used.

Example 1:

$$BS_1 = \frac{1}{\sqrt{2}}\begin{pmatrix} 1 & 1 \\ 1 & -1 \end{pmatrix}. \quad (2.6)$$

Other phase settings could be $\phi_{23} = \phi_{14} = \phi_R, \phi_{13} = \phi_{24} = \phi_T$ with $|R_{23}| = |R_{14}| = |R|, |T_{13}| = |T_{24}| = |T|$ and substituting these in Eq. 2.5.

$$\frac{|R|}{|T|} = -\frac{|R|}{|T|} e^{2i(\phi_T - \phi_R)}, \tag{2.7}$$

where $\phi_R - \phi_T = \frac{\pi}{2}$.

By choosing the phase settings $\phi_T = 0, \phi_R = \frac{\pi}{2}$, another example of the BS matrix can be produced.

Example 2:

$$BS_2 = \frac{1}{\sqrt{2}} \begin{pmatrix} 1 & i \\ i & 1 \end{pmatrix}. \tag{2.8}$$

Both examples are equivalent when appropriate phase shifters have been introduced before and after the beam splitter:

$$\frac{1}{\sqrt{2}} \begin{pmatrix} 1 & 1 \\ 1 & -1 \end{pmatrix} = \begin{pmatrix} 1 & 0 \\ 0 & e^{-i\frac{\pi}{2}} \end{pmatrix} \frac{1}{\sqrt{2}} \begin{pmatrix} 1 & i \\ i & 1 \end{pmatrix} \begin{pmatrix} 1 & 0 \\ 0 & e^{-i\frac{\pi}{2}} \end{pmatrix}. \tag{2.9}$$

A transformation from example 2 to example 1 is shown above.

2.1.2 The Directionality of a Beam Splitter

A beam splitter is a symmetric device, meaning that any one of four ports can be used as an input, and its action is invariant under time reversal. At the same time, there is another sense in which the device is not symmetric; the incoming photon cannot leave through the input port. We call this feature "directional-bias"; the choice of an input port biases the output to be in only two of the four possible output directions. This directional bias increases the required number of beam splitters when one enters the realm of higher dimensionality. In principle, this directional bias could be circumvented by placing external mirrors after the beam splitters so that they reverse the light propagation direction. This would allow the photon to leave through the input ports, and the system now becomes "directionally-unbiased"; all four output possibilities can still be realized, regardless of an input direction.

2.2 Interferometers as Two-Dimensional Devices

Interferometers are essential tools in quantum information processing and usually involve multiple beam splitters. The amplitude of each of the two outgoing modes can be modified by changing the relative phase between two paths. There are several major interferometer designs that offer 2×2 mode transformation. The Mach–Zehnder interferometer is a directionally-biased device that could be useful in realizing the Reck decomposition model, while the Michelson interferometer does not suffer from directional bias.

2.2.1 Mach–Zehnder Interferometer

The Mach–Zehnder interferometer shown in Fig.2·2 is a *directionally-biased* interferometer. Assume that each BS has a 50:50 power splitting ratio between the two outgoing fields and the device is symmetric because the path length between two arms can be made identical. The BS matrix U_{BS} is applied twice, and the relative phase shift ϕ between the two modes by applying the matrix U_{phase} is introduced before the photon encounters the second BS.

$$U_{MZ} = U_{BS} U_{phase} U_{BS}. \tag{2.10}$$

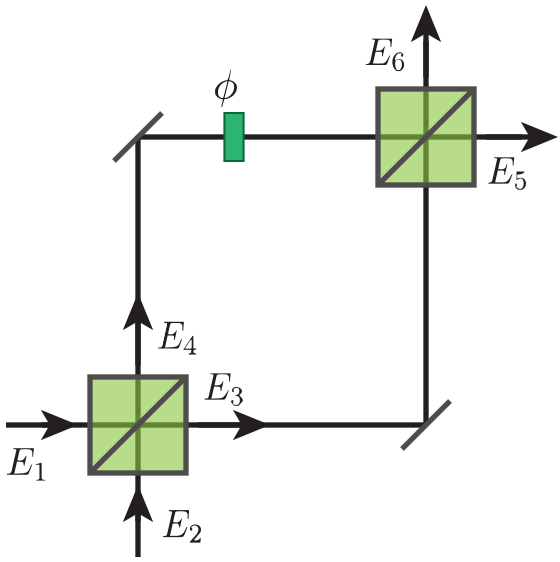

Figure 2·2: The Mach–Zehnder interferometer. A photon can enter either the port E_1 or E_2 and will be transformed by the first beam splitter. The photon can leave either through a superposition of E_3 and E_4 and be transformed by the second beam splitter. A phase plate ϕ is inserted between two beam splitters. The relative phase introduced between the upper and lower path changes the splitting ratio at the second BS. Finally, the photon leaves the device either through E_5 and/or E_6 modes.

By introducing expressions for the above matrices, one would obtain a specific formulation of the Mach–Zehnder transformation:

$$\begin{aligned} U_{MZ} &= \frac{1}{\sqrt{2}}\begin{pmatrix} 1 & i \\ i & 1 \end{pmatrix}\begin{pmatrix} e^{i\phi} & 0 \\ 0 & 1 \end{pmatrix}\frac{1}{\sqrt{2}}\begin{pmatrix} 1 & i \\ i & 1 \end{pmatrix} = \frac{1}{2}\begin{pmatrix} e^{i\phi}-1 & i(e^{i\phi}+1) \\ i(e^{i\phi}+1) & 1-e^{i\phi} \end{pmatrix} \\ &= \frac{1}{2}\begin{pmatrix} e^{i\frac{\phi}{2}}(e^{i\frac{\phi}{2}}-e^{-i\frac{\phi}{2}}) & ie^{i\frac{\phi}{2}}(e^{i\frac{\phi}{2}}+e^{-i\frac{\phi}{2}}) \\ ie^{i\frac{\phi}{2}}(e^{i\frac{\phi}{2}}+e^{-i\frac{\phi}{2}}) & -ie^{i\frac{\phi}{2}}(e^{i\frac{\phi}{2}}-e^{-i\frac{\phi}{2}}) \end{pmatrix} = e^{i(\frac{\phi}{2}+\frac{\pi}{2})}\begin{pmatrix} sin(\frac{\phi}{2}) & cos(\frac{\phi}{2}) \\ cos(\frac{\phi}{2}) & -sin(\frac{\phi}{2}) \end{pmatrix}. \end{aligned} \tag{2.11}$$

The element-wise multiplication leads to the following input-output probability distribution:

$$P_{MZ} = U_{MZ}U_{MZ}^{*} = \frac{1}{2}\begin{pmatrix} 1-cos\phi & 1+cos\phi \\ 1+cos\phi & 1-cos\phi \end{pmatrix}, \tag{2.12}$$

where U^{*} is a complex conjugate of U.

One can easily see that the Mach–Zehnder interferometer effectively serves as a *tunable*

directionally-biased variable beam splitter, and this tunability plays a key role in higher-dimensional interferometer-based optical networks.

2.2.2 Michelson Interferometer

The Michelson interferometer in Fig.2·3 is one example of the *directionally-unbiased* 2×2 device. Its layout could be used as an illustration of a general optical design principle that the directional bias within a 2×2 device could be circumvented by placing mirrors after the first beam splitter encounter and reversing directions of the optical flux.

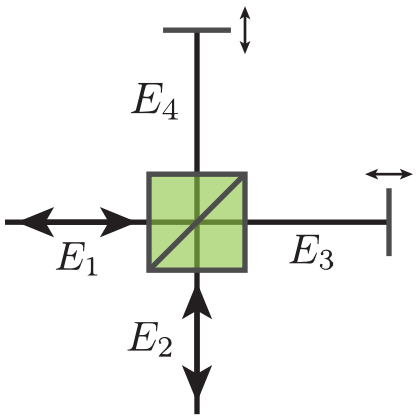

Figure 2·3: The Michelson interferometer. A photon can enter either port E_1 and/or E_2. The photon interacts with a beam splitter, mirrors, and again with a beamsplitter. The photon leaves through either E_1 and/or E_2, which are the same as the input ports. The phase can be controlled by translating mirrors in the system.

A state of the input photon will be transformed by the first interaction with a BS.

$$\begin{pmatrix} E_3 \\ E_4 \end{pmatrix} = U_{BS} \begin{pmatrix} E_1 \\ E_2 \end{pmatrix}, \tag{2.13}$$

where U_{BS} represents a linear transformation same as the previous subsection between the

input fields and output fields of a beam splitter. In order to consider the transformation of fields from E_3 and E_4 to E_1 and E_2, one must multiply the outcome with the inverse of matrix U_{BS} from the left.

$$U_{BS}^{-1}\begin{pmatrix} E_3 \\ E_4 \end{pmatrix} = U_{BS}^{-1} U_{BS}\begin{pmatrix} E_1 \\ E_2 \end{pmatrix}. \tag{2.14}$$

Since U_{BS} is a unitary matrix $U_{BS}^{-1} = U_{BS}^{\dagger}$, then:

$$\begin{pmatrix} E_1 \\ E_2 \end{pmatrix} = U_{BS}^{\dagger}\begin{pmatrix} E_3 \\ E_4 \end{pmatrix}. \tag{2.15}$$

This describes the transformation from E_3 and E_4 to E_1 and E_2. This still represents a forward propagation; therefore, we must take a complex conjugate to reverse the propagation direction.

$$\begin{pmatrix} E_1^* \\ E_2^* \end{pmatrix} = U_{BS}^{T}\begin{pmatrix} E_3^* \\ E_4^* \end{pmatrix}. \tag{2.16}$$

This equation is read as a reverse propagation from E_3 and E_4 to E_1 and E_2. Now, the 2 $\times$ 2 transformation of optical modes by the Michelson interferometer is described as:

$$U_{Michelson} = U_{BS}^{T} U_{Phase} U_{BS}. \tag{2.17}$$

The first transformation U_{BS} describes the propagation from E_1 and E_2 to E_3 and E_4, and then, phase shift U_{phase} introduces phase shifts between the two fields. The phases can be controlled by translating mirrors in the system as indicated in Fig. 2·3. Finally, the reversed propagation and transformation from E_3 and E_4 to E_1 and E_2 is given by U_{BS}^{T}. These transformations complete the transformation of input fields by the Michelson interferometer. Such 2 $\times$ 2 directionally-unbiased devices based on the Michelson interferometer configuration could be used as elements for building higher dimensional interferometric systems. The Michelson interferometer is essentially the two-port version of the unbiased multiports introduced below, with U_{phase} providing the tunability.

2.3 Hong-Ou-Mandel Effect

The Hong-Ou-Mandel effect is a two-photon intensity interference effect. The effect is observed when two identical photons impinge on a BS. In an experiment, this effect can be observed through coincidence measurements with temporal delay in one arm. The coincidence count disappears when a temporal delay between two photons is compensated. A temporal delay between two photons distinguishes the photons resulting in well known HOM dip (Agarwal, 2012; Loudon, 2000; Knight et al., 2003a).

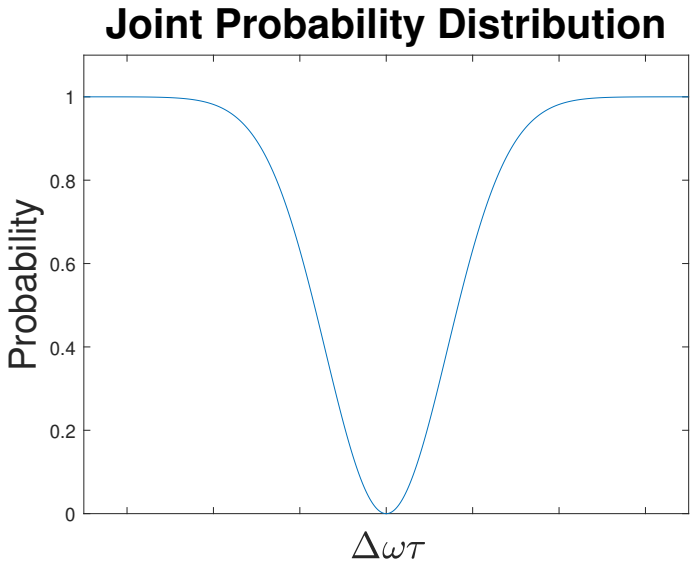

Figure 2·4: Hong-Ou-Mandel dip. The joint probability approaches to zero as the wevepackets overlap perfectly.

The coincidence probability distribution is given by

$$P \propto 1 - e^{-\Delta\omega^2\tau^2}, \tag{2.18}$$

where τ is the time difference between the two photons and $\Delta\omega$ is the bandwidth of a photon wave packet. Joint probability becomes zero when $\tau = 0$.

The coincidence term cancellation can be described mathematically in a simple manner using identical photons. A BS transforms a photon coming from spatial mode $\hat{a} \rightarrow \frac{1}{\sqrt{2}}(\hat{c} + \hat{d})$

and $\hat{b} \rightarrow \frac{1}{\sqrt{2}}(\hat{c} - \hat{d})$. Consider feeding two single photons at each BS input port. Each photon state evolves as follows,

$$\begin{aligned} \hat{a}\hat{b} &\rightarrow \tfrac{1}{2}(c+d)(c-d) = \tfrac{1}{2}(c^2 + cd - dc + d^2) \\ &= \tfrac{1}{2}(c^2 + d^2) = \tfrac{1}{\sqrt{2}}(|2,0\rangle + |0,2\rangle), \end{aligned} \tag{2.19}$$

where we have used the commutation property $cd = dc$. When two photons are distinguishable by giving polarization degrees of freedom then,

$$a_H b_V \rightarrow \frac{1}{2}(c_H + d_H)(c_V - d_V) = \frac{1}{2}(c_H c_V + c_H d_V - d_H c_V + d_H d_V). \tag{2.20}$$

Notice that the cross-terms are now not canceled out. Therefore, photodetectors click when joint measurements are performed between spatial modes c and d. Distinguishable photons do not exhibit HOM dip when joint measurements are performed.

2.3.1 2×2 Integrated Directional Waveguide Coupler

A directional coupler is an integrated optics analog of a beam splitter. When two waveguides are brought close together, evanescent waves overlap and start coupling in the neighboring waveguide. Fig. 2·5 illustrates a 2×2 integrated directional coupler and its cross-section. The coupling strength κ can be controlled by changing the distance between two waveguides. The BS and a directional coupler are both directionally-biased devices. The propagation of a photon through these devices can be described using a transfer matrix U. $E_{out} = UE_{in}$, where E_{in} and E_{out} are the input and output fields.

The transfer matrix of the directional coupler can be derived using coupled-mode equations based on the Heisenberg equation (Bromberg et al., 2009; Spagnolo et al., 2013a).

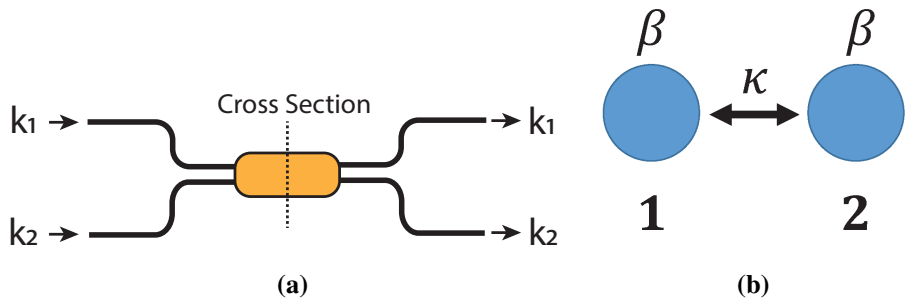

(a) (b)

Figure 2·5: (**a**) A 2×2 directional coupler. k_1 and k_2 represent input and output spatial modes. A photon can enter either k_1 or k_2, and a coupler transforms the input state. Two waveguides are closely located to allow evanescent coupling at the cross-section in the figure. (**b**) The cross-section area in the directional coupler illustrated in (**a**). The coupling strength between two waveguides is κ, and the propagation constant in each waveguide is β.

The evolution in the z direction is given by:

$$\begin{aligned} i\frac{dA_1^\dagger}{dz} &= \beta A_1^\dagger + \kappa A_2^\dagger, \\ i\frac{dA_2^\dagger}{dz} &= \kappa A_1^\dagger + \beta A_2^\dagger, \end{aligned} \tag{2.21}$$

where $A_j^\dagger \{j = 1,2\}$ are creation operators for a photon in the j^{th} waveguide. β is a waveguide propagation constant, and κ is a coupling coefficient between the two waveguides.

Eq. 2.21 can be rewritten in a matrix form:

$$\begin{pmatrix} \frac{dA_1^\dagger}{dz} \\ \frac{dA_2^\dagger}{dz} \end{pmatrix} = -i \begin{pmatrix} \beta & \kappa \\ \kappa & \beta \end{pmatrix} \begin{pmatrix} A_1 \\ A_2 \end{pmatrix}. \tag{2.22}$$

We can solve for A_1 and A_2 by Eq. 2.21 using differential equation solutions in the form of Eq. 2.22 and finding eigenvalues and eigenvectors.

Eigenvalues with corresponding eigenvectors are given by:

$$\lambda_1 = -\beta i - \kappa i : \begin{pmatrix} 1 \\ 1 \end{pmatrix}, \lambda_2 = -\beta i + \kappa i : \begin{pmatrix} -1 \\ 1 \end{pmatrix},$$

$$\begin{pmatrix} A_1 \\ A_2 \end{pmatrix} = c_1 e^{-(\beta z+\kappa z)i} \begin{pmatrix} 1 \\ 1 \end{pmatrix} + c_2 e^{-(\beta z-\kappa z)i} \begin{pmatrix} -1 \\ 1 \end{pmatrix}, \tag{2.23}$$

Initial conditions are given by: $A_1(0) = 1, A_2(0) = 0$, and $c_1 = \frac{1}{2}, c_2 = -\frac{1}{2}$. The full transfer matrix can be reconstructed after solving also for the alternative initial condition: $A_1(0) = 0, A_2(0) = 1$.

$$U_{Coupler} = \frac{e^{-\beta z i}}{2} \begin{pmatrix} e^{-\kappa z i} + e^{\kappa z i} & e^{-\kappa z i} - e^{\kappa z i} \\ e^{-\kappa z i} - e^{\kappa z i} & e^{-\kappa z i} + e^{\kappa z i} \end{pmatrix} = e^{-\beta z i} \begin{pmatrix} cos(\kappa z) & -isin(\kappa z) \\ -isin(\kappa z) & cos(\kappa z) \end{pmatrix}. \tag{2.24}$$

2.4 Integrated Optical Tritter and Quarter

Three- and four-dimensional directional linear optical devices are introduced in this section. Integrated waveguide couplers (Spagnolo et al., 2013a; Spagnolo et al., 2013b; Spagnolo et al., 2012; Meany et al., 2012) can be used to implement an optical tritter illustrated in Fig. 2·6a and its cross-section shown in Fig. 2·6b. The propagation dynamics of such a system can be described using the same formalism as in the previous case of the directional 2×2 coupler:

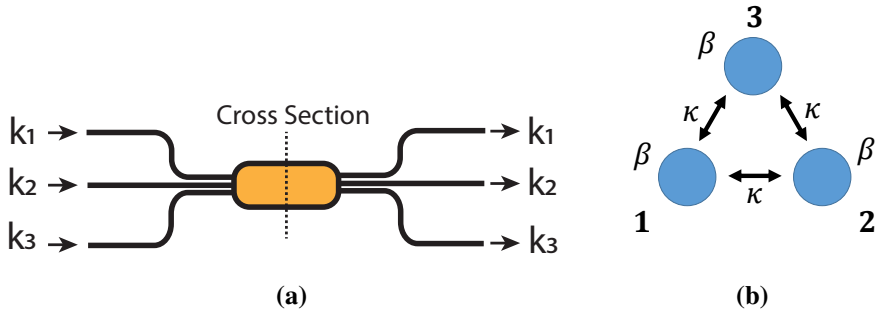

Figure 2·6: (**a**) Integrated optical tritter. k_i $\{i = 1,2,3\}$ represent input and output spatial modes. (**b**) Coupling region of the integrated tritter. β is a waveguide propagation coefficient, and κ is a coupling coefficient between the couplers.

$$
\begin{aligned}
i\frac{dA_1^\dagger}{dz} &= \beta A_1^\dagger + \kappa A_2^\dagger + \kappa A_3^\dagger, \\
i\frac{dA_2^\dagger}{dz} &= \kappa A_1^\dagger + \beta A_2^\dagger + \kappa A_3^\dagger, \\
i\frac{dA_3^\dagger}{dz} &= \kappa A_1^\dagger + \kappa A_2^\dagger + \beta A_3^\dagger,
\end{aligned}
\tag{2.25}
$$

where $A_j^\dagger$ $\{j = 1,2,3\}$ are creation operators for a photon in the j^{th} waveguide; β is a propagation constant in each waveguide; and κ is a coupling coefficient. It is assumed that all waveguides are identical and the distances between them are the same.

One could solve these equations using a matrix formalism in a similar way as the two-dimensional case:

$$
\begin{pmatrix} \frac{dA_1}{dz} \\ \frac{dA_2}{dz} \\ \frac{dA_3}{dz} \end{pmatrix} = -i \begin{pmatrix} \beta & \kappa & \kappa \\ \kappa & \beta & \kappa \\ \kappa & \kappa & \beta \end{pmatrix} \begin{pmatrix} A_1 \\ A_2 \\ A_3 \end{pmatrix}. \tag{2.26}
$$

One could find eigenvalues and corresponding eigenvectors:

$$
\lambda_1 = -\beta i + \kappa i : \begin{pmatrix} -1 \\ 1 \\ 0 \end{pmatrix}, \begin{pmatrix} -1 \\ 0 \\ 1 \end{pmatrix}, \lambda_2 = -\beta i - 2\kappa i : \begin{pmatrix} 1 \\ 1 \\ 1 \end{pmatrix},
$$

$$
\begin{pmatrix} A_1 \\ A_2 \\ A_3 \end{pmatrix} = c_1 e^{-\beta z i + \kappa z i} \begin{pmatrix} -1 \\ 1 \\ 0 \end{pmatrix} + c_2 e^{-\beta z i + \kappa z i} \begin{pmatrix} -1 \\ 0 \\ 1 \end{pmatrix} + c_3 e^{-\beta z i - 2\kappa z i} \begin{pmatrix} 1 \\ 1 \\ 1 \end{pmatrix}. \tag{2.27}
$$

When the initial conditions are given by: $A_1(0) = 1, A_2(0) = 0, A_3(0) = 0$, then $c_1 = c_2 = -\frac{1}{3}, c_3 = \frac{1}{3}$, where z is the propagation length. Other initial conditions are given as $A_1(0) = 0, A_2(0) = 1, A_3(0) = 0$, and $A_1(0) = 0, A_2(0) = 0, A_3(0) = 1$. After solving for all initial conditions, we can obtain a total transfer matrix for the system.

$$
U_{IntTritter} = \frac{e^{-\beta z i}}{3} \begin{pmatrix} 2e^{\kappa z i} + e^{-2\kappa z i} & -e^{\kappa z i} + e^{-2\kappa z i} & -e^{\kappa z i} + e^{-2\kappa z i} \\ -e^{\kappa z i} + e^{-2\kappa z i} & 2e^{\kappa z i} + e^{-2\kappa z i} & -e^{\kappa z i} + e^{-2\kappa z i} \\ -e^{\kappa z i} + e^{-2\kappa z i} & -e^{\kappa z i} + e^{-2\kappa z i} & 2e^{\kappa z i} + e^{-2\kappa z i} \end{pmatrix}. \tag{2.28}
$$

Unlike two- and three-dimensional couplers where the distances between each pair of couplers are the same, for the four-dimensional coupler with its cross-section in Fig. 2·7b, the coupling coefficients between diagonal coupling regions are different from those on the edges of the square. We again assume the coupling strength can be controlled.

$$\begin{aligned}
i\frac{dA_1^\dagger}{dz} &= \beta A_1^\dagger + \kappa_1 A_2^\dagger + \kappa_2 A_3^\dagger + \kappa_1 A_4^\dagger, \\
i\frac{dA_2^\dagger}{dz} &= \kappa_1 A_1^\dagger + \beta A_2^\dagger + \kappa_1 A_3^\dagger + \kappa_2 A_4^\dagger, \\
i\frac{dA_3^\dagger}{dz} &= \kappa_2 A_1^\dagger + \kappa_1 A_2^\dagger + \beta A_3^\dagger + \kappa_1 A_4^\dagger, \\
i\frac{dA_4^\dagger}{dz} &= \kappa_1 A_1^\dagger + \kappa_2 A_2^\dagger + \kappa_1 A_3^\dagger + \beta A_4^\dagger,
\end{aligned} \tag{2.29}$$

where $A_j^\dagger$ $\{j = 1,2,3,4\}$ are creation operators for a photon in the j^{th} waveguide, β is a propagation constant, κ_1 is a coupling coefficient between two non-diagonal couplers, and κ_2 is a coupling coefficient for two diagonal couplers.

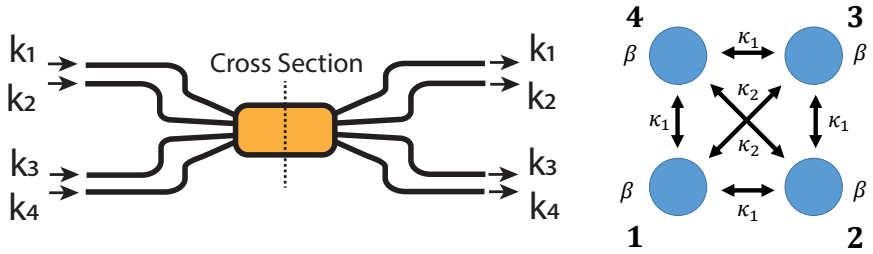

Figure 2·7: (**a**) Integrated quarter. k_i $\{i = 1,2,3,4\}$ represent input and output spatial modes. (**b**) Cross-section area of the integrated quarter. A waveguide propagation constant is β, and coupling coefficients are κ_1 for the neighboring couplers and κ_2 for the diagonal couplers.

One could solve this combination of equations using matrix formalism

$$\begin{pmatrix} \frac{dA_1}{dz} \\ \frac{dA_2}{dz} \\ \frac{dA_3}{dz} \\ \frac{dA_4}{dz} \end{pmatrix} = -i \begin{pmatrix} \beta & \kappa_1 & \kappa_2 & \kappa_1 \\ \kappa_1 & \beta & \kappa_1 & \kappa_2 \\ \kappa_2 & \kappa_1 & \beta & \kappa_1 \\ \kappa_1 & \kappa_2 & \kappa_1 & \beta \end{pmatrix} \begin{pmatrix} A_1 \\ A_2 \\ A_3 \\ A_4 \end{pmatrix}. \tag{2.30}$$

and by finding its eigenvalues and eigenvectors:

$$\lambda_1 = \beta i - \kappa_2 i : \begin{pmatrix} -1 \\ 0 \\ 1 \\ 0 \end{pmatrix}, \begin{pmatrix} 0 \\ -1 \\ 0 \\ 1 \end{pmatrix},$$

$$\lambda_2 = \beta i - 2\kappa_1 i + \kappa_2 i : \begin{pmatrix} -1 \\ 1 \\ -1 \\ 1 \end{pmatrix}, \lambda_3 = \beta i + 2\kappa_1 i + \kappa_2 i : \begin{pmatrix} 1 \\ 1 \\ 1 \\ 1 \end{pmatrix}, \tag{2.31}$$

$$\begin{pmatrix} A_1 \\ A_2 \\ A_3 \\ A_4 \end{pmatrix} = c_1 e^{\beta z i - \kappa_2 z i} \begin{pmatrix} -1 \\ 0 \\ 1 \\ 0 \end{pmatrix} + c_2 e^{\beta z i - \kappa_2 z i} \begin{pmatrix} 0 \\ -1 \\ 0 \\ 1 \end{pmatrix}$$

$$+ c_3 e^{\beta z i - 2\kappa_1 z i + \kappa_2 z i} \begin{pmatrix} -1 \\ 1 \\ -1 \\ 1 \end{pmatrix} + c_4 e^{\beta z i + 2\kappa_1 z i + \kappa_2 z i} \begin{pmatrix} 1 \\ 1 \\ 1 \\ 1 \end{pmatrix}. \tag{2.32}$$

When the initial conditions are given by: $A_1(0) = 1, A_2(0) = 0, A_3(0) = 0, A_4(0) = 0$, then $c_1 = -\frac{1}{2}, c_2 = 0, c_3 = -\frac{1}{4}, c_4 = \frac{1}{4}$ where z is the propagation length. After imposing the initial conditions and solving, we obtain a total transfer matrix for the system:

$$U_{IntQuarter} = \frac{e^{\beta z i}}{4} \begin{pmatrix} A & B & C & B \\ B & C & B & A \\ C & B & A & B \\ B & A & B & C \end{pmatrix}, \tag{2.33}$$

where:

$$
\begin{aligned}
A &= 2e^{-\kappa_2 zi} + e^{(-2\kappa_1+\kappa_2)zi} + e^{(2\kappa_1+\kappa_2)zi}, \\
B &= -e^{(-2\kappa_1+\kappa_2)zi} + e^{(2\kappa_1+\kappa_2)zi}, \\
C &= -2e^{-\kappa_2 zi} + e^{(-2\kappa_1+\kappa_2)zi} + e^{(2\kappa_1+\kappa_2)zi}.
\end{aligned}
\tag{2.34}
$$

2.5 Three- and Four-Dimensional Linear Optical Devices

The dimensionality of the 2×2 linear-optical devices investigated in the previous section can be expanded to a more general situation covering a greater number of spatial modes. It has been demonstrated in the past that one has to rely on using multiple 2×2 beam splitters in order to execute a high-dimensional transformation. This relationship is often called a Reck decomposition model (Reck model) (Reck et al., 1994). The Reck model has been demonstrated experimentally (Carolan et al., 2015). There is also a symmetric directional alternative to Reck's approach that is called Clements' design (Sansoni et al., 2012; Clements et al., 2016). This design can realize any unitary matrices and will be discussed in the 4×4 device section. In addition to Reck's and Clements' decomposition via multiple lower dimensional devices, a 3×3 directional transformation could be realized directly by exploiting a 3D optical integrated device in a waveguide configuration that is called an optical tritter (Kowalevicz et al., 2005; Suzuki et al., 2006; Meany et al., 2012). Another decomposition model has been proposed as well (de Guise et al., 2018). This section examines these possible designs for 3×3 and 4×4 devices in detail. Four-dimensional devices are not just a simple extension of the three-dimensional devices. When the number of ports exceeds three, the distances between couplers are not identical. This suggests coupling strength would not be the same between couplers; therefore, it can change the final transfer matrix between the input fields and the output fields.

2.5.1 Reck Decomposition Design

It has been determined theoretically (Reck et al., 1994) that an arbitrary single N $\times$ N unitary matrix, U(N), can be decomposed into a succession of $\frac{N(N-1)}{2}$ numbers of 2 $\times$ 2 mode mixing matrices. In order to understand the decomposition procedure, it is useful to understand the decomposition procedure for the 2 $\times$ 2 unitary matrix. Higher dimensional decomposition examples will be provided after the 2 $\times$ 2 example. An arbitrary unitary 2 $\times$ 2 matrix U(2) is defined as:

$$U(2) = \begin{pmatrix} A & B \\ C & D \end{pmatrix}, \tag{2.35}$$

where $A, B, C, D \in \mathbb{C}$. $\mathbb{C}$ is a set of complex numbers. It is always possible to find a unitary matrix T such that U(2) becomes diagonal after it is multiplied by the matrix T.

$$U(2)T = \begin{pmatrix} A' & 0 \\ 0 & D' \end{pmatrix}, \tag{2.36}$$

where $A', D' \in \mathbb{C}$.

The resulting diagonalized matrix is turned into an identity matrix by multiplying it with an additional diagonal matrix P.

$$U(2)TP = \begin{pmatrix} 1 & 0 \\ 0 & 1 \end{pmatrix}. \tag{2.37}$$

This procedure shows that any U(2) matrix can be transformed into an identity matrix. This result indicates that the inverse matrix $(TP)^{-1}$ is the original U(2) we wanted. T and P are both unitary matrices; therefore, $T^{-1} = T^{\dagger}$ and $P^{-1} = P^{\dagger}$ where † is complex conjugate and transpose.

$$U(2)TP = I(2) \rightarrow U(2) = (TP)^{-1} = P^{\dagger}T^{\dagger}. \tag{2.38}$$

This procedure shows that a matrix U(2) is decomposed into matrices $P^{\dagger}$ and $T^{\dagger}$. Such a diagonalization process can be applied in higher dimensions as well. In the 3 $\times$ 3 case,

arbitrary U(3) matrices can be diagonalized using multiple 3×3 matrices with each matrix containing U(2) inside. $T_{3,1}$, $T_{2,1}$, and $T_{3,2}$ are the matrices containing U(2) inside. $T_{3,1}$ mixes spatial Modes 3 and 1; $T_{2,1}$ mixes spatial Modes 2 and 1; and $T_{3,2}$ mixes spatial Modes 3 and 2.

$$T_{3,1} = \begin{pmatrix} U(2)_{1,1} & 0 & U(2)_{1,2} \\ 0 & 1 & 0 \\ U(2)_{2,1} & 0 & U(2)_{2,2} \end{pmatrix}, T_{3,2} = \begin{pmatrix} 1 & 0 \\ 0 & U(2) \end{pmatrix}, T_{2,1} = \begin{pmatrix} U(2) & 0 \\ 0 & 1 \end{pmatrix}, \tag{2.39}$$

where $U(2)_{1,1}$ is the element of U(2) from the first row and the first column. The rest of three elements $U(2)_{1,2}, U(2)_{2,1}, U(2)_{2,2}$ follow the same rule. Our goal is to find a decomposition for an arbitrary matrix U(3). Assume that the U(3) matrix has the form of:

$$U(3) = \begin{pmatrix} A_1 & B_1 & C_1 \\ D_1 & E_1 & F_1 \\ G_1 & H_1 & I_1 \end{pmatrix}. \tag{2.40}$$

As a first step, elements from the first row and the third column $U(3)_{1,3}$ and the third row and the first column $U(3)_{3,1}$ can be eliminated by multiplying a matrix $T_{3,2}$.

$$U(3)T_{3,2} = \begin{pmatrix} A_2 & B_2 & 0 \\ D_2 & E_2 & F_2 \\ 0 & H_2 & I_2 \end{pmatrix}. \tag{2.41}$$

Repeat the elimination procedure for all the non-diagonal elements of U(3).

$$U(3)T_{3,2}T_{3,1} = \begin{pmatrix} A_3 & B_3 & 0 \\ D_3 & E_3 & 0 \\ 0 & 0 & I_3 \end{pmatrix}, \tag{2.42}$$

$$U(3)T_{3,2}T_{3,1}T_{2,1} = \begin{pmatrix} A_4 & 0 & 0 \\ 0 & E_4 & 0 \\ 0 & 0 & I_4 \end{pmatrix}. \tag{2.43}$$

U(3) is transformed into an identity matrix after multiplying by a diagonal matrix P. U(3)

can be obtained by taking the inverse of $(T_{3,2}T_{3,1}T_{2,1}P)$.

$$U(3)T_{3,2}T_{3,1}T_{2,1}P = I(3) \rightarrow U(3) = (T_{3,2}T_{3,1}T_{2,1}P)^{-1} = P^{\dagger}T_{2,1}^{\dagger}T_{3,1}^{\dagger}T_{3,2}^{\dagger}. \tag{2.44}$$

Matrix elements A_i through I_i, $i \in \mathbb{Z}$ belong to $\mathbb{C}$. $\mathbb{Z}$ is a set of integers. The U(3) matrix is decomposed into matrices $P^{\dagger}$, $T_{2,1}^{\dagger}$, $T_{3,1}^{\dagger}$, and $T_{3,2}^{\dagger}$. This leads to the conclusion that the knowledge of each individual beam splitter (or interferometer) in the system allows reconstructing a transfer matrix of the whole system. The same reconstruction process can be applied in the 4×4 case of U(4) decomposition.

$$\begin{aligned} &U(4)T_{4,3}T_{4,2}T_{4,1}T_{3,2}T_{3,1}T_{2,1}P = I(4) \\ \rightarrow U(4) &= (T_{4,3}T_{4,2}T_{4,1}T_{3,2}T_{3,1}T_{2,1}P)^{-1} = P^{\dagger}T_{2,1}^{\dagger}T_{3,1}^{\dagger}T_{3,2}^{\dagger}T_{4,1}^{\dagger}T_{4,2}^{\dagger}T_{4,3}^{\dagger}. \end{aligned} \tag{2.45}$$

The matrices $T_{i,j}, i, j \in \mathbb{Z}$ are 4×4 matrices, which contain U(2) matrices inside. The experimental setup in the case of 3×3 transformation is illustrated in Fig. 2·8. The order of embedded U(2) matrices' multiplication and their action is equivalent to the physical diagram outlined. The 4×4 case is given in Fig. 2·9.

2.5.2 Clements Decomposition Design

The unitary matrix decomposition can also be realized in a slightly different configuration. The Clements design transforms the originally non-symmetric Reck configuration into a symmetric form (Clements et al., 2016), by which we mean that the situation is non-symmetric when photons in different input ports experience different numbers of beam splitters during their propagation and before exiting the unit. It would be helpful for any future consideration to introduce a simplified mesh representation for the systems outlined in Fig. 2·10. For example, in the case of 4×4 transformation, its mesh decomposition via U(2) embedded matrices could be represented either by the original decomposition proposed by Reck. The crossing parts in the mesh designs mix spatial modes and consist of integrated couplers. The tunability of the power splitting ratio can be obtained either through the

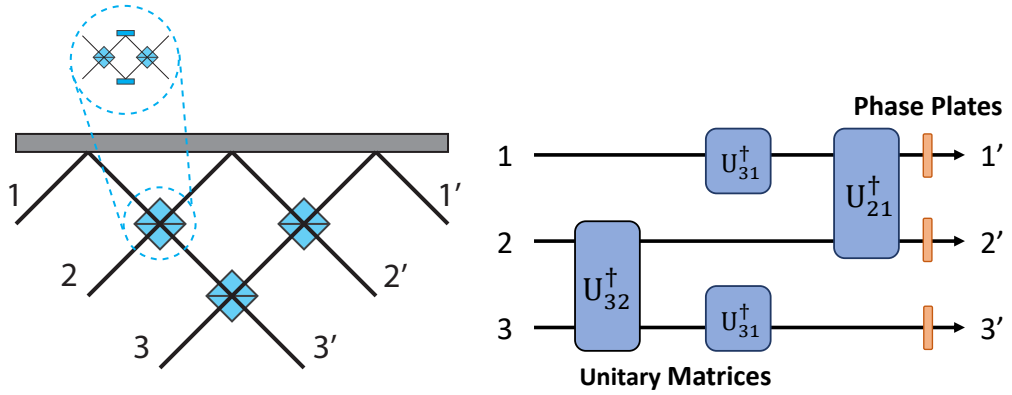

Figure 2·8: (**a**) The 3 × 3 Reck model realization using three beam splitters. A photon can enter either Port 1, 2, or 3 and the photon leaves either Port 1', 2', and/or 3'. A beam splitter in the system can be substituted by a Mach–Zehnder interferometer if one wants to give amplitude tuning at each beam splitter encounter. The beam splitter requirement will be increased to six when amplitude tuning by interferometers is imposed. (**b**) The information flow decomposition of the bulk 3 × 3 setup using a set of 2 × 2 unitary matrices. This is equivalent to the physical setup in (**a**).

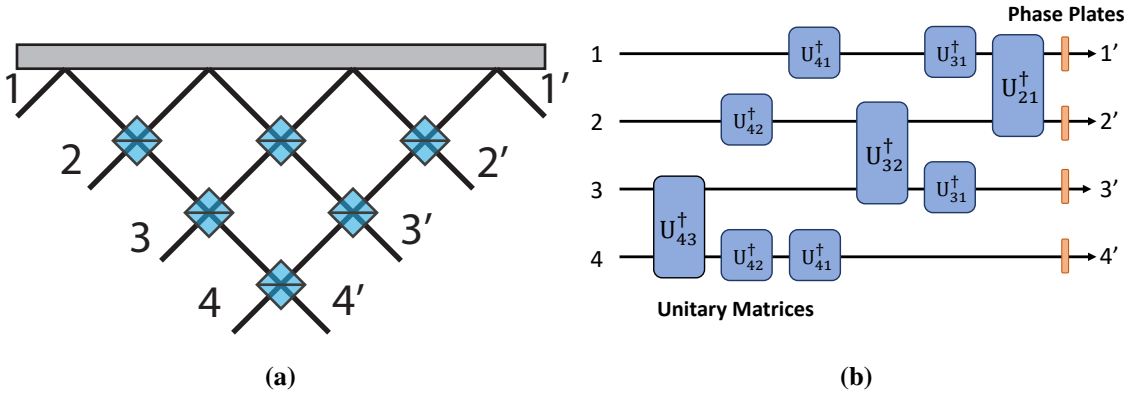

Figure 2·9: (**a**) The 4 × 4 Reck model using six beam splitters (12 with tunability). A photon can enter either one of four input ports and can leave through any of the four output ports. (**b**) The information flow representation in the case of decomposing a bulk 4 × 4 setup using 2 × 2 unitary matrices illustrated in (**a**).

dynamical change of the coupling ratio between two waveguides in an integrated coupler or by forming an interferometer using two integrated couplers executed the same task. The graphical detail of the crossing parts in mesh design is indicated in Fig. 2·11.

(a) (b)

Figure 2·10: (**a**) 4 × 4 mesh of the Reck design. Input photons flow from the left to the right. Each line cross-section consists of the two-dimensional two-mode mixer illustrated in Figure 2·11. This is identical to the setup in Figure 2·9a. (**b**) 4 × 4 mesh of symmetric Clements design.

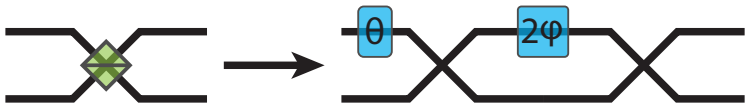

Figure 2·11: An integrated coupler requires tunability to change a transfer matrix of the system. The tunability is acquired through an interferometer with phase shifters. θ is an external phase shift, and ϕ is an internal phase shift.

The mesh designs are illustrated in Fig. 2·10. They are equivalent to the 4 × 4 Reck model and 4 × 4 Clements model. It is clear that a photon in the first path of the 4 × 4 Reck design illustrated in Fig. 2·10a could encounter only one beam splitter, while the photon in the lowest path encounters at least three beam splitters prior to exiting the device. In the Clements symmetric design illustrated in Fig. 2·10b, a photon in the first path and a photon in the last path encounter the same number of beam splitters. The loss tolerance of a quantum state becomes higher when a photon experiences the same number of beam splitter interactions (Clements et al., 2016). The Clements designs are widely used instead of Reck decomposition, precisely because of its loss tolerance in quantum information processing.

In a similar manner to the Reck model, a unitary matrix can be decomposed using multiple U(2)-based matrices. Unitary matrices' realization based on the Reck model is decomposed by multiplying matrices from one side in succession. It is not necessary to multiply matrices from only one side to decompose the unitary matrix. The decomposition can be done by multiplying matrices from both sides. The U(3) case and U(4) case are given as an example.

U(3) case:

$$T_{2,3}T_{1,2}U(3)T_{1,2}^{-1} = P \rightarrow U(3) = T_{1,2}^{-1}T_{2,3}^{-1}PT_{1,2}. \tag{2.46}$$

U(4) case:

$$T_{3,4}T_{2,3}U(4)T_{1,2}^{-1}T_{3,4}^{-1}T_{2,3}^{-1}T_{1,2}^{-1} = P \rightarrow U(4) = T_{2,3}^{-1}T_{3,4}^{-1}PT_{1,2}T_{2,3}T_{3,4}T_{1,2}. \tag{2.47}$$

The unitary matrix decomposition is possible, and this has been experimentally realized and demonstrated (Clements et al., 2016; Metcalf et al., 2013).

Any unitary matrices can be generated using the models above. Among all the higher dimensional unitary matrices, we will focus on the the Grover matrix and the Fourier matrix. The Grover matrix is particularly interesting because of its symmetry under cyclic exchange of labels.

$$Grover = \begin{pmatrix} -1+\frac{2}{N} & \frac{1}{N} & \cdots & \frac{1}{N} \\ \frac{1}{N} & -1+\frac{2}{N} & \cdots & \frac{1}{N} \\ \vdots & \vdots & \ddots & \vdots \\ \frac{1}{N} & \frac{1}{N} & \cdots & -1+\frac{2}{N} \end{pmatrix}, \tag{2.48}$$

$$Fourier = \frac{1}{\sqrt{N}} \begin{pmatrix} 1 & 1 & 1 & \dots & 1 \\ 1 & \omega & \omega^2 & \dots & \omega^{(N-1)} \\ 1 & \omega^2 & \omega^4 & \dots & \omega^{2(N-1)} \\ \vdots & \vdots & \vdots & \ddots & \vdots \\ 1 & \omega^{(N-1)} & \omega^{2(N-1)} & \dots & \omega^{(N-1)(N-1)} \end{pmatrix}. \tag{2.49}$$

Chapter 3

Directionally-Unbiased Linear-Optical Multiports

3.1 Introduction

Over the past several decades, quantum computers have sparked significant interest, based on their potential advantages over conventional computing devices in certain tasks. Several quantum algorithms have been proposed for quantum computers (Shor, 1994; Grover, 1996), but it is clear that a substantial amount of time and resources are still required in order for general-purpose quantum computing to become a reality. Therefore, it is beneficial to revisit Feynman's original approach of creating special-purpose quantum computing devices that are capable of efficiently simulating specific features of a complex physical system by utilizing another simple and controllable quantum device (i.e. a quantum simulator or "analog" quantum computer) (Feynman, 1982). Quantum walks (Aharonov et al., 1993; Portugal, 2013; Feldman and Hillery, 2004) on complex graphs are good candidates for executing this approach, given the statistical nature of quantum mechanical phenomena. Furthermore, quantum walks on graphs have been shown to possess the capability of performing a universal computation (Childs, 2009). Linear optics is one plausible physical architecture for implementing quantum walks due to its stability to decoherence, room temperature operation, and scalability through on-chip integration.

A beam splitter (BS) (Saleh et al., 1991) is a device of central importance in realizing any discrete quantum unitary operation (Reck et al., 1994; Carolan et al., 2015), Hadamard-coin-

based quantum walks (Kempe, 2003), and other quantum interferometer-based experiments (Spring et al., 2013; Clements et al., 2016; Crespi et al., 2013a; De Nicola et al., 2014; Wang et al., 2018; Peruzzo et al., 2011). It is of interest to look at BS properties from the point of their symmetries. The BS has reflection and time-reversal invariance allowing the two input and two output ports to be interchanged. However, the BS is asymmetric and directionally-biased in the sense that an input photon cannot leave the same port through which it entered. This property of directional bias forces standard implementations of linear-optical quantum walks to form a unidirectional, expanding tree of possible optical paths, leading to a rapid increase in the hardware requirement needed to cover all possible probability amplitudes that are present in the Hamiltonian of the physical system under investigation (Crespi et al., 2013a; Metcalf et al., 2013; Broome et al., 2013). Similarly, all the optical multiports currently in use, such as tritters, share the same directionally-biased behavior (Spagnolo et al., 2013a; Weihs et al., 1996a). The multiports considered here have some similarities with a previously-introduced type of non-directional coupler known as a reflective star coupler (Zhang et al., 2000; Saleh and Kogelnik, 1988). Nonetheless, unlike star couplers, the directionally unbiased multiports discussed here have relative output amplitudes at each port that can be readily tuned to desired values without dynamically changing splitting ratios of beam splitters. This additional flexibility opens up a broad range of new applications. It is possible to construct a directionally-unbiased multiport by combining several linear-optical elements such as beam splitters and mirrors to form a single compound device (Simon et al., 2016).This multiport can be seen as the physical implementation of a scattering vertex for quantum walks in undirected graph systems, with the added benefit of easy control of the unitary transformation between input and output amplitudes. By connecting multiple copies of such devices one could carry out a variety of different experiments, such as 1D and higher-dimensional discrete quantum walks, realizing group transformation with Bell states (Simon et al., 2016), simulation of physical system Hamiltonians (Simon et al., 2017a), and

experimental exploration of topological phases (Simon et al., 2017b) using linear optics. In particular, in quantum walk applications, because of direction reversibility, the walk can occur along a single line, rather than engaging additional spatial modes perpendicular to the overall direction of motion imposed by the beam splitter.

In this chapter, we report on the first experimental demonstration of a directionally-unbiased linear-optical three-port and explore its properties. The three-ports are then extended to four-ports. We introduce potential bulk optics-based implementation and coupler based schemes.

3.2 Directionally Unbiased Three-Ports

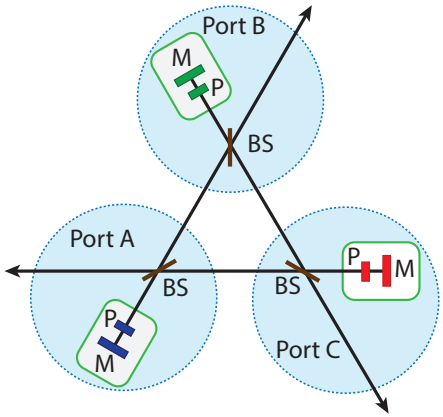

Figure 3·1: Theoretical implementation of three-ports. Each port is labeled as port A, port B and port C. Each port is adjacent to a unit containing a non-polarizing beam splitter (BS), a phase plate (P) and a mirror (M). A photon can enter and leave through any of the three ports.

We focus on the simplest case, where the number of ports is $m = 3$. It has three inputs/outputs labeled as port A, B, and C. The multiport internal structure consists of three beam splitters with a 50/50 transmission reflection ratio and three mirror units with control over the phases of reflected photons. When the photon enters from port A, it is either

transmitted or reflected upon hitting the first, as well as subsequent, beam splitters. The reflected photon acquires $\frac{\pi}{2}$ phase shift at each beam splitter, with additional controllable phase shifts from phase plates. The photon then accumulates different phases for each potential path through the system; this phase depends on the number of encounters with beam splitters and mirror units, equivalently, on the number of edges traversed.

In Fig. 3·1, each mirror unit consists of a phase plate (P) and a mirror (M), which together impart some controllable total phase shift ϕ at each encounter. The multiport input/output properties are defined by a *coherent summation* of amplitudes of all possible paths having the same input and output. In order to avoid turning this into a classical, decoherent sum over probabilities, information on which internal path each photon took must remain inaccessible. Therefore, the detection of the photon output probability at ports A, B, and C must be performed over a time much longer than the transit time between beam splitters in order to avoid paths to be distinguished by exit time. After a sufficiently long time, the output probability amplitudes for the photon to exit at the three ports after entering the multiport at port A are given by:

$$\begin{aligned} A \to A = {} & \frac{1}{4}e^{i\phi_C} + \frac{1}{4}e^{i\phi_B} - i\frac{1}{8}e^{i(\phi_B+\phi_C)} - i\frac{1}{8}e^{i(\phi_B+\phi_C)} + \frac{1}{16}e^{i(\phi_A+\phi_B+\phi_C)} + \frac{1}{16}e^{i(\phi_A+\phi_B+\phi_C)} \\ & - \frac{1}{16}e^{i(\phi_B+\phi_C+\phi_B)} - \frac{1}{16}e^{i(\phi_C+\phi_B+\phi_C)} - \frac{1}{16}e^{i(\phi_B+\phi_A+\phi_B)} - \frac{1}{16}e^{i(\phi_C+\phi_A+\phi_C)} + \ldots \end{aligned} \tag{3.1}$$

$$\begin{aligned} A \to B = {} & i\frac{1}{2} - \frac{1}{4}e^{i\phi_C} - i\frac{1}{8}e^{i(\phi_A+\phi_B)} + i\frac{1}{8}e^{i(\phi_A+\phi_C)} + i\frac{1}{8}e^{i(\phi_B+\phi_C)} + \frac{1}{16}e^{i(\phi_A+\phi_B+\phi_C)} \\ & - \frac{1}{16}e^{i(\phi_A+\phi_B+\phi_C)} - \frac{1}{16}e^{i(\phi_A+\phi_B+\phi_C)} + \frac{1}{16}e^{i(\phi_C+\phi_B+\phi_C)} + \frac{1}{16}e^{i(\phi_C+\phi_A+\phi_C)} + \ldots \end{aligned} \tag{3.2}$$

$$A \to C = i\frac{1}{2} - \frac{1}{4}e^{i\phi_B} + i\frac{1}{8}e^{i(\phi_A+\phi_B)} - i\frac{1}{8}e^{i(\phi_A+\phi_C)} + i\frac{1}{8}e^{i(\phi_B+\phi_C)} + \frac{1}{16}e^{i(\phi_A+\phi_B+\phi_C)} - \frac{1}{16}e^{i(\phi_A+\phi_B+\phi_C)} - \frac{1}{16}e^{i(\phi_A+\phi_B+\phi_C)} + \frac{1}{16}e^{i(\phi_B+\phi_C+\phi_B)} + \frac{1}{16}e^{i(\phi_B+\phi_A+\phi_B)} + \ldots, \tag{3.3}$$

where ϕ_A, ϕ_B, ϕ_C are the total phases acquired by the photon from mirror units A, B, C, respectively, and a $\frac{\pi}{2}$ phase is acquired from each beam splitter reflection. Small additional terms of the order $\left(\frac{1}{2}\right)^5$ or higher have been left out from consideration. Similar equations can be obtained for inputs B and C. Here, we have also assumed that phase shifts gained from propagation between mirror units are integer multiples of 2π so that they play no role.

After a sufficient number of beamsplitter encounters, the output amplitudes converge to fixed values (Simon et al., 2016). Let N be the number of beamsplitter encounters for the photon before exiting the multiport or, equivalently, the number of time steps, where the unit of time is the travel time between consecutive beamsplitter encounters. The cumulative probability to exit a multiport as a function of N is given in Table. 3.1. One could observe that after N = 8 in over 99 percent of trials of the photons have left the system, as indicated in Table. 3.1.

A transfer matrix expression for the multiport can be obtained by substituting specific phase settings in Eq. 3.1, 3.2, and 3.3. We set $\phi_A = \phi_B = \phi_C = \frac{\pi}{6}$ in this paper to explore the most symmetric case that would make this unit suitable for quantum walks on unstructured graphs. Carrying out an exact summation of the series in Eqs. 3.1-3.3, the resulting expected transfer matrix is:

$$U = \begin{pmatrix} U_{A\to A} & U_{B\to A} & U_{C\to A} \\ U_{A\to B} & U_{B\to B} & U_{C\to B} \\ U_{A\to C} & U_{B\to C} & U_{C\to C} \end{pmatrix} = \frac{1}{\sqrt{3}} e^{\frac{2\pi i}{3}} \begin{pmatrix} e^{\frac{-2\pi i}{3}} & 1 & 1 \\ 1 & e^{\frac{-2\pi i}{3}} & 1 \\ 1 & 1 & e^{\frac{-2\pi i}{3}} \end{pmatrix} \tag{3.4}$$

We can choose different phases to implement different matrices. If the phase value $\phi_A = \phi_B = \phi_C = \frac{3\pi}{2}$ is chosen then, the resulting matrix becomes Grover matrix.

N	A exit	B exit	C exit	Exit Probability	Cumulative Exit Probability
2	0	$\frac{i}{2}$	$\frac{i}{2}$	$\frac{1}{2}$	0.5
4	$\frac{-i}{2}$	$\frac{i}{4}$	$\frac{i}{4}$	$\frac{3}{8}$	0.875
6	$\frac{i}{4}$	$\frac{-i}{8}$	$\frac{-i}{8}$	$\frac{3}{32}$	0.96875
8	$\frac{-i}{8}$	$\frac{i}{16}$	$\frac{i}{16}$	$\frac{3}{128}$	0.99219
10	$\frac{i}{16}$	$\frac{-i}{32}$	$\frac{-i}{32}$	$\frac{3}{512}$	0.99805

Table 3.1: Probability amplitudes for the port A, B, and C, exit probability in respect to a specific number of BS encounters, and the cumulative exit probability are shown. Columns A exit, B exit, and C exit represent exit probability amplitude at each port with the initial photon entering at port A. Exit Probability shows the exit probability for each possible number of beam splitter hits. The cumulative exit probability is obtained from summing all the exit probabilities. As N increases, the cumulative exit probability quickly approaches 1 and a photon leaves the unit.

$$U = \begin{pmatrix} U_{A\to A} & U_{A\to B} & U_{A\to C} \\ U_{B\to A} & U_{B\to B} & U_{B\to C} \\ U_{C\to A} & U_{C\to B} & U_{C\to C} \end{pmatrix} = \frac{1}{3}\begin{pmatrix} -2 & 1 & 1 \\ 1 & -2 & 1 \\ 1 & 1 & -2 \end{pmatrix} \tag{3.5}$$

The transfer matrix acts on an input state via the transformation: $|\psi_{output}\rangle = U\,|\psi_{input}\rangle$. Squaring the modulus of each matrix element gives the final transition probability distribution that should be observed in an experiment.

$$P = \begin{pmatrix} |U_{A\to A}|^2 & |U_{A\to B}|^2 & |U_{A\to C}|^2 \\ |U_{B\to A}|^2 & |U_{B\to B}|^2 & |U_{B\to C}|^2 \\ |U_{C\to A}|^2 & |U_{C\to B}|^2 & |U_{C\to C}|^2 \end{pmatrix} = \frac{1}{3}\begin{pmatrix} 1 & 1 & 1 \\ 1 & 1 & 1 \\ 1 & 1 & 1 \end{pmatrix} \tag{3.6}$$

3.2.1 Directionally-Unbiased Linear-Optical Four-Port Devices

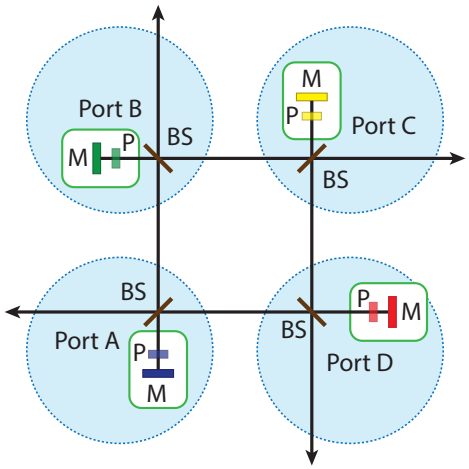

Figure 3·2: Directionally-unbiased linear-optical four-port operation. It has the same configuration as Fig. 3·1 with one extra input/output port.

The dimensionality and the number of optical elements are increased in the case of a four-port device as illustrated in Fig. 3·2. It needs to be noted that four ports are slightly different from the three ports because of the number of beam splitter encounters before the input photon leaves the system. For instance, the shortest path for Port A to Port B would be $A \to B$ with one beam splitter encounter. likewise, the shortest path for Port A to Port C would be $A \to B \to C$ or $A \to D \to C$ with two beam splitter encounters. The probability amplitude is lower for the path A to C because the photon encounters one extra beam splitter. This path-dependent amplitude difference needs to be considered for higher-dimensional multiport implementation.

$$\begin{aligned} A \to A \quad &= \tfrac{1}{4}e^{i\phi_B} + \tfrac{1}{4}e^{i\phi_D} - \tfrac{1}{16}e^{i(\phi_B+\phi_C+\phi_B)} + \tfrac{1}{16}e^{i(\phi_B+\phi_C+\phi_D)} - \tfrac{1}{16}e^{i(\phi_D+\phi_C+\phi_D)} \\ &\quad + \tfrac{1}{16}e^{i(\phi_D+\phi_C+\phi_B)} - \tfrac{1}{16}e^{i(\phi_B+\phi_A+\phi_B)} - \tfrac{1}{16}e^{i(\phi_D+\phi_A+\phi_D)} + \ldots, \end{aligned} \tag{3.7}$$

$$A \to B \quad = i\tfrac{1}{2} - i\tfrac{1}{8}e^{i(\phi_D+\phi_C)} - i\tfrac{1}{8}e^{i(\phi_B+\phi_A)} + i\tfrac{1}{8}e^{i(\phi_B+\phi_C)} + i\tfrac{1}{8}e^{i(\phi_D+\phi_A)} + \ldots, \tag{3.8}$$

$$A \to C \quad = -\tfrac{1}{4}e^{i\phi_B} - \tfrac{1}{4}e^{i\phi_D} - \tfrac{1}{16}e^{i(\phi_B+\phi_C+\phi_D)} + \tfrac{1}{16}e^{i(\phi_B+\phi_A+\phi_B)} + \tfrac{1}{16}e^{i(\phi_D+\phi_C+\phi_D)} - \tfrac{1}{16}e^{i(\phi_D+\phi_C+\phi_B)} + \tfrac{1}{16}e^{i(\phi_B+\phi_A+\phi_B)} + \tfrac{1}{16}e^{i(\phi_D+\phi_A+\phi_D)} + \ldots, \tag{3.9}$$

$$A \to D = i\frac{1}{2} - i\frac{1}{8}e^{i(\phi_B+\phi_C)} - i\frac{1}{8}e^{i(\phi_D+\phi_C)} - i\frac{1}{8}e^{i(\phi_D+\phi_A)} + i\frac{1}{8}e^{i(\phi_B+\phi_A)} + \ldots. \tag{3.10}$$

The final transfer matrix consists of 16 (input $\to$ output) transition amplitudes:

$$U_{multiport} = \begin{pmatrix} U_{A\to A} & U_{B\to A} & U_{C\to A} & U_{D\to A} \\ U_{A\to B} & U_{B\to B} & U_{C\to B} & U_{D\to B} \\ U_{A\to C} & U_{B\to C} & U_{C\to C} & U_{D\to C} \\ U_{A\to D} & U_{B\to D} & U_{C\to D} & U_{D\to D} \end{pmatrix}. \tag{3.11}$$

The probability distribution is obtained in the same way as the three-ports by multiplying its complex conjugates for each matrix entry.

3.3 Experimental Demonstration of Directionally-Unbiased Three-Ports

We introduced theoretical designs of three- and four-ports in previous subsections. The operation of a directionally-unbiased symmetric three-edge vertex device has been demonstrated by characterizing probability distribution matrix elements responsible for all possible photon input/output transitions. The actual experimental setup is shown in Fig. 3·3. A continuous-wave 10 mW laser operating at 633 nm (NECSEL single longitudinal mode) with a very long coherence length ($>$ 1 km) was used. This condition ensures the coherent superposition requirement for all possible photon paths inside the unit. The beam splitters have a 50/50 transmission/reflection ratio at 633 nm. The phase shifts imparted by the mirror units are controlled by piezo actuators on translation stages. The input beam was attenuated to a single-photon level with polarizers. The multiport arrangement indicated in Fig. 3·3 is for the input at port A and outputs from A, B, and C.

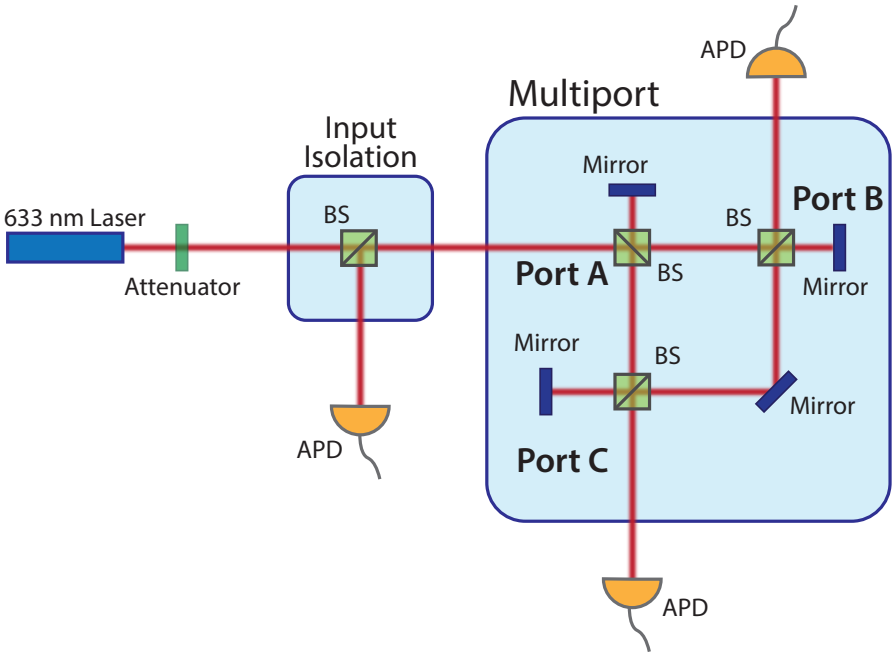

Figure 3·3: Experimental setup for detecting probabilistic single-photon distribution in a three-port with a photon entering at the port A. A laser with a long coherence length (>1 km) operates at 633 nm. The input beam is attenuated to a single-photon level prior to entering the multiport. The input isolation allows decoupling the input photon from the one exiting through the same port A. This multiport consists of three beam splitters, three mirrors with piezo actuators to control internal phases, and an extra mirror in one arm. The number of exiting photons is counted by a single-photon avalanche diode modules (APD). Phases in each branch of the multiport are set to $\frac{\pi}{6}$ using mirror units.

This corresponds to the first matrix row in Eq. 3.2. The beam splitter at port A serves as a 50% isolation device separating half of the output photons statistically into a different path for detection. An optical circulator would be a better device to use in the future in order to separate all of the outgoing photons from the incoming ones. A similar setup is used to measure transitions with input at port B and port C. This would correspond to rows 2 and 3 in Eq. 3.2, respectively. The outgoing photons at each port were counted using fiber-coupled single-photon avalanche diodes (PerkinElmer SPCM-AQR-15-FC), as indicated in Fig. 3·3. The real experimental configuration is equivalent to the theoretical schematic depicted in Fig. 3·1, despite the slightly different shape; this more complex experimental arrangement is necessary in the current case because the equidistant triangular setup described in section

3.2 cannot be easily realized with cube beam splitters. The distance between beam splitters A-B and A-C is set to be identical, while B-C is set to be twice as long as A-B and has one additional mirror. This does not affect the overall probability distribution in the matrix Eq. 3.4 when the photon coherence is sufficiently long. What is important is the phase balance in all possible paths inside the multiport. The mirror units are translated for an additional phase π to recover the balance due to one extra mirror presence. Alternatively, this extra π phase can be compensated by arranging the structure so that all three paths have the same number of mirrors. The same result could be achieved by inserting a phase plate in the path with an extra mirror.

The weak photon source statistics follow a Poisson distribution, and the input coherent laser beam is attenuated to the single-photon level, meaning its average photon number during the detection interval must be smaller than 1. Our single-photon avalanche photodetector integration time is 35 ns. The average photon number within the detector integration window is below 0.1 when the input beam is attenuated to 1 nW average power. The detector quantum efficiency is 0.6 at the 633 nm wavelength of the source.

The system under consideration could be considered as a coherent superposition of several interferometers with three independent phase controls. The detected outcome at each port forms an interference pattern of intensity as a function of those phases. The quality of the multiport alignment is verified by determining the visibility of such interference patterns:

$$V = \frac{n_{max} - n_{min}}{n_{max} + n_{min}}, \tag{3.12}$$

where n_{max} is the maximum number of detected photons, n_{min} is the minimum number of detected photons.

The problem of setting all three phases to the same value is not very straightforward, since the phases are relative parameters. Interference contour maps were generated to cover all possible phases from 0 to 2π in order to find a position when all three of them have the

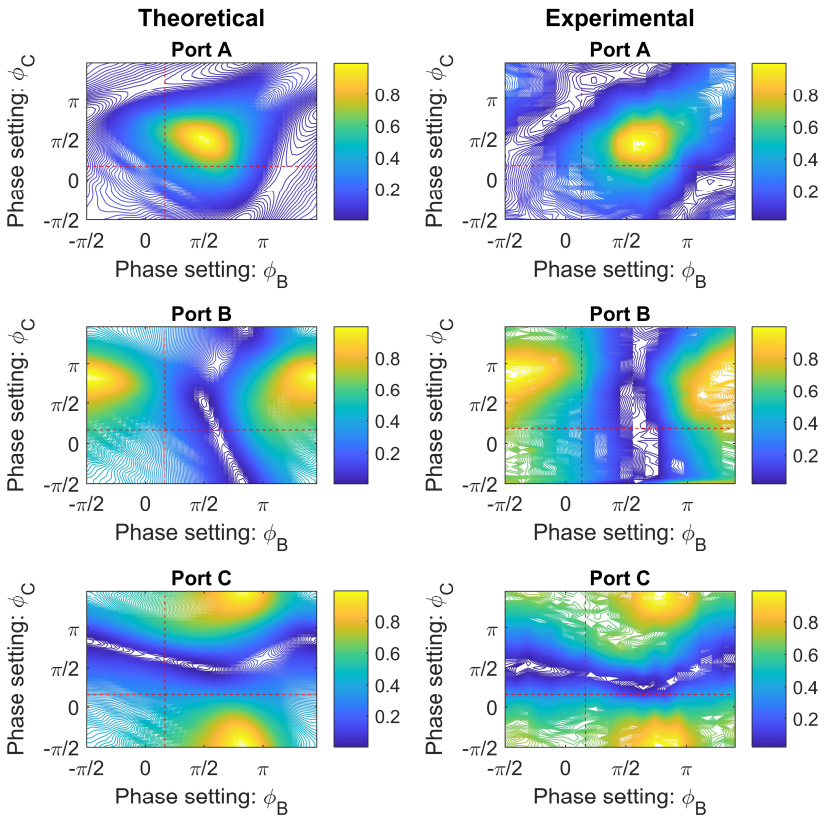

Figure 3·4: Theoretical simulation (left) and experimental results (right) at $\phi_A = \frac{\pi}{6}$.The contour graphs represent probability distribution for the input-output combinations A-A, A-B, and A-C where the minimum is close to 0 and maximum is close to 1. Light color coding (yellow) corresponds to a high probability and dark color (blue) indicates low probability. The phase at the mirror unit A is set to $\phi_A = \frac{\pi}{6}$ for all three plots. The left contour graphs are the theoretical simulation. Dashed lines are drawn at $\phi_B = \frac{\pi}{6}$ and $\phi_C = \frac{\pi}{6}$. The cross section indicates the point when all three phases (ϕ_A,ϕ_B,ϕ_C) = ($\frac{\pi}{6}$,$\frac{\pi}{6}$,$\frac{\pi}{6}$). The contour graphs in the right column present the results of experimental observation. The dashed lines are drawn to indicate phase settings at $\frac{\pi}{6}$. The phase step in the contour graph is $\frac{\pi}{15}$.

same $\frac{\pi}{6}$ value (see Fig. 3·3).

The distance between consecutive beam splitter hits in the multiport is marginally less than 30 cm. Any incident photon will exit the system with a probability of 0.998 after N = 10 interactions (Simon et al., 2016), so one has to ensure a coherent (indistinguishable) travel of the photon over about 300 cm in this case. This is significantly shorter than the coherence length of the source used in our experiment ($>$ 1 km). One should point out that

dividing this number by the speed of light we obtain an estimate for a maximum time any photon would stay inside the multiport (about 10 ns).

The optical table was passively stabilized with active mechanical vibration isolation. By this means, the required interferometric stability of operation was achieved over a 5 hour period, which was sufficient for automatic scans of all required high-visibility interference patterns illustrated in Fig. 3·4. In future free-space experiments requiring greater data acquisition times, active stabilization loops may be needed. The eventual transfer of this configuration into a waveguided on-chip design will help significantly to enhance performance stability and transverse alignment and to reduce the long-term longitudinal phase drift. This offers extensive opportunities for miniaturizing the device on a chip-scale, allowing greater compactness and stability, as well as reducing the coherence requirements.

Multiple contour maps were obtained by translating two mirror units B and C (one at a time) when the phase from a mirror unit ϕ_A is fixed at a certain value. Then the procedure was repeated multiple times for new values of ϕ_A. A subset of such contour maps corresponding to the situation when the photon is inserted at port A is illustrated in Fig. 3·4. The situation when the photon enters at ports B or C generates a similar set of contour plots. The comparison of such experimental contour maps with those obtained in theoretical simulation enables one to identify a point corresponding to $\frac{\pi}{6}$ phase shift value in all three phases (indicated by a dashed line). The final probability distribution for single photons to enter and exit any of the ports has been performed at these particular phase settings from all three mirror units A, B, and C.

In order to compare to the real experimental situation, Eqs. 3.1 - 3.3 must be modified to account for the additional mirror present (see Fig. 3·3). This is done by shifting each phase acquired from the mirror units by π. The resulting equations will have the following modifications: $\phi_A \rightarrow \phi_A + \pi$, $\phi_B \rightarrow \phi_B + \pi$, and $\phi_C \rightarrow \phi_C + \pi$. Under these conditions, $A \rightarrow A$ changes sign, $A \rightarrow B$ and $A \rightarrow C$ remain the same, with similar changes for other input

ports. The theoretical unitary transfer matrix corresponding to the current experimental configuration is now:

$$U = \frac{1}{\sqrt{3}} e^{\frac{2\pi i}{3}} \begin{pmatrix} -e^{\frac{-2\pi i}{3}} & 1 & 1 \\ 1 & -e^{-\frac{2\pi i}{3}} & -1 \\ 1 & -1 & -e^{-\frac{2\pi i}{3}} \end{pmatrix} \tag{3.13}$$

This insignificant phase modification in the unitary transfer matrix Eq. 3.13 is a reflection of the need to use several bulk optical elements (such as beam splitters and mirrors) during the first experimental implementation. (Currently, available technology would allow the original theoretically-formulated unitary transfer matrix indicated in Eq. 3.4 to be realized using a waveguided platform in an integrated configuration that executes all features of the multiport in Fig.3·1. Such an on-chip configuration would be highly desirable due to improved compactness and stability.) This *phase modification* leaves the final *probability distribution* for the transfer matrix *unchanged* from that of Sec. 3.2:

$$P = \frac{1}{3} \begin{pmatrix} 1 & 1 & 1 \\ 1 & 1 & 1 \\ 1 & 1 & 1 \end{pmatrix} \tag{3.14}$$

3.4 Experimental Results

The quality of the overall multiport alignment has been verified by observing a single-photon interference at each port by sequentially feeding a single-photon input state into each of ports A, B, and C. The experimentally observed visibility is calculated for all 9 possible outcomes corresponding to a photon state inserted in port A, port B, and port C. Three plots corresponding to insertion at Port A case are illustrated in Fig. 3·4 (right column). An average observed visibility of 0.97 ± 0.01 was achieved. A phase step of $\frac{\pi}{15}$ was taken between each point on the plots. All presented data are based on direct observation, with no background subtraction performed. A small reduction in the visibility came from the detector dark counts, slight reflection on the beam splitter surfaces, and from the minor

imperfection of beam splitter surface alignment that results in the imperfect overlap of the beams. All experimental probability detection maps for each port in Fig. 3·4 are normalized by their maxima to obtain a probability distribution. The contour map in the right column of Fig. 3·4 represents the photon count distribution for the fixed $\phi_A = \frac{\pi}{6}$ and phase sweeps from 0 to 2π for ϕ_B and ϕ_C by changing the voltages on piezo actuators responsible for the position of corresponding metal mirrors in space. Each map is compared with its theoretical simulations in the left column in Fig. 3·4. The same method and similar contour maps were used for detecting outcome probabilities when a single photon has been inserted in B and C. The probability distribution for the photon to transition between any pair of ports has been reconstructed by statistically averaging the raw data over 1.8 s.

The final reconstructed probability matrix at $(\phi_A,\phi_B,\phi_C) = (\frac{\pi}{6},\frac{\pi}{6},\frac{\pi}{6})$ is given by:

$$P_{exp} = \begin{pmatrix} 0.332 \pm 0.007 & 0.343 \pm 0.007 & 0.340 \pm 0.004 \\ 0.340 \pm 0.005 & 0.339 \pm 0.006 & 0.328 \pm 0.008 \\ 0.332 \pm 0.005 & 0.340 \pm 0.012 & 0.338 \pm 0.007 \end{pmatrix} \tag{3.15}$$

Losses generally play a negative role in quantum optics experiments. However, the role of losses in the case considered here is not significant. The device is probabilistic and operates with one photon at a time in the system. The loss of a photon simply results in discarding this particular trial from detection and recording of all possible outcomes. This does not affect the quality of the next trial and does not degrade the overall visibility of the detected outcome. The effect of losses shows up simply as an increase in the required accumulation time needed to get sufficient statistics when characterizing the multiport. The probability distribution (input-output) matrix elements were characterized one by one and are independent of one another. These are obtained from a contour map using visibility as the major quality parameter. The loss does not affect the visibility normalization process since we have the same loss across the contour map.

The interference patterns observed at each port depend on the fact that all of the possible paths within the multiport remain coherent with one another. The high visibility observed in

each output port, therefore, indicates a high level of mutual coherence of the output at the different ports, a requirement for multi-photon (and especially entangled-photon) quantum information processing applications.

3.4.1 Constructing Reversible Optical Tritter and Quarter

We can suggest an alternative approach to these directionally-unbiased devices. It has been shown earlier that traditional integrated optical 3×3 and 4×4 couplers are directionally-biased devices. However, placing mirrors at each of the output ports of the device helps to eliminate this directional bias and return the optical signal back to any of the input ports. This type of reversible design has been also introduced in the area of linear interferometric networks and has been sometimes called a generalized Michelson interferometer (Vance and Barrow, 1995; Schwelb, 1998). The reversibility is introduced by mirrors, while additional phase shifters can be introduced before the mirrors. Both 3×3 and 4×4 implementations are illustrated in Fig. 3·5. The reversed tritter can be realized using the same design formalism as a generalized Michelson interferometer. The input photon state is transformed by a tritter matrix, phase shifters, and a transposed tritter matrix.

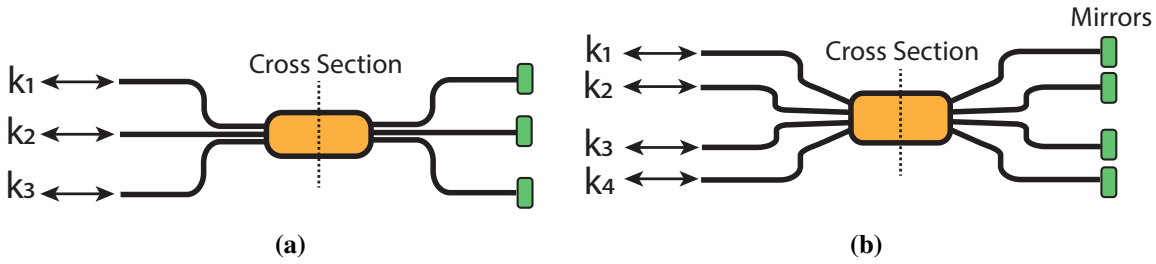

Figure 3·5: (**a**) Reversible integrated tritter. The photon propagation direction is reversed by placing mirrors at the end of the coupling region. (**b**) Reversible integrated quarter. It has the same configuration as (**a**) with extra input and output port.

A reversible tritter device can be constructed using the same approach as a michelson interferometer where an incoming forward propagation state gets transformed by the direc-

tional tritter and the propagation direction is flipped by the mirror. The flipped amplitude is transformed by the tritter device again. This is described using a matrix method.

$$U_{RevTritter} = U_{IntTritter}^{T} U_{phase} U_{IntTritter}, \tag{3.16}$$

$$U_{phase} = \begin{pmatrix} e^{i\phi_A} & 0 & 0 \\ 0 & e^{i\phi_B} & 0 \\ 0 & 0 & e^{i\phi_C} \end{pmatrix}, \tag{3.17}$$

$$\begin{aligned} U_{IntTritter} &= \frac{e^{-\beta z i}}{3} \begin{pmatrix} 2e^{\kappa z i} + e^{-2\kappa z i} & -e^{\kappa z i} + e^{-2\kappa z i} & -e^{\kappa z i} + e^{-2\kappa z i} \\ -e^{\kappa z i} + e^{-2\kappa z i} & 2e^{\kappa z i} + e^{-2\kappa z i} & -e^{\kappa z i} + e^{-2\kappa z i} \\ -e^{\kappa z i} + e^{-2\kappa z i} & -e^{\kappa z i} + e^{-2\kappa z i} & 2e^{\kappa z i} + e^{-2\kappa z i} \end{pmatrix} \\ &= \frac{e^{-\beta z i}}{3} \begin{pmatrix} A & B & B \\ B & A & B \\ B & B & A \end{pmatrix}, \end{aligned} \tag{3.18}$$

where $A = 2e^{\kappa z i} + e^{-2\kappa z i}$ and $B = -e^{\kappa z i} + e^{-2\kappa z i}$. Putting all the pieces together, the final expression is:

$$U_{RevTritter} = \frac{e^{-2\beta z i}}{9} \begin{pmatrix} e^{i\phi_A} AA + e^{i(\phi_B+\phi_C)} BB & e^{i(\phi_A+\phi_B)} AB + e^{i\phi_C} BB & e^{i(\phi_A+\phi_C)} AB e^{i\phi_B} BB \\ e^{i(\phi_A+\phi_B)} AB + e^{i\phi_C} BB & e^{i(\phi_A+\phi_C)} BB + e^{i\phi_B} AA & e^{i\phi_A} BB + e^{i(\phi_B+\phi_C)} AB \\ e^{i(\phi_A+\phi_C)} AB + e^{i\phi_B} BB & e^{i\phi_A} BB + e^{i(\phi_B+\phi_C)} AB & e^{i(\phi_A+\phi_B)} BB + e^{i\phi_C} AA \end{pmatrix}. \tag{3.19}$$

$$U_{phase} = \begin{pmatrix} e^{i\phi_A} & 0 & 0 & 0 \\ 0 & e^{i\phi_B} & 0 & 0 \\ 0 & 0 & e^{i\phi_C} & 0 \\ 0 & 0 & 0 & e^{i\phi_D} \end{pmatrix}, \tag{3.20}$$

where ϕ_A, ϕ_B, ϕ_C and ϕ_D are phase shifts introduced before the second device encounter.

$$U_{IntQuarter} = \frac{e^{\beta z i}}{4} \begin{pmatrix} A & B & C & B \\ B & C & B & A \\ C & B & A & B \\ B & A & B & C \end{pmatrix}, \tag{3.21}$$

where $A = 2e^{-\kappa_2 zi} + e^{-2\kappa_1 zi+\kappa_2 zi} + e^{2\kappa_1 zi+\kappa_2 zi}$, $B = -e^{-2\kappa_1 zi+\kappa_2 zi} + e^{2\kappa_1 zi+\kappa_2 zi}$, and $C = -2e^{-\kappa_2 zi} + e^{-2\kappa_1 zi+\kappa_2 zi} + e^{2\kappa_1 zi+\kappa_2 zi}$. The reversible quarter matrix is then derived from the equation below.

$$U_{RevQuarter} = U_{IntQuarter}^{T} U_{phase} U_{IntQuarter}. \tag{3.22}$$

3.5 Specific Transfer Matrix Examples Using Reversible Linear-Optical Devices

We consider several specific experimental configurations for an efficient realization of quantum walks in higher dimensions using linear optical devices and exploiting the very important feature of optical reversibility. We look into specific phase values and corresponding transfer matrices using formalisms covered in previous sections. The focus here is on realization of the Fourier matrix and the Grover matrix using directionally-unbiased linear-optical multiports, and reversible optical tritter and quarter configurations.

3.5.1 The Fourier Matrix Realization

A three-dimensional Fourier matrix has the form:

$$U_{Fourier} = \frac{1}{\sqrt{3}} \begin{pmatrix} 1 & 1 & 1 \\ 1 & \omega_3 & \omega_3^2 \\ 1 & \omega_3^2 & \omega_3 \end{pmatrix}, \tag{3.23}$$

where $\omega_3 = e^{-\frac{2\pi i}{3}}$.

This matrix can be generated with a reversible tritter containing phase shifters at all three ports, and directionally-unbiased linear-optical three-ports can perform the same job as well. For a reversible system, an input photon experiences the same phase shifts twice from the same phase shifters. $U_{phasein}$ and $U_{phaseout}$ would take care of such phase shifts. Fig. 3·6 is a reversible tritter with phase shifters. Multiport designs are introduced in Section 3.2.1.

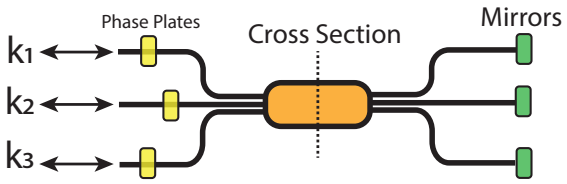

Figure 3·6: Reversible tritter with phase shifters. The yellow squares are phase shifters, and the green squares are mirrors.

The matrix generation is performed by multiplying $U_{phasein}$, U_{device}, and $U_{phaseout}$ in sequence. U_{device} can be any reversible optical device. The Fourier coin using the optical tritter is realized by the following procedure.

$$U_{Fourier} = U_{phaseout} U_{Tritter} U_{phasein}. \tag{3.24}$$

$$U_{phasein} = U_{phaseout} = \begin{pmatrix} e^{i\phi_a} & 0 & 0 \\ 0 & e^{i\phi_b} & 0 \\ 0 & 0 & e^{i\phi_c} \end{pmatrix}, \tag{3.25}$$

$$\begin{aligned} U_{Fourier} &= \begin{pmatrix} e^{-i\frac{\pi}{3}} & 0 & 0 \\ 0 & e^{i\frac{\pi}{3}} & 0 \\ 0 & 0 & e^{i\frac{\pi}{3}} \end{pmatrix} \frac{i}{\sqrt{3}} \begin{pmatrix} e^{i\frac{2\pi}{3}} & 1 & 1 \\ 1 & e^{i\frac{2\pi}{3}} & 1 \\ 1 & 1 & e^{i\frac{2\pi}{3}} \end{pmatrix} \begin{pmatrix} e^{-i\frac{\pi}{3}} & 0 & 0 \\ 0 & e^{i\frac{\pi}{3}} & 0 \\ 0 & 0 & e^{i\frac{\pi}{3}} \end{pmatrix} \\ &= \frac{i}{\sqrt{3}} \begin{pmatrix} 1 & 1 & 1 \\ 1 & e^{-i\frac{4\pi}{3}} & e^{-i\frac{2\pi}{3}} \\ 1 & e^{-i\frac{2\pi}{3}} & e^{-i\frac{4\pi}{3}} \end{pmatrix}, \end{aligned} \tag{3.26}$$

where ϕ_a, ϕ_b, ϕ_c are the phase shifts from phase shifters at the entrance ports. The reversible optical tritter and quarter can realize the Fourier coin when phases are set at specific values:

$$(\phi_A, \phi_B, \phi_C, \kappa z, \phi_a, \phi_b, \phi_c) = (\frac{10\pi}{9}, \frac{10\pi}{9}, \frac{10\pi}{9}, \frac{10\pi}{9}, -\frac{\pi}{3}, \frac{\pi}{3}, \frac{\pi}{3}), \tag{3.27}$$

where ϕ_A, ϕ_B, ϕ_C, and κz are phase values from mirror units of the reversible tritter and propagation distance of the coupling region.

Similarly, the unbiased three-port operation can realize the same matrix with the settings:

$$U_{Fourier} = U_{phaseout} U_{Three-port} U_{phasein}. \tag{3.28}$$

$$\begin{aligned} U_{Fourier} &= \begin{pmatrix} e^{i\frac{\pi}{3}} & 0 & 0 \\ 0 & e^{-i\frac{\pi}{3}} & 0 \\ 0 & 0 & e^{-i\frac{\pi}{3}} \end{pmatrix} \frac{1}{\sqrt{3}} e^{i\frac{2\pi}{3}} \begin{pmatrix} e^{-i\frac{2\pi}{3}} & 1 & 1 \\ 1 & e^{-i\frac{2\pi}{3}} & 1 \\ 1 & 1 & e^{-i\frac{2\pi}{3}} \end{pmatrix} \begin{pmatrix} e^{i\frac{\pi}{3}} & 0 & 0 \\ 0 & e^{-i\frac{\pi}{3}} & 0 \\ 0 & 0 & e^{-i\frac{\pi}{3}} \end{pmatrix} \\ &= \frac{1}{\sqrt{3}} e^{i\frac{2\pi}{3}} \begin{pmatrix} 1 & 1 & 1 \\ 1 & e^{-i\frac{4\pi}{3}} & e^{-i\frac{2\pi}{3}} \\ 1 & e^{-i\frac{2\pi}{3}} & e^{-i\frac{4\pi}{3}} \end{pmatrix}, \end{aligned} \tag{3.29}$$

when:

$$(\phi_A, \phi_B, \phi_C, \phi_a, \phi_b, \phi_c) = (\frac{\pi}{6}, \frac{\pi}{6}, \frac{\pi}{6}, \frac{\pi}{3}, -\frac{\pi}{3}, -\frac{\pi}{3}), \tag{3.30}$$

where ϕ_A, ϕ_B, and ϕ_C are the phase values for the directionally-unbiased three-port operation.

Four-dimensional matrices are generated using the same methods. The reversible quarter with phase shifters is given in Figure 3·7. Multiport designs are introduced in Section 3.2.1.

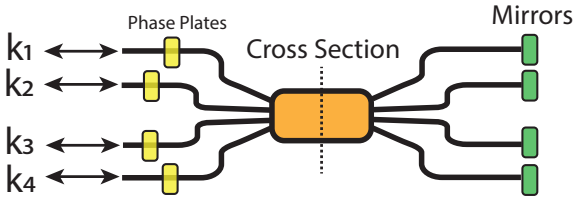

Figure 3·7: Reversible quarter with phase shifters. The yellow squares are phase shifters, and the green squares are mirrors.

The four-dimensional Fourier coin has the form of:

$$U_{Fourier} = \frac{1}{2}\begin{pmatrix} 1 & 1 & 1 & 1 \\ 1 & \omega_4 & \omega_4^2 & \omega_4^3 \\ 1 & \omega_4^2 & \omega_4^4 & \omega_4^6 \\ 1 & \omega_4^3 & \omega_4^6 & \omega_4^9 \end{pmatrix}, \tag{3.31}$$

where $\omega_4 = e^{-\frac{2\pi i}{4}}$.

$$U_{Fourier} = U_{phaseout} U_{Quarter} U_{phasein}, \tag{3.32}$$

$$U_{phasein} = U_{phaseout} = \begin{pmatrix} e^{i\phi_a} & 0 & 0 & 0 \\ 0 & e^{i\phi_b} & 0 & 0 \\ 0 & 0 & e^{i\phi_c} & 0 \\ 0 & 0 & 0 & e^{i\phi_d} \end{pmatrix}. \tag{3.33}$$

The reversible quarter can realize the Fourier coin as well with the phase settings equal to:

$$(\phi_A, \phi_B, \phi_C, \phi_D, \kappa z_1, \kappa z_2, \phi_a, \phi_b, \phi_c, \phi_d) = (\pi, \frac{\pi}{4}, \pi, \frac{5\pi}{4}, \frac{7\pi}{4}, \frac{7\pi}{8}, -\frac{\pi}{4}, -\frac{\pi}{2}, -\frac{\pi}{4}, \frac{\pi}{2}), \tag{3.34}$$

where $\phi_A, \phi_B, \phi_C, \phi_D$, and $\kappa z_1, \kappa z_2$ are phase values from the mirror units of the reversible tritter and propagation distance of the coupling region.

Four ports:

$$U_{Fourier} = U_{phaseout} U_{fourport} U_{phasein}, \tag{3.35}$$

when:

$$(\phi_A, \phi_B, \phi_C, \phi_D, \phi_a, \phi_b, \phi_c, \phi_d) = (0, \frac{\pi}{2}, 0, \frac{\pi}{2}, -\frac{\pi}{4}, -\frac{\pi}{4}, \frac{3\pi}{4}, -\frac{\pi}{4}), \tag{3.36}$$

where $\phi_A, \phi_B, \phi_C, \phi_D$ are the phase settings of the four-port operation.

3.5.2 The Grover Matrix Realization

The Grover matrix is realized using reversible designs as well. The procedure is identical to the Fourier matrix case. The three-dimensional Grover matrix takes the form of:

$$C_3 = \frac{1}{3}\begin{pmatrix} -1 & 2 & 2 \\ 2 & -1 & 2 \\ 2 & 2 & -1 \end{pmatrix}. \tag{3.37}$$

This can be realized using a reversible tritter with phase settings equal to:

$$(\phi_A, \phi_B, \phi_C, \kappa z) = (\frac{11\pi}{6}, \frac{11\pi}{6}, \frac{11\pi}{6}, \frac{11\pi}{6}), \tag{3.38}$$

or using an unbiased three-port with settings:

$$(\phi_A, \phi_B, \phi_C) = (\frac{3\pi}{2}, \frac{3\pi}{2}, \frac{3\pi}{2}). \tag{3.39}$$

The four-dimensional Grover matrix operator is given by:

$$C_4 = \frac{1}{2}\begin{pmatrix} -1 & 1 & 1 & 1 \\ 1 & -1 & 1 & 1 \\ 1 & 1 & -1 & 1 \\ 1 & 1 & 1 & -1 \end{pmatrix}, \tag{3.40}$$

which can be realized with a reversible quarter,

$$U_{Grover} = U_{phaseout} U_{Quarter} U_{phasein}. \tag{3.41}$$

The phase settings for this Grover matrix realization is done by:

$$(\phi_A, \phi_B, \phi_C, \phi_D, \kappa z_1, \kappa z_2) = (0, 0, 0, 0, \frac{\pi}{8}, \frac{\pi}{8}). \tag{3.42}$$

Similarly for the four ports:

$$U_{Grover} = U_{phaseout} U_{Four-ports} U_{phasein}, \tag{3.43}$$

$$(\phi_A, \phi_B, \phi_C, \phi_D) = (\frac{3\pi}{2}, \frac{3\pi}{2}, \frac{3\pi}{2}, \frac{3\pi}{2}). \tag{3.44}$$

3.6 Comparison between Directional- and Directionally-Unbiased Devices

Directional devices (the Reck and Clements decomposition model) can produce any unitary matrices U(N). However, when reversibility is introduced in the system (reversible tritters and directionally-unbiased linear-optical multiports), it imposes symmetry or the self-transpose property $U_{i,j} = U_{j,i}$, where i,j are matrix indices. Hence, reversible designs only produce the subset of symmetric unitary matrices. As an example, Eq. 3.45 is a unitary matrix, but it is not a self-transpose matrix.

$$U = \begin{pmatrix} 0 & 1 & 0 \\ 0 & 0 & 1 \\ 1 & 0 & 0 \end{pmatrix}. \tag{3.45}$$

Regardless, this reversible design can produce important matrices, such as Grover and Fourier matrices, for quantum walks. The properties of each directional- and directionally-unbiased design are compared in Table 3.2. In this table, directionally-unbiased three-port and four-port operations are denoted as 3-port and 4-port; Reversible tritters and quarters are denoted as Rev Tritter and Rev Quarter; 3-port Reck, 4-port Reck, and 4-port Clements represent the directional three-port Reck model, the directional four-port Reck model, and the directional four-port Clements model, respectively. We also consider several different conditions for comparing different optical devices: the numbers of beam splitters used to form a device, the coherence length requirement to generate the final unitary matrix, and dense unitary matrix generation. The Grover and the Fourier matrix generation are considered as indicated in the Conditions column in Table 3.2. The number of beam splitters varies depending on the design. Directionally-unbiased linear-optical multiports require the fewest beam splitters among all the devices in the table. A directionally-unbiased N-port requires N beam splitters, while other devices with N input and N output ports would require

N(N + 1) beam splitters. The multiport device demands a long coherence length because different photons traveling paths with different travel lengths need to be coherently summed. In the reversible designs, Reck decomposition, and the Clements decomposition model, the input photon does not need long coherence lengths because the devices consist of balanced interferometers. All the devices listed in the table can realize both the Grover and the Fourier matrices.

Conditions	**3-port**	**4-port**	**Rev T**	**Rev Q**	**3-R**	**4-R**	**4-C**
# of BS	3	4	-	-	12	20	20
Coherence Length	Long	Long	Short	Short	Short	Short	Short
U Generation	✗	✗	✗	✗	✓	✓	✓
Grover Mat	✓	✓	✓	✓	✓	✓	✓
Fourier Mat	✓	✓	✓	✓	✓	✓	✓

Table 3.2: Comparison between reversible and non-reversible designs. In the table, 3-port and 4-port represent directionally-unbiased linear-optical multiports; Rev T and Rev Q represent reversible tritter and reversible quarter; 3-R, 4-R and 4-C represent the three-port and four-port Reck decomposition models and the four-port Clements decomposition model. Short coherence length means there is no coherent addition of paths with significant length difference. U generetion describes the capability of realizing any unitary matrices by decomposition method. Grover Mat and Fourier Mat show the possibility for realizing Grover matrix and Fourier matrix. The check mark implies that the condition can be satisfied while crossed ones cannot satisfy the condition.

3.7 Discussion

The experimentally observed probability distribution for the directionally-unbiased linear-optical multiport illustrates the validity of the original theoretical concept (Simon et al., 2016) offering to construct coherent multi-edged vertices that are suitable for experimentally executing universal quantum walks on arbitrary graphs. The natural reversibility of the photon flow in such multiports offers a dramatic reduction in the amount of required hardware resources when compared with currently exploited systems based on beamsplitter trees. The encounter of such multiport during a quantum walk procedure could be considered as a quantum coin application. The greater number of edges $(N \geqslant 2)$ at every application

of such quantum coin speeds up significantly the coverage of higher dimensions in Hilbert spaces. This opens new possibilities when simulating dynamic Hamiltonians of complex physical systems.

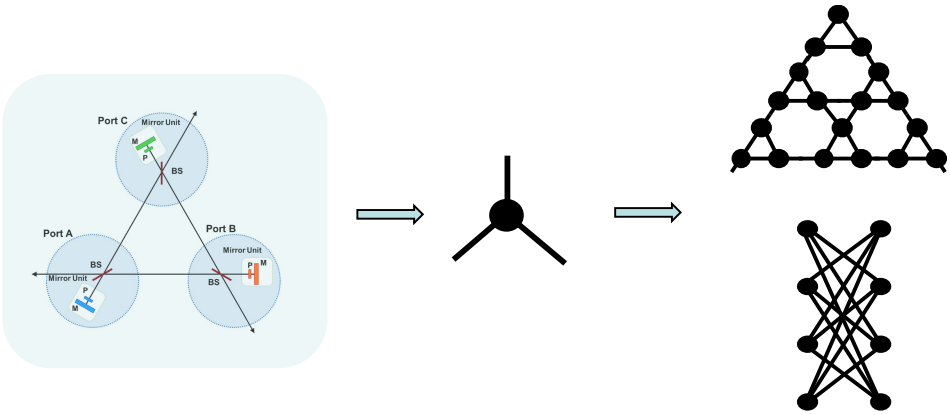

Figure 3·8: Directionally-unbiased linear optical three-edge vertex device demonstrated in this paper could be used for building complex quantum graphs. The efficiency of approaches based on quantum walks on graphs holds the promise of addressing some complex scientific and technical problems more efficiently than conventional numerical computational methods.

This multiport could find a number of applications in the areas of quantum information processing and quantum simulation of dynamic Hamiltonians. The quantum walk on a specially designed network of such three-edge multiports offers configuration flexibility enabling to simulate Hamiltonians of complex polymer chains, energy band structure of semiconductor materials including topological insulators (Simon et al., 2017a). Although an unbiased three-port was examined here, m-ports with $m > 3$ can be constructed in a similar manner. However, it needs to be clarified that if 50:50 beam splitters are used to construct higher dimensional multiports by simply connecting the beam splitters to form a ring structure then the amplitude does not propagate as the number of ports increase. Therefore, it is necessary to introduce some changes in the splitting ratio to scale the device

using our method.

The main result is shown for a totally symmetric three-edge vertex multiport. This multiport design allows to realize a multitude of different unitary transformation matrices (see (Simon et al., 2016)) without ever changing beam splitter splitting ratios. A simple modification in phase shifts at each of the mirror units can modify the transfer matrix amplitudes, allowing output distributions to be controllably tailored for different purposes and opening additional possibilities for simulating physical systems with a range of output probability distributions.

Connecting multiple copies of a three-edge multiports could result in the practical realization of a quantum walk on several complex graphs with different topological properties, using only linear optics. A 1D quantum particle walk on a lattice of such multiport structures corresponding to an SSH-type system has been proposed, offering conditions to demonstrate topological structures and distinguishable winding numbers (Simon et al., 2017b). 1D quantum walk implementation based on beam splitters would scale quadratically due to the feed-forward nature of the setup while the multiport devices scale linearly. Multiport based setup requires as little as two detectors. Feed-forward systems would require at least N detectors; therefore, the multiport setup can reduce both beam splitters and detector requirements. A 2D distribution of three-edge vertices (see Fig. 3·8) has even more interesting applications in the area of designing novel types of topological insulators, quantum walk over fractal states such as the Sierpinski gasket (Crownover, 1995), and serve as natural elements in constructing tensor networks (Werner et al., 2016). The quantum character of signal processing in tensor networks promises significant speed up in the problem solving large systems of differential equations (Bachmayr et al., 2016). It would be practically impossible to execute quantum walks on complex graph structures of reasonable size using conventional binary coins realized with optical beam splitters; directionally unbiased m-ports provide a much more feasible route to implementing such structures while offering

significant savings in resources.

Multi-photon states can also be inserted instead of single-photon inputs. The use of multi-photon input states more easily allows one to fully reconstruct a transfer matrix by explicitly recovering the phase information as well. In addition, such a three-port device with two-photon Bell-state inputs could be used to navigate a group structure when a pair of correlated Bell-states are injected into a non-overlapping set of ports (Simon et al., 2016).

In conclusion, we have demonstrated experimentally the operation of a directionally-unbiased linear-optical three-port unitary device at a particular phase setting of $\frac{\pi}{6}$ by reconstructing a probability distribution of all possible propagation patterns with an interferometric method. The effective operation of the device as a symmetric three-edge vertex suitable for quantum walks on graphs has been demonstrated. This provides one more step towards the intention of using such directionally-unbiased multiports to implement complex quantum walks on graphs and in ultimately demonstrating their practical use in achieving quantum speedup for the solution of specific physical simulations.

Chapter 4

Quantum Walks

4.1 Introduction

Quantum walks are a suitable venue for linear optics based applications to explore. The quantum approach to computing attracts public attention mainly because of its capability to execute some computational tasks faster when compared to classical computational devices (Shor, 1999; Grover, 1996). Several physical platforms exist to realize quantum computation procedures. Linear optics has been one of the candidates because of its robustness against noise and the ease of quantum state manipulation at room temperature. The design of quantum computing gates with single photons has been proposed and is known as the Knill, Laflamme and Milburn (KLM) model (Knill et al., 2001). This design makes use of linear-optical devices such as beam splitters and phase shifters. The quantum gate performance is executed probabilistically by the process of measuring auxiliary photons. While the KLM model has been used for gate-based quantum computation, other quantum-optical approaches to execute computational tasks have been developed. For example, quantum walks (QW) over optical networks of scattering centers have been considered as another promising tool in executing certain computational tasks (Kempe, 2003; Venegas-Andraca, 2012; Aharonov et al., 1993; Portugal, 2013; Childs, 2009). The construction of such optical networks for quantum walks relies on the use of multiple beam splitters and phase shifters connected in a particular spatial graph pattern. A beam splitter is used as an elementary scattering center during the propagation, and many of them must be cascaded by connecting consecutively in order to form an extensive tree-like network (Carolan et al., 2015; Wang et al., 2018).

Quantum mechanical information processing requires unitarity at every operation. The beam splitter in optics implements two-dimensional unitary transformations and can be seen as a probabilistic mixer of two spatial field modes.

The increase in dimensionality enables employing and manipulating more information. This needs to be achieved in a coherent way. Optical networks are constructed to perform this task by constructing higher-dimensional unitary matrices. It is known that higher-dimensional unitary matrices can be decomposed using lower-dimensional unitary matrices. By repeating this procedure, any complex unitary matrix can be eventually decomposed using only two-dimensional ones. The Reck decomposition model (see Sec. 2.5.1) has been introduced to describe this procedure (Reck et al., 1994). A symmetric version of the Reck model is often called the Clements model (see Sec. 2.5.2) (Clements et al., 2016). For example, these two models have been used by researchers in designing and building experimental linear-optical networks for boson sampling purposes (Spring et al., 2013; Broome et al., 2013; Tillmann et al., 2013; Crespi et al., 2013a). During the boson sampling process, photons propagate from one side of a complex nodal structure to the other side of the optical network, thus performing a computational task. Direct implementation of a multimode optical device has been experimentally verified in integrated platforms (Weihs et al., 1996a; Peruzzo et al., 2011; Spagnolo et al., 2013a; Meany et al., 2012). Quantum walks over the network of quantum nodes represent another form of quantum information processing, as an alternative to the quantum gate model. QW can also perform certain computations more efficiently than classical algorithms (Aharonov et al., 1993; Moore and Russell, 2002; Krovi and Brun, 2006; Childs et al., 2002; Childs et al., 2003; Ambainis, 2007; Magniez et al., 2007; Buhrman and Špalek, 2006; Magniez and Nayak, 2007). Quantum walks in 1D and 2D systems have been experimentally demonstrated in optical systems (Bouwmeester et al., 1999a; Knight et al., 2003b; Knight et al., 2003a; Schreiber et al., 2010; Pandey et al., 2011; Zhao et al., 2002; Broome et al., 2010; Goyal et al., 2013;

Zhang et al., 2007; Cardano et al., 2015; Tang et al., 0018; Schreiber et al., 2012).

The traditional quantum walk approach uses a coin operator and a shift operator to execute each elementary step. An alternative description of a quantum walk can be implemented using the scattering quantum walk, also known as the edge walk (Feldman and Hillery, 2004; Feldman and Hillery, 2007), which has been introduced to describe the quantum walk based on scattering at the nodes or vertices of a lattice on which the walk occurs. There is no need for a coin operator in this model. In order to execute some specific type of quantum walk, we first need to identify a network of scattering centers (a graph) on which the walk is performed. Many different special-purpose graphs can be formed using linear-optical devices in order to execute a particular computational procedure. Thanks to the Reck and Clements decomposition models, the majority of experimental demonstrations in this field, even some complex ones, could be realized using multiple directionally-biased two-dimensional optical devices such as beam splitters. However, the execution of such quantum walks calls for a considerable amount of optical devices when the complexity and the required number of steps in the system increase. This is why quantum walks based on the use of directional devices demand a great deal of costly hardware real estate, which limits their scalability in the long run.

A directionally-unbiased linear-optical multiport is a unitary coherent optical quantum information processing device that addresses two issues simultaneously: (i) it executes a higher dimensional unitary scattering process at every node of the network with fewer numbers of two-dimensional units for the device construction, and (ii) it scales down significantly the required amount of hardware resources by offering the possibility of reusing scattering units of the graph again and again. An array of such multiports can then form a graph upon which a photon can execute a quantum walk. In principle, the feature of full reversibility can be realized using special designs by incorporating commonly-used optical elements. This is referred to as “directional” or “directionally-biased” when a photon

propagates only in one direction, meaning the input port and the output ports are never the same. This directionality could be circumvented in optics by placing mirrors so that a photon can leave the input port as well. This chapter is dedicated for reviewing quantum walk systems and is used as a building block for topological photonics and multiphoton quantum walk systems discussed in the next two chapters.

4.2 Discrete-Time Quantum Walks

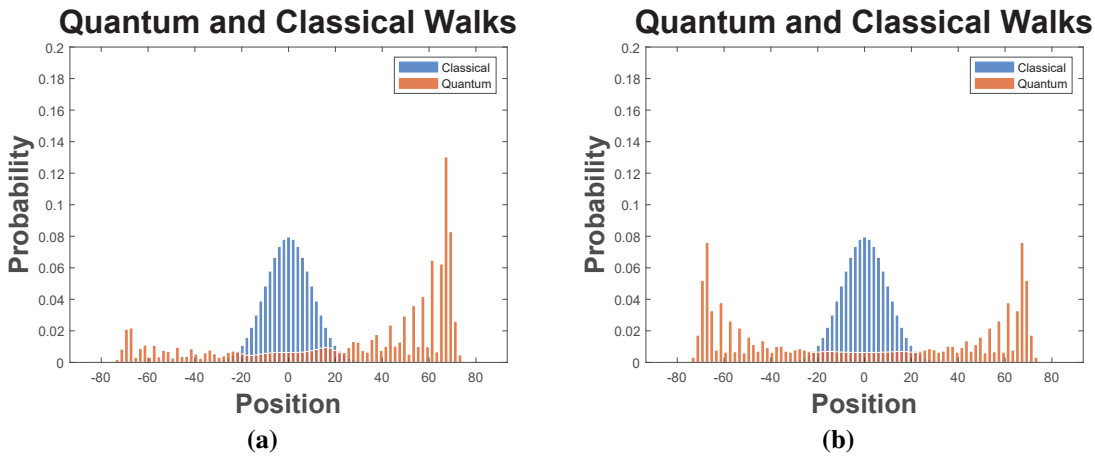

Figure 4·1: Quantum and classical walks with 100 time steps. Quantum walk (orange) spreads faster than the classical case (blue). (a) Skewed quantum walk. The initial internal state is $|0\rangle$. (b) Symmetric quantum walk. The initial internal state is $\frac{1}{\sqrt{2}}(|0\rangle + i|1\rangle)$.

A major motivation for focusing on the directionally-unbiased versions is in their potential for implementing quantum walk applications. Quantum walks can support superposition states and interference in the system where interference is absent in classical random walks. There are two types of quantum walks, discrete-time quantum walks, and continuous-time quantum walks. During the discrete-time quantum walk, the evolution operator is applied in a discrete-time fashion while the operator application timing is irrelevant in the continuous case. We focus on the discrete case in this review. The simplest classical and quantum walk

design would be a walk performed on a line. In the case of a classical random walk on a line with an unbiased two-dimensional coin, a walker can hop one step to the right or to the left with an equal probability depending on the result of a coin-toss event. The walker walks on a line for certain steps, and the probability at a specific position can be obtained by repeating the process. By recording all the probability at each location on the line, a probability distribution associated with that coin is constructed. Classical random walks involve intermediate measurement, meaning the position of the walker is measured right after a coin-toss event. In contrast, the quantum approach to random walks preserves the coherence of all possible paths by not measuring an intermediate state of the walker and, as a consequence, enables the quantum interference of available probability amplitudes. It is known that the probability distribution spreads faster in quantum walks compared to classical random walks. Classical random walks are useful for many randomized algorithm implementations (Motwani and Raghavan, 1996). It is natural to consider that quantum walks could achieve better outcomes than classical random walk-based algorithms, and it is indeed possible to gain algorithmic speedup using the fact that quantum walks can spread faster than classical random walks. Several different algorithms have been developed through quantum walks, and some are faster than classical algorithms. Hitting time, graph traversal speed from a point to another point in a graph, on a hypercube (Moore and Russell, 2002; Krovi and Brun, 2006), and a glued tree are known to be exponentially faster in the quantum case (Childs et al., 2002; Childs et al., 2003). Element distinctness (Ambainis, 2007), triangle finding (Magniez et al., 2007), matrix product verification (Buhrman and Špalek, 2006), and group commutativity testing (Magniez and Nayak, 2007) has been also investigated. Flexible graph construction is necessary to perform quantum walk-based algorithms. Any graphs consist of vertices and edges, and these need to be prepared in an experimentally realizable way. This task can be achieved through linear-optical devices, which have several input and output ports as discussed in previous sections. An experimental

quantum walk implementation has been demonstrated in optical systems using optical cavities (Bouwmeester et al., 1999a; Knight et al., 2003b), optical rings (Knight et al., 2003a), time-bins (Schreiber et al., 2010), Michelson interferometers (Pandey et al., 2011), optical network (Zhao et al., 2002), beam displacers (Broome et al., 2010), orbital angular momentum manipulation (Goyal et al., 2013; Zhang et al., 2007; Cardano et al., 2015), and optical refraction (Francisco et al., 2006). The majority of these implementations are based on directional-optical devices; therefore, their implementation costs would rapidly increase as the dimensionality of the quantum walk system becomes higher. This applies to spatially-multiplexed quantum walk systems as they need to use beam splitters in a feed-forward manner. Time-multiplexed quantum walks are also commonly used since they can be compact. Still, it would be challenging to perform node-by-node amplitude tuning. Integrated waveguide-based systems can be made directionally-unbiased and have been experimentally demonstrated (Peruzzo et al., 2010; Tang et al., 0018; Tang et al., 2018). Directionally-unbiased linear-optical multiport-based quantum walk configurations, which can realize amplitude tunability while offering an implementation resource reduction, will be introduced in the following several subsections.

4.2.1 Coin Walk: Quantum Walk on Vertices

The traditional quantum walk is illustrated using a position Hilbert space H_P and a "coin" Hilbert space H_C. A quantum walker's position is described by the amplitudes in a position space spanned by $\{|m\rangle, m \in \mathbb{Z}\}$, and a coin space is spanned by a two-dimensional computational basis $\{|R\rangle \equiv (1,0)^T, |L\rangle \equiv (0,1)^T\}$. The Hilbert space of the system is given by $H = H_P \otimes H_C$. We define a coin operator $\hat{C}$ and a shift operator $\hat{S}$ acting on each Hilbert space. The shift operator translates a walker's position from $|m\rangle$ to $|m-1\rangle$ or $|m+1\rangle$ depending on the result of the coin operation.

$$\hat{S}|m\rangle|R\rangle = |m+1\rangle|R\rangle \text{ and } \hat{S}|m\rangle|L\rangle = |m-1\rangle|L\rangle. \tag{4.1}$$

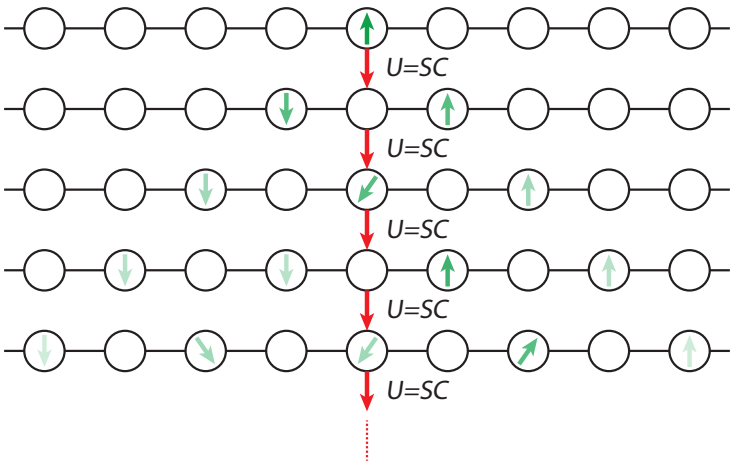

Figure 4·2: Coin based quantum walk. The initinal state is rotated by the coin operator C and depending on the rotated state is translated by the shift operator S. The single step of the quantum walk would be described bu $U = SC$. The color opacity of the green arrows corresponds to the probability.

We can deduce a linear operator $\hat{S}$.

$$\hat{S} = \sum_{n=-\infty}^{\infty} |m+1\rangle \langle m| \otimes |R\rangle \langle R| + \sum_{n=-\infty}^{\infty} |m-1\rangle \langle m| \otimes |L\rangle \langle L| . \tag{4.2}$$

The walker's direction of the walk is decided by the result of the coin operator. The walk consists of applying, at each step, the coin operator, then the shift operator. The combined operation is given by:

$$\hat{V} = \hat{S} \cdot (\hat{I} \otimes \hat{C}). \tag{4.3}$$

This $\hat{V}$ is applied on an initial state multiple times to perform walks with multiple steps.

$$|\psi(t = N)\rangle = \hat{V}^N |\psi(t = 0)\rangle . \tag{4.4}$$

The Hadamard coin operator $\hat{H}_2$ can be used to demonstrate the quantum walk. The coin operator $\hat{C}$ in Eq. (4.3) is substituted by $\hat{H}_2$.

$$\hat{H}_2 = \frac{1}{\sqrt{2}} \begin{pmatrix} 1 & 1 \\ 1 & -1 \end{pmatrix} . \tag{4.5}$$

One cycle of the quantum walk is completed by applying $\hat{H} \otimes \hat{I}$ followed by $\hat{S}$. This process is performed multiple times without making intermediate measurements. Final measurements are made after a certain number of time steps. The probability distribution generated using a quantum walk behaves differently than a classical random walk. The standard deviation of the classical random walk on a line with N step is known to have a size of $\sqrt{N}$ (Kempe, 2003); on the other hand, a quantum walk on a line has a standard deviation of the order of N. This indicates that the quantum walk spreads faster than the classical random walk and can result in large speed increases in searching applications.

4.2.2 Scattering Quantum Walk: Quantum Walk on Edges

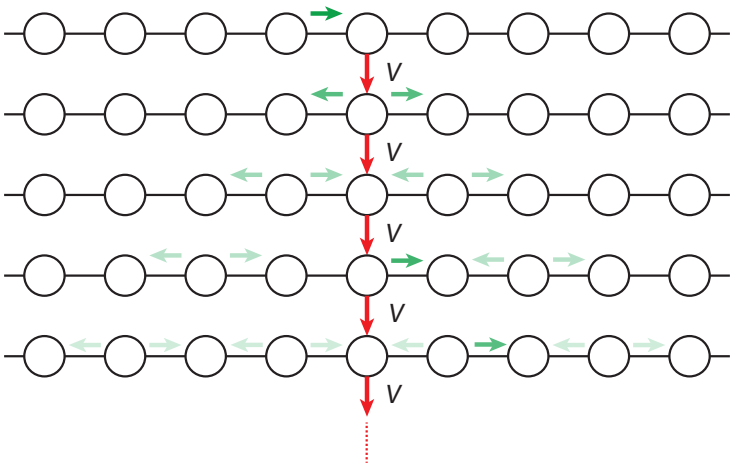

Figure 4·3: Quantum walk on edges. The initial state is in one of the edges propagating to the right. The amplitude gets transmitted and reflected by some amount defined by an operator V. We would observe some amplitude cancellation. The color opacity of the green arrows corresponds to the probability.

A different picture of the quantum walk is provided by the scattering model introduced (Feldman and Hillery, 2004; Feldman and Hillery, 2007). This discrete-time scattering-based quantum walk is also called an edge walk. Unlike the coin model, the interference occurs on edges instead of performing the walk only on vertices. Each vertex works as a

scattering center in this model. An input photon amplitude and phase will be controlled by a transmission and reflection coefficient at the scattering center. This model starts with a photon in a state $|m-1,m\rangle$, representing a photon propagating from a vertex location $m-1$ to m, hence describing a state on an edge.

In this scattering model, a Michelson interferometer can serve as a vertex with two edges. One-step propagation starting at a specific edge is given by:

$$\begin{aligned} \hat{U}_{Michelson}\,|m-1,m\rangle &\rightarrow \frac{1}{\sqrt{2}}(|m,m+1\rangle + i\,|m,m-1\rangle). \\ \hat{U}_{Michelson}\,|m+1,m\rangle &\rightarrow \frac{1}{\sqrt{2}}(|m,m-1\rangle + i\,|m,m+1\rangle). \end{aligned} \tag{4.6}$$

We will introduce a simplified description for a single scattering center, but we present the full description first. The unitary transformation represented by the Michelson interferometer in Eq. (4.6) and illustrated in Fig. 4·4b can be rewritten using the matrix below:

$$U_{Full} = \begin{pmatrix} A_R \rightarrow A_R & A_L \rightarrow A_R & B_R \rightarrow A_R & B_L \rightarrow A_R \\ A_R \rightarrow A_L & A_L \rightarrow A_L & B_R \rightarrow A_L & B_L \rightarrow A_L \\ A_R \rightarrow B_R & A_L \rightarrow B_R & B_R \rightarrow B_R & B_L \rightarrow B_R \\ A_R \rightarrow B_L & A_L \rightarrow B_L & B_R \rightarrow B_L & B_L \rightarrow B_L \end{pmatrix} = \frac{1}{\sqrt{2}} \begin{pmatrix} 0 & i & 1 & 0 \\ i & 0 & 0 & 1 \\ 1 & 0 & 0 & i \\ 0 & 1 & i & 0 \end{pmatrix}. \tag{4.7}$$

$$\begin{aligned} \hat{U}_{Full}\,|A_R\rangle &\rightarrow \frac{1}{\sqrt{2}}(|B_R\rangle + i\,|A_L\rangle), \\ \hat{U}_{Full}\,|B_L\rangle &\rightarrow \frac{1}{\sqrt{2}}(|A_L\rangle + i\,|B_R\rangle). \end{aligned} \tag{4.8}$$

$|A_R\rangle$, $|A_L\rangle$, $|B_R\rangle$, and $|B_L\rangle$ correspond to $|m-1,m\rangle$, $|m,m-1\rangle$, $|m,m+1\rangle$, and $|m+1,m\rangle$, respectively. The propagation direction needs to be distinguished when multiple scattering centers are connected, but a simplified version can be used for a single scattering center. We will use the simplified matrix for a single scattering element in the upcoming sections so that we can directly make a comparison to the coin operators:

$$\hat{U}_{Simplified} = \begin{pmatrix} A \rightarrow A & B \rightarrow A \\ A \rightarrow B & B \rightarrow B \end{pmatrix} = \frac{1}{\sqrt{2}} \begin{pmatrix} i & 1 \\ 1 & i \end{pmatrix} \tag{4.9}$$

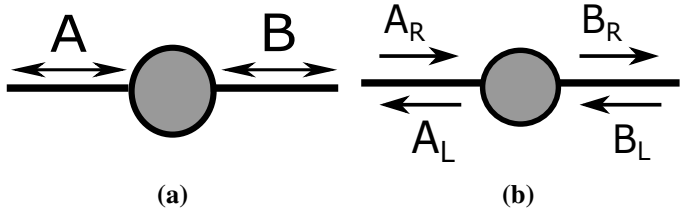

Figure 4·4: (**a**) Directionally-insensitive description for a scattering center. A photon can enter port A and then leave either port A or B. (**b**) Directionally-sensitive description for a scattering center. If the photon is initially in the state A_R, then the photon will have an amplitude in the A_L direction and the B_R direction. Photon in states A_R and A_L do not interact, so they need to be distinguished when a graph is formed based on scattering centers.

By repeating this unitary matrix transformation process from an initial state, a walk can be implemented on a line. This scattering model is unitarily equivalent to the coin walk (Venancio et al., 2013; Hillery et al., 2003). To see the unitary equivalence between the two models, we define a unitary operator $\hat{E}$.

$$\begin{aligned} \hat{E}\,|m-1,m\rangle &= |m\rangle \otimes |R\rangle\,, \\ \hat{E}\,|m+1,m\rangle &= |m\rangle \otimes |L\rangle\,, \end{aligned} \tag{4.10}$$

where $|R\rangle$ and $|L\rangle$ are defined in the coin model section. Consider a state evolution by operators $\hat{E}\hat{U}$ with an initial condition $|m-1,m\rangle$.

$$\begin{aligned} \hat{U}\,|m-1,m\rangle &= \frac{1}{\sqrt{2}}(|m,m+1\rangle + i\,|m,m-1\rangle), \\ \hat{E}\hat{U}\,|m-1,m\rangle &= \frac{1}{\sqrt{2}}(|m+1\rangle \otimes |R\rangle + i\,|m-1\rangle \otimes |L\rangle). \end{aligned} \tag{4.11}$$

$$\begin{aligned} \hat{V}\hat{E}\,|m-1,m\rangle = \hat{V}\,|m\rangle \otimes |R\rangle &= \hat{S}\,|m\rangle \otimes \frac{1}{\sqrt{2}}(|R\rangle + i\,|L\rangle) \\ &= \frac{1}{\sqrt{2}}(|m+1\rangle \otimes |R\rangle + i\,|m-1\rangle \otimes |L\rangle). \end{aligned} \tag{4.12}$$

The former represents the edge walk, and the latter represents the coin walk. The outcomes are the same when the evolution operators $\hat{U}$ and $\hat{V}$ are multiplied by the operator $\hat{E}$; therefore, these two formalisms are unitarily equivalent. This unitary equivalence $\hat{E}\hat{U} = \hat{V}\hat{E}$ can be also seen as $\hat{U} = \hat{E}^{\dagger}\hat{V}\hat{E}$. $\hat{U}^n = \hat{E}^{\dagger}\hat{V}^n\hat{E}$ because of unitarity of the operator $\hat{E}$ where n is an integer. For example, the operators below would satisfy the equivalence between the two works.

$$E = \sum_m |m-1\rangle \langle m| \otimes |R\rangle \langle R| + |m\rangle \langle m| \otimes |L\rangle \langle L| \tag{4.13}$$

$$E^{-1} = \sum_m |m+1\rangle \langle m| \otimes |R\rangle \langle R| + |m\rangle \langle m| \otimes |L\rangle \langle L| \tag{4.14}$$

This result can be extended to higher dimensional walks. We can find the same equivalence for an initial state $|m+1, m\rangle$.

4.2.3 Higher Dimensional Coin Operators and Scattering Vertices

Quantum walks can be extended to higher dimensions by changing the dimension of the operators in the system and attaching additional edges to each vertex. It is possible to introduce scattering centers with different scattering amplitude ratios between output modes using directionally-unbiased devices. We will introduce several different coin operators and corresponding scattering centers in this section. The relationship between the coin model and the scattering model is deduced using an additional unitary operator as discussed in the previous subsection. There are several quantum coin operators with specific characteristics. The Hadamard coin, an unbiased coin, is one example.

The four-dimensional real-valued Hadamard coin H_4 is given as an example. This matrix

is obtained by taking the tensor product of two by two real Hadamard matrices H_2.

$$H_4 = H_2 \otimes H_2 = \frac{1}{2}\begin{pmatrix} 1 & 1 & 1 & 1 \\ 1 & -1 & 1 & -1 \\ 1 & 1 & -1 & -1 \\ 1 & -1 & -1 & 1 \end{pmatrix}. \tag{4.15}$$

In addition to the Hadamard coin, there are two other major specific coins used in quantum information processing. The first coin is motivated by Grover's search algorithm (Grover, 1996).

$$C_d = \begin{pmatrix} \frac{2}{d}-1 & \frac{2}{d} & \cdots & \frac{2}{d} \\ \frac{2}{d} & \frac{2}{d}-1 & \cdots & \frac{2}{d} \\ \vdots & \vdots & \ddots & \vdots \\ \frac{2}{d} & \frac{2}{d} & \cdots & \frac{2}{d}-1 \end{pmatrix}, \tag{4.16}$$

where d is the size of the matrix.

Matrices for $d = 3$ and 4 are given.

$$C_3 = \frac{1}{3}\begin{pmatrix} -1 & 2 & 2 \\ 2 & -1 & 2 \\ 2 & 2 & -1 \end{pmatrix} \quad \text{and} \quad C_4 = \frac{1}{2}\begin{pmatrix} -1 & 1 & 1 & 1 \\ 1 & -1 & 1 & 1 \\ 1 & 1 & -1 & 1 \\ 1 & 1 & 1 & -1 \end{pmatrix}. \tag{4.17}$$

This coin is biased in amplitudes (except for d = 4), yet symmetric under permutations of matrix labels. Another coin is a discrete Fourier transform (DFT) coin; this coin is unbiased; however, it is not symmetric under permutations. The Fourier transform matrix is given by:

$$U_{Fourier} = \frac{1}{\sqrt{d}}\begin{pmatrix} 1 & 1 & 1 & \cdots & 1 \\ 1 & \omega & \omega^2 & \cdots & \omega^{d-1} \\ 1 & \omega^2 & \omega^4 & \cdots & \omega^{2(d-1)} \\ \vdots & \vdots & \vdots & \ddots & \vdots \\ 1 & \omega^{(d-1)} & \omega^{2(d-1)} & \cdots & \omega^{(d-1)(d-1)} \end{pmatrix}, \tag{4.18}$$

where $\omega = e^{-\frac{2\pi i}{d}}$.

Three-dimensional and four-dimensional Fourier coins are given by:

$$U_{Fourier} = \frac{1}{\sqrt{3}} \begin{pmatrix} 1 & 1 & 1 \\ 1 & \omega_3 & \omega_3^2 \\ 1 & \omega_3^2 & \omega_3 \end{pmatrix}, \tag{4.19}$$

where $\omega_3 = e^{-\frac{2\pi i}{3}}$.

$$U_{Fourier} = \frac{1}{2} \begin{pmatrix} 1 & 1 & 1 & 1 \\ 1 & \omega_4 & \omega_4^2 & \omega_4^3 \\ 1 & \omega_4^2 & \omega_4^4 & \omega_4^6 \\ 1 & \omega_4^3 & \omega_4^6 & \omega_4^9 \end{pmatrix} = \frac{1}{2} \begin{pmatrix} 1 & 1 & 1 & 1 \\ 1 & i & 1 & -i \\ 1 & -1 & 1 & -1 \\ 1 & -i & -1 & i \end{pmatrix}, \tag{4.20}$$

where $\omega_4 = e^{-\frac{2\pi i}{4}}$.

4.2.4 Equivalence between Higher Dimensional Coin Walk and Scattering Quantum Walk

The coin walk and the scattering walk were introduced in the previous subsections, as well as higher-dimensional coin operators. It is possible to give a unitary equivalence relation between the two walks in higher dimensions as well. Consider a quantum walk on a 2D rectangular lattice. The center of the grid is given by coordinate (m,n). A photon on one of the edges around that grid is defined as $|m,m,n-1,n\rangle$. This state is read as a photon propagation from a vertex location $(m,n-1)$ to (m,n). The unitary operator for one

propagation step of an edge is defined as:

$$\begin{aligned}
\hat{U}\,|m-1,m,n,n\rangle \rightarrow \quad & \tfrac{1}{2}(|m,m-1,n,n\rangle + |m,m,n,n+1\rangle \\
& - |m,m+1,n,n\rangle + |m,m,n,n-1\rangle), \\
\hat{U}\,|m,m,n+1,n\rangle \rightarrow \quad & \tfrac{1}{2}(|m,m-1,n,n\rangle + |m,m,n,n+1\rangle \\
& + |m,m+1,n,n\rangle - |m,m,n,n-1\rangle), \\
\hat{U}\,|m+1,m,n,n\rangle \rightarrow \quad & \tfrac{1}{2}(-|m,m-1,n,n\rangle + |m,m,n,n+1\rangle \\
& + |m,m+1,n,n\rangle + |m,m,n,n-1\rangle), \\
\hat{U}\,|m,m,n-1,n\rangle \rightarrow \quad & \tfrac{1}{2}(|m,m-1,n,n\rangle - |m,m,n,n+1\rangle \\
& + |m,m+1,n,n\rangle + |m,m,n,n-1\rangle).
\end{aligned} \tag{4.21}$$

The corresponding coin operator of the coin walk is given by:

$$\hat{C} = \frac{1}{2}\begin{pmatrix} -1 & 1 & 1 & 1 \\ 1 & -1 & 1 & 1 \\ 1 & 1 & -1 & 1 \\ 1 & 1 & 1 & -1 \end{pmatrix}. \tag{4.22}$$

The matrix is essentially the Grover matrix.

The operator transforms an initial coin state into a superposition state:

$$\hat{C}\,|L\rangle = \frac{1}{2}(-|L\rangle + |U\rangle + |R\rangle + |D\rangle), \tag{4.23}$$

where $|L\rangle = (1,0,0,0)^T, |U\rangle = (0,1,0,0)^T, |R\rangle = (0,0,1,0)^T, |D\rangle = (0,0,0,1)^T$. A new shift operator is defined as follows:

$$\begin{aligned}
\hat{S} = \sum_m \sum_n & (|m,n+1\rangle\langle m,n| \otimes |U\rangle\langle U| + |m,n-1\rangle\langle m,n| \otimes |D\rangle\langle D| \\
& + |m+1,n\rangle\langle m,n| \otimes |R\rangle\langle R| + |m-1,n\rangle\langle m,n| \otimes |L\rangle\langle L|).
\end{aligned} \tag{4.24}$$

One step of the coin walk is given by:

$$\hat{V} = \hat{S}(\hat{I} \otimes \hat{C}). \tag{4.25}$$

We wish to find equivalence between the edge walk and the coin walk by finding a unitary operator $\hat{E}$. Define an operator $\hat{E}$ transforming edge states into vertex states.

$$\begin{aligned} \hat{E}\,|m-1,m,n,n\rangle &= |m,n\rangle \otimes |R\rangle \\ \hat{E}\,|m,m,n+1,n\rangle &= |m,n\rangle \otimes |D\rangle \\ \hat{E}\,|m+1,m,n,n\rangle &= |m,n\rangle \otimes |L\rangle \\ \hat{E}\,|m,m,n-1,n\rangle &= |m,n\rangle \otimes |U\rangle\,. \end{aligned} \tag{4.26}$$

Consider two cases for the coin-based walk and edge walk starting with an initial state $|m,m,n-1,n\rangle$.

Unitary transformation of the coin-based walk:

$$\hat{E}\,|m,m,n-1,n\rangle = |m,n\rangle \otimes |U\rangle\,. \tag{4.27}$$

$$\begin{aligned} \hat{V}\hat{E}\,|m,m,n-1,n\rangle &= S\,|m,n\rangle \otimes (\tfrac{1}{2}(|L\rangle - |U\rangle + |R\rangle + |D\rangle)) \\ &= S\tfrac{1}{2}(|m,n\rangle \otimes |L\rangle - |m,n\rangle \otimes |U\rangle + |m,n\rangle \otimes |R\rangle + |m,n\rangle \otimes |D\rangle) \\ &= \tfrac{1}{2}(|m-1,n\rangle \otimes |L\rangle - |m,n+1\rangle \otimes |U\rangle \\ &\quad + |m+1,n\rangle \otimes |R\rangle + |m,n-1\rangle \otimes |D\rangle). \end{aligned} \tag{4.28}$$

Unitary transformation of the edge-based walk:

$$\begin{aligned} \hat{U}\,|m,m,n-1,n\rangle &= \frac{1}{2}(|m,m-1,n,n\rangle - |m,m,n,n+1\rangle \\ &+ |m,m+1,n,n\rangle + |m,m,n,n-1\rangle). \end{aligned} \tag{4.29}$$

$$\begin{aligned}\hat{E}\hat{U}\,|m,m,n-1,n\rangle &= \frac{1}{2}(|m-1,n\rangle\otimes|L\rangle - |m,n+1\rangle\otimes|U\rangle \\ &+ |m+1,n\rangle\otimes|R\rangle + |m,n-1\rangle\otimes|D\rangle). \qquad (4.30)\end{aligned}$$

$\hat{V}\hat{E}$ and $\hat{E}\hat{U}$ both transform the initial state into the same state. Therefore, the outcomes are equivalent, and the coin walk and the scattering walk are unitarily equivalent. We went through a specific equivalence, which is the quantum walk generalized equivalence between two models, as found elsewhere (Venancio et al., 2013; Feldman and Hillery, 2004).

4.2.5 Examples of Multi-Dimensional Quantum Walks on Graphs

The two types of quantum walks, the coin quantum walk, and the scattering (edge) quantum walk, are both performed on graphs. Graphs with nodes implemented by higher dimensional coins are applicable to algorithm development. For example, the Grover search algorithm, when implemented via quantum walks on certain graphs with a superposition initial state, demonstrates significant speedup over classical algorithms. Many quantum walk applications are based on undirected graphs, meaning a walker can travel forward and backward in the system. Directionally-unbiased linear-optical devices possess reversibility and therefore can implement such undirected graphs. It has been established that a spatial search performed on a 2D lattice is faster than similar classical algorithms (Benioff, 2000; Aaronson and Ambainis, 2003; Childs and Goldstone, 2004; Tulsi, 2008; Abal et al., 2010; Abal et al., 2012). To observe the spatial search on a 2D lattice, the scattering centers have transmission and reflection coefficients equal to the Grover coin setting. One node in a graph is "marked" by introducing a different matrix on one specific scattering center in the lattice. Localization occurs on edges around the marked scattering center when the superposition state is sent in the system as an initial state. The graph geometry can be configured using directionally-unbiased devices. The rectangular lattice illustrated in Fig. 4·5a would require four-port

devices. Similarly, the hexagonal lattice illustrated in Fig. 4·5b would require three-port devices. These optical quantum walk implementations through these optical devices are advantageous because of their amplitude tunability. The graphs can be implemented with the same Grover coin matrix setting throughout the graph vertices initially, then a marked coin can be introduced by tuning one of the vertices into a different coin. A quantum walk search can find the marked point faster than any classical search algorithms.

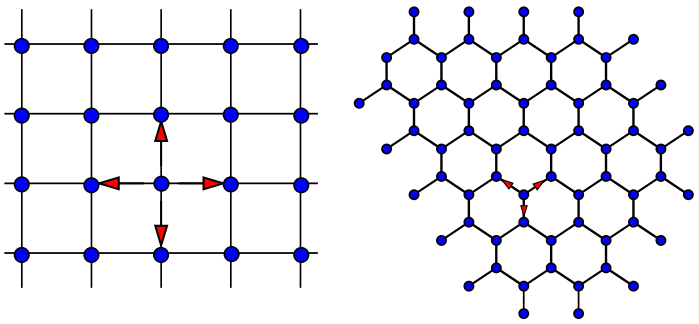

Figure 4·5: (**a**) Rectangular lattice. This structure has four edges for every vertex. (**b**) Hexagonal lattice. This structure has three edges for every vertex.

Other graph structures can be considered using directionally-unbiased devices. Quantum walks on a glued tree have been investigated theoretically and experimentally (Kempe, 2005; Tang et al., 0018). Hitting time, the time required to reach one point to another point on a graph is commonly used to evaluate propagation speed on a specific graph. A quantum walk on a glued tree with three nodes gives exponential speedup when the three-dimensional Grover coin is used at the nodes (Tregenna et al., 2003). We can form hypercubes using unbiased multiports, and it has been shown that the quantum walk hitting time is shorter than the classical walk case (Krovi and Brun, 2006). A walker starts on the left side of the graph, and the walker tries to reach the other end in a short amount of time. As indicated in Fig. 4·6a, the randomly-connected middle part in the glued tree complicates the pathfinding procedure to reach the other end. The speedup applies in the case of the hypercube as

well. A four-dimensional hypercube is illustrated in Fig. 4·6b as an example. Classical algorithms cannot perform this search efficiently. On the other hand, quantum walks can perform exponentially faster than any classical algorithms to find the other end of the path (Shi et al., 2020).

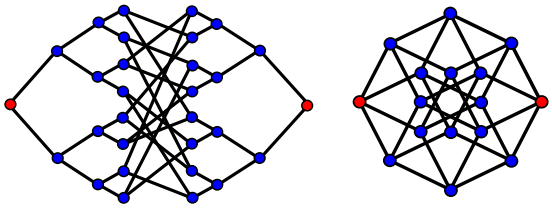

Figure 4·6: (**a**) Glued tree. Two trees are glued in a random manner in the middle part of the graph. A photon's hitting time from one red circle to the other red circle is shorter than the classical walk on this graph. (**b**) Four-dimensional hypercube. Every vertex has four edges. A photon's hitting time from one red circle to the other red circle is shorter than the classical walk on this graph.

4.3 Summary

We reviewed discrete-time quantum walk systems and the use of directionally-unbiased linear-optical designs in quantum walk applications. This directionally-unbiased system allowed us to generate reversible graphs with vertices having multiple edges. This flexibility in graph generation can be useful in quantum walk-based algorithmic speedup as briefly mentioned in the introduction part of Sec. 4.2.

Previously introduced directionally-unbiased designs (Simon et al., 2016; Osawa et al., 2018), reversible optical tritter and quarter, can work as scattering centers having three and four edges for quantum walk applications. These designs are advantageous because of the implementation cost reduction by removing directional bias in the system. We focused on Grover and Fourier coin implementations, which are important matrices in quantum

information processing. Grover and Fourier matrices can be realized when all the phases are at proper settings. Any unitary matrices can be realized using directional devices; however, this is not the case for the directionally-unbiased design. Directionally-unbiased designs cannot realize non-self-transpose unitary matrices. We have focused on quantum walk and search applications in this chapter. This chapter is a building block for the next two chapters by reviewing the key components in quantum walk systems.

Chapter 5

Topology Assisted Quantum Information Processing

5.1 Introduction

States with integer-valued topological invariants, such as winding and Chern numbers, exhibit a variety of physically interesting effects in solid-state systems (Hasan and Kane, 2010; Kitagawa, 2012; Asbóth et al., 2016; Bernevig and Hughes, 2013; Stanescu, 2016), including integer and fractional quantum Hall effects (Thouless, 1983; Laughlin, 1983; Tsui et al., 1982; Laughlin, 1981; Klitzing et al., 1980). Such topological invariants can be simulated in a simple model often known as the Su-Schreiffer-Heeger (SSH) model (Su et al., 1979; Su et al., 1980). Originally, the SSH model describes the behavior of an electron in polymers by introducing staggered hopping amplitudes between lattice sites. The SSH system has two parameters and depending on the relationship between the two parameters, the system can be classified based on some topologically distinct properties. To show the topological distinction, discrete symmetries are useful when combined with band structures of the system. There are three main symmetries used for topological phase classification such as time-reversal, particle-hole, and chiral symmetries in a Hermitian system (Kitaev, 2009).

When band gapped systems with different values of topological invariants are brought into contact, states arise that are highly localized at the boundaries. These edge or boundary states have unusual properties; for example, in two dimensional materials they lead to

unidirectional conduction at the edges, while the interior bulk remains insulating. Because of the inability to continuously interpolate between discrete values of the topological invariant, these surface states are protected from scattering and are highly robust against degradation. This makes them prime candidates for use in error-protected quantum information processing. Optical states with similar topological properties can be produced by means of photonic quantum walks in linear-optical systems(Kitagawa et al., 2012; Kitagawa et al., 2010b; Kitagawa et al., 2010a; Simon, 2018; Bouwmeester et al., 1999a; Zhang et al., 2007; Ribeiro et al., 2008; Perets et al., 2008; Schreiber et al., 2010; Broome et al., 2010; Lu et al., 2014; Lu et al., 2016; Cardano et al., 2017). Photonic walks have demonstrated topological protection of polarization entanglement (Moulieras et al., 2013) and of path entanglement in photonic crystals (Rechtsman et al., 2016).

In a periodically driven system, we are interested in a time periodic Hamiltonian $H(t) = H(t+T)$ where T being the period of the drive. We can establish Floquet formalism through the Schrodinger equation (Holthaus, 2015).

$$i\hbar\frac{d}{dt}\left|\psi(t)\right\rangle = H(t)\left|\psi(t)\right\rangle. \tag{5.1}$$

The solution to this equation is given by

$$U(t,t_0) = \mathbb{T}exp\left[-i\int_{t_0}^{t} H(t^{'})dt^{'}\right], \tag{5.2}$$

where $\mathbb{T}$ is the time-ordering operator. This is in general not an easy task to evaluate without the temporal periodicity of H. In a quantum walk system, the time evolution of the state can be written as $\left|\psi(t+1)\right\rangle = U\left|t\right\rangle$ for some unitary operator U. We can associate the quantum walk unitary transformation such as the simple Hadamard walk and the split-step quantum walk to the periodically driven Hamiltonians through Floquet formalism. With the temporal quasienergy, we can define an effective Hamiltonian $H_{eff} \propto ilnU(t,t_0)$. Because of this relationship, we can study the effective band structure through unitary operators.

Optical systems are useful laboratories to study topologically-nontrivial states, due to the high level of control: system properties can be varied over a wide range of parameters, in ways not easy to replicate in condensed matter systems. In the quest to carry out practical quantum information processing tasks, it is of great interest to examine more closely the types of topologically-protected states that can be optically engineered. Those that are also entangled are of particular interest for quantum information applications. The goal is to entangle states that are associated with distinct topological sectors, and to do so in a way that allows this entangled topology to be readily available for information processing. Specifically, linear optics will be used to produce: (i) entangled topologically-protected boundary states, (ii) winding-number-entangled bulk states, and (iii) an entangled pair of error-protected memory registers. To create the states, a source of initial polarization entangled light is necessary, specifically type-II spontaneous parametric down conversion (SPDC) in a $\chi(2)$ nonlinear crystal. Taking this initial state as given, all further processing requires only linear optical elements. Topological invariants characterize global properties of systems and cannot be easily distinguished by localized measurements. This difficulty in measurement limits their use in many applications. That problem is solved here by linking topology to a more easily-measured variable, polarization. Polarizations and winding numbers will be tightly correlated (and in fact, jointly entangled with each other), but will serve distinct purposes: winding number provides stability against perturbations, while polarization allows easy access and measurement. We confine ourselves to one-dimensional systems.

It is shown that arrays of directionally-unbiased linear-optical multiports can produce entangled pairs of bulk states associated with an effective Hamiltonians of different winding number through a quantum walk approach. A variation of the same idea then allows single qubits or entangled qubit pairs to be stored in a linear optical network as winding numbers. Topological protection of boundary states is well-known, but less widely recognized is the

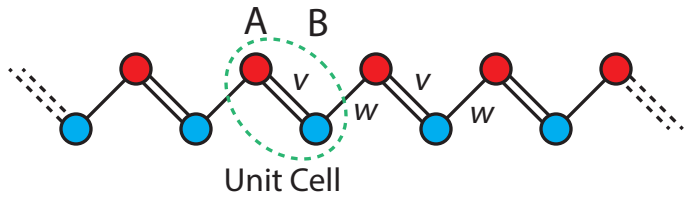

Figure 5·1: The SSH model. A unit cell consists of sublattice A and B. The intracell hopping is given by v and the intercell hopping is given by w.

fact that bulk wavefunctions also have a degree of resistance to changes in winding numbers (Simon et al., 2018b). This transition suppression of bulk wavefunction effect is used to reduce polarization-flip errors of qubits stored in the optical register, greatly reducing the need for additional error correction. It needs to be noted that some amount of transmission from a topological bulk to a trivial bulk is allowed due to the fact that the suppression amount relies on both amplitude hopping parameters and a topological distinction. We start with reviewing the SSH Hamiltonian model to understand topological properties of the bulk structure.

5.2 The SSH model

The SSH model is a simple toy model yet has some rich topological features (Su et al., 1979; Su et al., 1980). The system consists of two repeating sublattices A, B forming a unit cell as indicated in Fig. 5·1, and the hopping amplitude between the sublattices are the controllable parameters of the system. Having a unit cell with two sublattices allows introducing internal degrees of freedom, which is useful to evaluate SSH Hamiltonian by evaluating only internal degrees of freedom.

We can write its Hamiltonian by

$$\begin{aligned} H_{SSH} &= v\sum_{m}^{N}(|m,B\rangle\langle m,A| + |m,A\rangle\langle m,B|) \\ &+ w\sum_{m}^{N-1}(|m+1,A\rangle\langle m,B| + |m,B\rangle\langle m+1,A|), \end{aligned} \tag{5.3}$$

where $v, w \geq 0$ and N is the total number of unit cells. The chain has boundaries at the two ends of the chain and bulk portion of the chain. The presence of the boundary should not affect the bulk part when the chain is long enough. To evaluate the bulk part of the physics, we connect the ends of boundaries to form a loop so that we can apply periodic boundary conditions. By applying Fourier transform $|k\rangle = \frac{1}{\sqrt{N}} \sum_{m=1}^{N} e^{imk} |m\rangle$ to the unit cell index, we can obtain bulk momentum-space Hamiltonian of internal degrees of freedom (Asbóth et al., 2016).

$$H(k) = \begin{pmatrix} 0 & v + we^{-ik} \\ v + we^{ik} & 0 \end{pmatrix}, \tag{5.4}$$

$$H(k) \begin{pmatrix} a(k) \\ b(k) \end{pmatrix} = E(k) \begin{pmatrix} a(k) \\ b(k) \end{pmatrix}. \tag{5.5}$$

From the equation above, we can examine the dispersion relation of the Hamiltonian by varying k.

$$E = \pm \sqrt{v^2 + w^2 + 2vwcos(k)}. \tag{5.6}$$

The band gap closes at v = w.

The SSH model has a $\mathbb{Z}_2$ invariant obtained from the Berry phase in 1D model. The Berry phase for sweeping Brillouin zone in one-dimensional systems is called the Zak phase (Zak, 1989). In general, the Zak phase is not quantized, however the quantization occurs under the existence of chiral symmetry (Ryu et al., 2010). The Zak phase and the winding number can be used interchangeably since they both calculate the Berry curvature of the same system.

Winding numbers are defined as

$$\nu = \frac{1}{2\pi i} \int_0^{2\pi} \langle \psi | \frac{d}{dk} | \psi \rangle \, dk. \tag{5.7}$$

We can obtain bulk winding number of the SSH model from

$$|\psi^{\pm}\rangle = \begin{pmatrix} \pm e^{-i\phi(k)} \\ 1 \end{pmatrix}, \text{where } \phi(k) = tan^{-1}\left(\frac{wsin(k)}{v+wcos(k)}\right). \tag{5.8}$$

$$\nu = \begin{cases} 1 & v < w \\ 0 & v > w \\ Undefined & v = w \end{cases} \tag{5.9}$$

Each bulk having winding numbers 0 and 1 are gapped, and a phase transition from a bulk with winding number 1 to a bulk with winding number 0 cannot occur without closing a gap or breaking chiral symmetry.

5.3 Chiral Symmetry

1D chiral symmetric systems support integer-valued winding numbers, and topological distinction can be observed when a system has two different winding numbers. Quantum walk systems can be chiral symmetric, therefore we can dictate topological invariance through bulk properties. Discrete symmetries play an important role to see topological invariance in the system. There are three discrete symmetries used in topological condensed matter systems, time-reversal, particle-hole, and chiral symmetry. Time-reversal symmetry certifies the existence of paired energies due to Kramer's degeneracy. Particle-hole symmetry is commonly used in a superconducting system where the symmetry exchanges electrons with holes. Time-reversal symmetry operator is an anti-unitary operator T satisfying $T^2 = -1$. We obtain the following relation $THT^{-1} = H$ when applied to a Hamiltonian H. Similarly, particle-hole symmetry operator P satisfies $P^2 = +1$ with $PHP^{-1} = -H$. Chiral symmetry operator is introduced by combining time-reversal and particle-hole symmetry $\Gamma = PT$. Having time-reversal and particle-hole symmetries automatically certifies the presence of chiral symmetry in the system, however the converse is not true. Chiral

symmetry is also called sublattice symmetry because a chiral symmetry operator alters the sign of the wavefunction from one sublattice to another. Such chiral symmetric operator for the SSH Hamiltonian can be defined by

$$\Gamma = P_A - P_B \tag{5.10}$$

where $P_A = \sum_{m=1}^{N} |m,A\rangle \langle m,A|$ and $P_B = \sum_{m=1}^{N} |m,B\rangle \langle m,B|$ are projecton operators for each sublattice.

The SSH Hamiltonian has chiral symmetry,

$$\Gamma H(k) \Gamma = -H(k), \tag{5.11}$$

where the operator Γ must obey Hermiticity ($\Gamma^\dagger = \Gamma$) and Unitarity ($\Gamma^\dagger = \Gamma^{-1}$). Chiral symmetry guarantees that energy eigenvalues come into pairs meaning the existence of eigenenergy E certifies the existence of $-E$. This can be shown by defining an eigenstate $|\psi_n\rangle$ of an arbitrary Hamiltonian with eigenvalue E_n. Now, we can form two equations using the Hamiltonian,

$$H |\psi_n\rangle = E_n |\psi_n\rangle \tag{5.12}$$

$$H\Gamma |\psi_n\rangle = -E_n \Gamma |\psi_n\rangle . \tag{5.13}$$

We used $\Gamma H(k) \Gamma = -H(k)$ here, and the result shows that the chiral symmetric system supports eigenenergies with opposite sign $\pm E_n$. $E_n = 0$ is a special case because this automatically tells us that $-E_n = 0$. This zero-energy is protected against perturbation which does not close the band gap (Ryu and Hatsugai, 2002). The zero-energy state is the only state that can support single energy. The rest of states are paired with opposite energy states due to the chiral symmetry, and this prohibits from generating a state having only a single energy near the zero-energy. Any deformation that moves the state away from E=0 has to split this state into two opposite-energy states in order to preserve the chiral symmetry,

so that the difference of the number of edge modes on the two sublattices $(N_A - N_B)$ remains topologically invariant. This protected energy state appears in a 1D quantum walk system because of chiral symmetry and periodicity in the system. The quantum walk systems are described using unitary matrices, we can take effective Hamiltonian approach to demonstrate the topological protection.

We take the approach introduced by (Kitagawa et al., 2010b) and (Obuse et al., 2015) for introducing topological invariants in a quantum walk system. The 1D quantum walks are introduced in Chap. 4 therefore we briefly mention the relevant quantum walk construction.

The quantum walk model uses a coin operator and a shift operator. Shift operator in real and momentum space is given by

$$\begin{aligned} S &= \sum_x |x+1\rangle\langle x| \otimes |\uparrow\rangle\langle\uparrow| + |x-1\rangle\langle x| \otimes |\downarrow\rangle\langle\downarrow| \\ &= \int_{-\pi}^{\pi} e^{ik\sigma_z} \otimes |k\rangle\langle k| . \end{aligned} \tag{5.14}$$

Similarly, the coin operator is given by

$$C = \sum_x |x\rangle\langle x| \otimes R(\theta(x)) = \int_{-\pi}^{\pi} e^{-i\theta\sigma_y} \otimes |k\rangle\langle k| \tag{5.15}$$

where

$$R = \begin{pmatrix} cos(\theta) & -sin(\theta) \\ sin(\theta) & cos(\theta) \end{pmatrix} = e^{-i\theta\sigma_y}. \tag{5.16}$$

We can obtain band structures of the system by only looking at the 2x2 matrix part of the equation since its a block diagonal matrix filled with identical 2x2 matrices. The quantum walk system is periodic, we can use Floquet formalism to obtain the energy eigenvalue $E(k)$ of the effective Hamiltonian H_{eff} using $U = e^{-iH_{eff}}$.

$$U = SC = e^{ik\sigma_z} e^{-i\theta\sigma_y} = e^{-iE(k)} \tag{5.17}$$

This equality gives

$$cos(E(k)) = cos(k)cos(\theta). \tag{5.18}$$

From the equation above, the band diagram of Hadamard quantum walk can be drawn and the band gap closes at $\theta = 0, \pi$.

The effective Hamiltonian for this QW can be written as

$$H_{eff} = \int_{-\pi}^{\pi} dk[E(k)n(k) \cdot \sigma] \otimes |k\rangle \langle k| . \tag{5.19}$$

The unit vectors are $n(k)$ for this specific quantum walk structure.

$$n(k) = \frac{(\sin(\frac{\theta}{2})sin(k), \sin(\frac{\theta}{2})cos(k), -\cos(\frac{\theta}{2})sin(k))}{sin(E(k))}. \tag{5.20}$$

$\sigma = (\sigma_x, \sigma_y, \sigma_z)$ are pauli matrices. The quantum walk is performed using unitary operators. To show that the system has chiral symmetry, we can translate the Hamiltonian chiral symmetry to unitary matrix based chiral symmetry $\Gamma U \Gamma^{-1} = U^{-1}$. Periodicity is present in the system and it implies that $E = -E$ would occur at $E = \pi$ in addition to $E = 0$. $E = 0$ stems from chiral symmetry without periodicity and $E = \pi$ is unique to periodically driven systems. Any periodically driven systems can support this π-energy.

An example chiral symmetry operator (Kitagawa et al., 2010b) is given by

$$\Gamma^{-1} H_{eff} \Gamma = -H_{eff} \Gamma = e^{-\pi A \cdot \frac{\sigma}{2}} \tag{5.21}$$

where $A = (cos(\frac{\theta}{2}), 0, sin(\frac{\theta}{2}))$. The chiral symmetry operator is θ dependent and θ is location dependent variable, therefore this operator makes it difficult to keep track of the symmetry of the entire system when some θ values are varied independently.

There is another method for identifying a chiral symmetry operator by shifting time of origin within the quantum walk (Obuse et al., 2015; Asbóth and Obuse, 2013; Rakovszky

and Asboth, 2015). The quantum walk repeats the procedure to show the propagation of the amplitudes meaning we need to apply the unitary operator U multiple times (e.g. $U^n = SCSCSC\cdots$). We can find two chiral symmetric time frames which satisfy the condition of θ being independent.

$$U' = C\left(\frac{\theta}{2}\right)SC\left(\frac{\theta}{2}\right) \text{ and } U'' = SC(\theta)S. \tag{5.22}$$

In this model, $\Gamma = \sigma_x$, θ independent operator satisfies the chiral symmetry condition. Winding number for zero energy state and π energy is derived by looking at the two time frames $U^{'}$ and $U^{''}$. In a simple Hadamard quantum walk, there are only two topologically distinct winding numbers.

5.4 Numerical Analysis of Topological Protection of Bulk States

The existence of localized, topologically protected states under the condition of having a distinct winding number at each bulk has been extensively studied. It has been demonstrated that under certain conditions, bulk wave-functions can also be made to be "suppressed" (Simon et al., 2018b). Here, suppression implies the amplitude propagation from one bulk to another bulk. The suppression amount depends on the hopping parameter as well as the discrete change of topology. We examine the amount of transmission by considering a simple quantum walk system $U = SC(\theta)$ under the influence of topological difference in winding number. We have introduced an edge based quantum walk in the previous chapters. Because one quantum walk model can be transformed into another quantum walk model by a unitary matrix and they both have the same set of eigenvalues. For this reason, we use the two quantum walk models interchangeably. The system consists of two bulk regions by setting coin operator differently at each bulk. This model is called a single step quantum walk or two-phase quantum walk (Endo et al., 2015). The right side of the region is governed by θ_R and the left side has θ_L. We show the existence of protection from

propagating into another region having a different winding number numerically. Distinct winding numbers can be obtained in the following coin phase relationship. Technically speaking, we have winding numbers for both zero energy and π energy, however, the system only has two distinct topological states or phases, therefore we use the equation below to introduce winding number difference between two bulks.

$$\Delta\nu = \begin{cases} 0 & (0 < \theta_R < \pi) \cap (0 < \theta_L < \pi) \text{ or } (\pi < \theta_R < 2\pi) \cap (\pi < \theta_L < 2\pi) \\ 1 & (\pi < \theta_R < 2\pi) \cap (0 < \theta_L < \pi) \text{ or } (0 < \theta_R < \pi) \cap (\pi < \theta_L < 2\pi) \end{cases} \tag{5.23}$$

Consider a quantum walk system consisting of 100 sites. The two ends of a chain is connected to form a loop. We provide numerical simulation of the topological protection, eigenvalue distribution of the unitary matrix, bulk state transition, and probability distribution for all possible phase values. All the simulations in this chapter are performed using MATLAB (see Appendix C). To perform the simulation, a 200 by 200 unitary matrix $U = SC$ for a single step is constructed. The unitary matrix U is $U(\theta_L)$ for spatial location $-50 \leq m \leq 0$, and $U(\theta_R)$ for spatial location $0 < m < 50$. An amplitude with spin up and spin down are distributed through out the system by the 200 by 200 unitary matrix. Amplitudes with spin up and spin down are independently summed at each site, therefore the final probability distribution has 100 sites. When a spin up photon is inserted at the boundary (lattice site = 0) of two topologically distinct bulks, highly localized amplitude appears at the boundary as shown in Fig. 5·2 (a). In this simulation, the number of walk steps is 50. Topological distinction is provided by setting phase values $\theta_R = \frac{9\pi}{8}$ and $\theta_L = \frac{\pi}{8}$ since $\Delta\nu = 1$. If $\theta_R = \frac{\pi}{8}$, $\theta_L = \frac{\pi}{8}$ are chosen, the winding numbers of the two bulks are identical, therefore edge state disappears as indicated in Fig. 5·2 (b). We also provided eigenvalue distribution for both unitary matrices. Eigenvalues correspond to edge states are isolated from the clustered regions. The eigenvalues are rotated by applying $e^{i\frac{\pi}{2}}$ globally. Global operation does not change the winding number (Obuse et al., 2015).

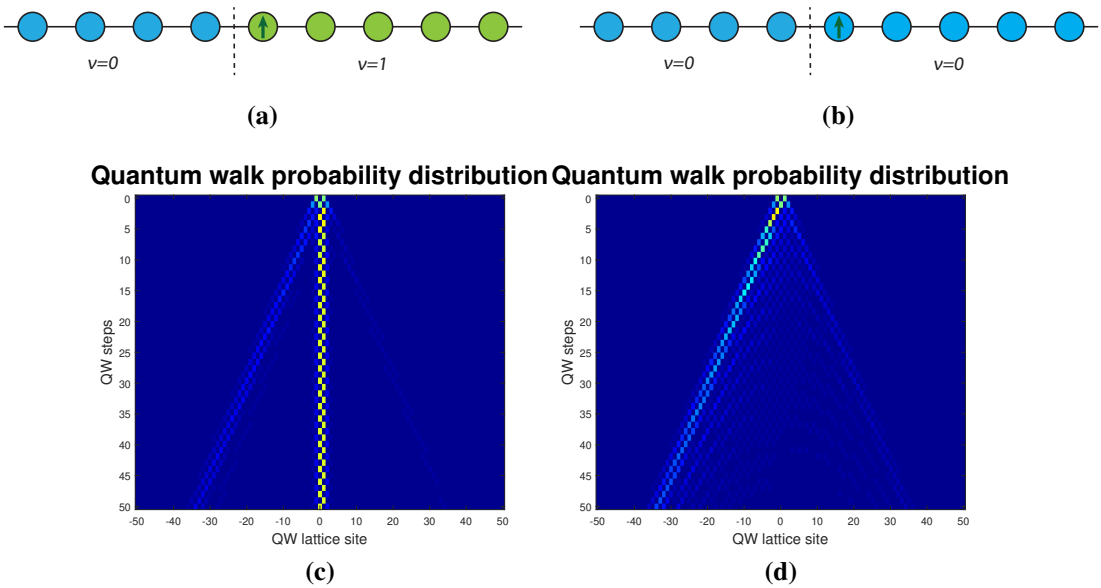

Figure 5·2: Quantum walk with topological boundaries. The chain length is 100 with quantum walk steps equal to 50. Site 50 and -50 are connected because of the ring structure. We set topological boundaries between -1 and 0, and between site 50 and -50 in x-axis. (**c**) Topologically protected edge state. Right side phase is set to $\frac{9\pi}{8}$ and left side phase is set to $\frac{\pi}{8}$. (**d**) Edge state does not appear when $\Delta\nu = 0$. Right side phase is set to $\frac{\pi}{8}$ and left side phase is set to $\frac{\pi}{8}$.

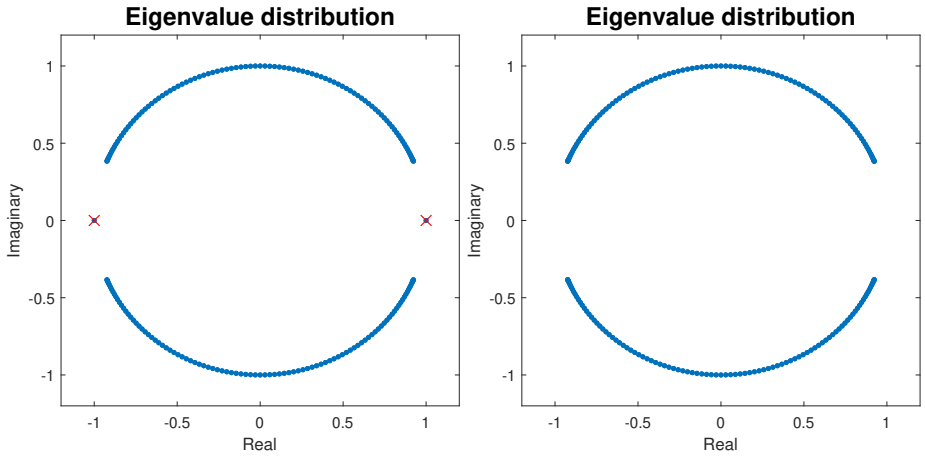

Figure 5·3: Its corresponding eigenvalue distributions to the previous quantum walk plot. The plots show the eigenvalue of the quantum walk unitary matrix. The distribution is rotated by multiplying $e^{i\frac{\pi}{2}}$ globally. (**a**) Topologically protected edge state appears at 1 and -1. Right side phase is set to $\frac{9\pi}{8}$ and left side phase is set to $\frac{\pi}{8}$. (**b**) Edge state does not appear at 1 and -1. Right side phase is set to $\frac{\pi}{8}$ and left side phase is set to $\frac{\pi}{8}$.

The origin of the quantum walk is shifted away from the boundary to demonstrate the suppression of amplitude transition from one bulk to another bulk when topological distinction is present. This numerical simulation is shown in Fig. 5·4. Here, the input photon is inserted at site 25 and the system forms a loop, therefore the system has two boundaries. In Fig. 5·4 (a), the input photon meets the boundary enough times by performing 1000 steps, yet the leakage of probability is small when two bulks are topologically distinct. Topologically distinct system has $(\theta_R, \theta_L) = (\frac{13\pi}{8\pi}, \frac{5\pi}{8})$. In Fig. 5·4 (b), the phases are set to $(\theta_R, \theta_L) = (\frac{5\pi}{8}, \frac{5\pi}{8})$ and topological suppression no longer exists.

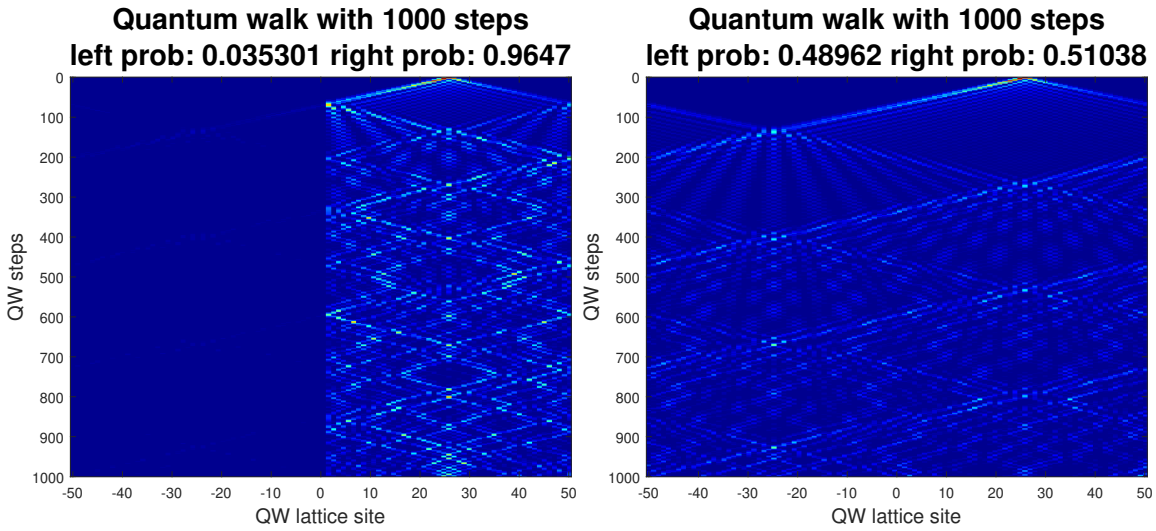

Figure 5·4: Shifted quantum walk with 1000 steps. A photon is inserted at lattice site 25. We set a topological boundary at 0 in x-axis. Site 50 and -50 are connected because of the ring structure. (a) Topological region. The input photon does not leak into left side of the bulk. The probability distribution between left side bulk and the right side bulk is 3.5% and 96.5% respectively. (b) Topological region. When the two bulks are topologically not distinct, the input photon penetrates the boundary therefore the photon propagates the entire system without reflection. The probability distribution between left side bulk and the right side bulk is 49% and 51% respectively.

We show the topologically protected regions in Fig. 5·5 by searching through the entire coin phase angle space. The topological boundary is shown in red line. The phase resolution is $\frac{\pi}{100}$ with the chain length equal to 100. The initial quantum walk point is at $+25$ and the total walk steps at each phase setting is 2000. When $\theta = \frac{\pi}{2}$ or $\frac{3\pi}{2}$, $cos(\frac{\pi}{2}) = 0$ and $sin(\frac{\pi}{2}) = 1$, therefore the photon stays at the original location and never reaches the boundary. This explains the zero leakage when such phase settings are employed. We can look further into the difference between topological and non-topological probability distributions in Fig. 5·6.

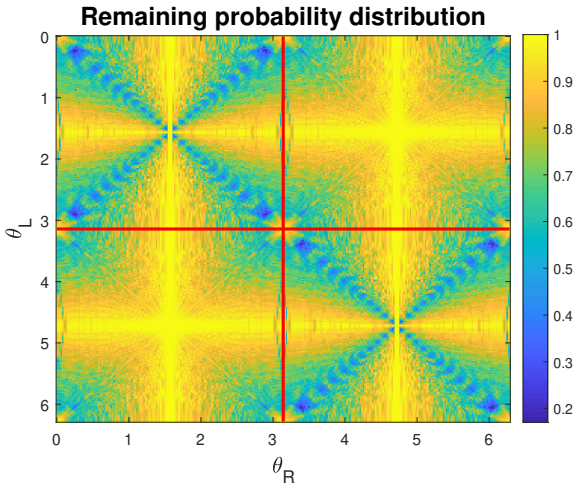

(a)

Figure 5·5: Probability distribution of a quantum walk system. The phase values on the right side and the left side are translated to cover the entire phase space. Topologically distinct region ($\Delta\nu = 1$) is on the right top and left bottom side of the diagram while topologically equivalent regions are on the right bottom and left top side. As indicated, for example, left top side has significantly more leakage of probability compared to the topological regions.

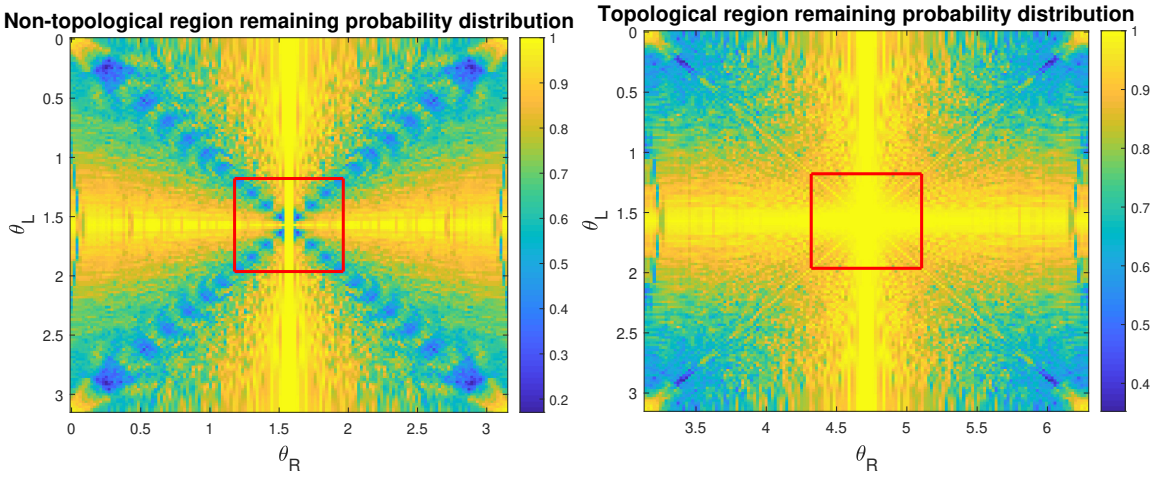

(a) **(b)**

Figure 5·6: (a) Non-topological region. (b) Topological region. The red box shows strongly suppressed region compared to the non-topological bulks. The side length of the box is $\frac{\pi}{4}$

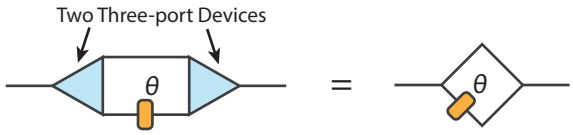

Figure 5·7: Two multiports and a phase shifter are used to construct a diamond-shaped structure. The multiports are viewed as scattering centers at edges of an optical graph. Detailed properties of this structure may be found in (Feldman and Hillery, 2004; Feldman and Hillery, 2007).

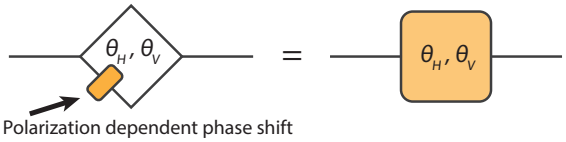

Figure 5·8: The unit cell for the proposed systems is the diamond graph with polarization dependent phase shifts θ_H and θ_V, as shown on the left. Each such cell contains four three-ports. This basic unit will be drawn in the schematic form shown on the right.

5.5 Jointly-Entangled Topologically Error Suppressed Bulk States

We have demonstrated the propagation suppression of amplitudes between topologically distinct bulks in the previous section. We can apply this suppression to an error suppressed quantum information processing scheme by engaging in polarization degrees of freedom. The system we are using is based on chiral symmetry protected system based on quantum walk. Start with a polarization-entangled photon source, type-II SPDC in a nonlinear crystal. We define a maximally polarization entangled two photon state,

$$|\psi^{\pm}\rangle = \frac{1}{\sqrt{2}}\left(|H\rangle_1 |V\rangle_2 \pm |V\rangle_1 |H\rangle_2\right), \tag{5.24}$$

where 1 and 2 refer to two spatial modes. Our goal is to produce a winding number entangled state. Polarization entanglement needs to remain intact, to use for control and measurement purposes. It should be noted that we are making a slight abuse of terminology

here: the winding number is associated with the Hamiltonian, not strictly speaking with the state. Transitions of bulk states between spatial regions or parameter values with Hamiltonians of different winding numbers can be arranged to be suppressed. Therefore, as a practical matter, under appropriate conditions one may to a high degree of accuracy think of the winding number as being associated with the state as well. We introduce an abstract unit cell using two directionally-unbiased three-port devices. Strictly speaking, the change in θ in the diamond unit is not identical to the coin operator in the quantum walk model. However, the amplitudes produced from the diamond unit spans the same spectrum generated by the coin operator, therefore we treat them the same. If we look at the probability distribution of coin based quantum walk and edge based quantum walk independently without performing the additional unitary transformation, some details on probability distribution would be different, but the overall structure is the same. Consider two chains of unit cells introduced in Fig. , distinguishing the upper (u) and lower (l) chains (Fig. 5·9). Using the states $|\psi^{\pm}\rangle$ as input, each down conversion photon is directed into one of the two chains, so that the labels 1 and 2 in Eq. 5.24 are replaced to u and l. A set of optical circulators and switches, as described in (Simon et al., 2017a) is one way of introducing photon pairs into the system. The circulators are used only to couple photons into the system initially, and to couple them out for measurement at the end; they play no role in the actual operation of the system in between. We take polarization-dependent phase θ_H and θ_V. The polarization-dependent phase shifts are easily implemented with thin slices of birefringent material or, if real-time control of the phase shifts is desired, with Pockels cells. In the visible and near infrared, it is easy to find crystals with low absorption and strong birefringence; calcite is one example. Other materials with similar properties can be found for other spectral ranges. It should be relatively easy to produce the necessary phase shifts with negligible effect on performance. The use of electro-optical effects can enable fine adjustment of the phase shift in each cell if necessary. If θ_H is chosen correctly, then

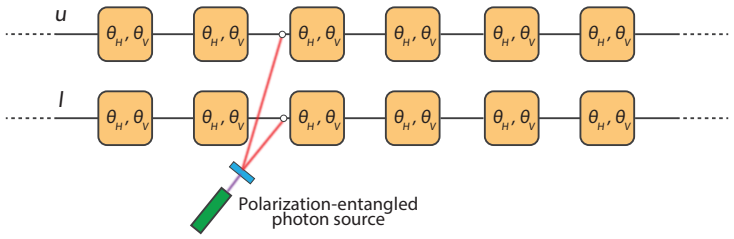

Figure 5·9: Producing winding-number-entangled two-photon states. Each unit cell consists of a diamond graph unit, and so contains a total of two three-ports and a polarization dependent phase shifter. The photons are inserted using optical isolators.

the H part is put into a state with winding number $\nu = 0$ and the V part into a state with $\nu = 1$. Then the vertically- and horizontally-polarized states will be eigenstates of Hamiltonians with respective winding numbers $\nu_V = 1$ and $\nu_H = 0$. The final state is therefore of the form

$$\frac{1}{\sqrt{2}}(|0_H\rangle_u |1_V\rangle_l \pm |1_V\rangle_u |0_H\rangle_l), \tag{5.25}$$

where the 0 and 1 represent winding number values of the Hamiltonians that govern their time evolution, while u and l denote the spatial modes in the upper and lower chains.

The state is written in condensed form here; a more explicit expression, including the spatial dependence of the wavefunction is provided in (Simon et al., 2018b). The photons now form winding number-entangled qubit pairs. All that matters is that the polarization-dependent combination (θ_H, θ_V) leads to each polarization state seeing a Hamiltonian of different winding number. Usually, the global property of winding number is difficult to determine by local measurements. This is especially true for single-photon states which are usually destroyed by the measurement process, so that multiple measurements cannot be carried out to determine the global state. Polarization and winding numbers remain coupled in this case. This jointly-entangled structure allows the variables to play disparate roles: the discrete winding number leads to topologically-enforced stability, while polarization, being defined locally, makes the photon state easy to measure. Polarization can be determined by a

single local measurement, allowing the global winding number to be inferred from its value. Suppose that a perturbation occurs to the system. Normally, this might cause the photon's polarization to change (a polarization-flip error). For example, a horizontally-polarized state of winding number ν might try to flip into a vertical state: $|\psi_\nu\rangle_H \rightarrow |\psi_{\nu'}\rangle_V$, where ν' is the final winding number. However, as discussed in more detail, unless the perturbation is strong enough to severely and globally alter the entire system, transitions from eigenstates of one bulk Hamiltonian to those of a Hamiltonian of different winding number are suppressed. If the hopping parameters are chosen appropriately as indicated in Sec. 5.4, the amplitudes for these transitions can be made arbitrarily small. This means that, to a high level of certainty, the initial and final winding numbers can be assumed to be equal: $\nu' = \nu$. Due to the way the system was constructed, there are no allowed states that have V polarization and which propagate according to a Hamiltonian of winding number ν, so the polarization flip is suppressed. Thus, barring extreme alterations of the system, polarization-flip errors are greatly reduced. The suppression of polarization errors occurs without loss of photons, and so there is no damage to any coherence or entanglement present in the system.

5.6 Topologically-Protected Quantum Memory Registers and Entanglement

A basic ingredient needed for quantum computing is a quantum memory unit capable of storing a logical qubit $\alpha|0\rangle + \beta|1\rangle$. Such units need to have read, and or write capability and should be resistant to bit-flip errors. This can be achieved by a variation on the strategy above. Once again, topological stability suppresses errors, with polarization used for reading and writing stored values. A schematic depiction of the memory register is shown in Fig. 5·10. When a horizontally-polarized photon enters the ring it is associated with winding number $\nu = 0$, but for appropriate values of θ_V a vertically polarized photon will have $\nu = 1$. The winding number then serves as the logical bit being stored. Readout of bit values requires

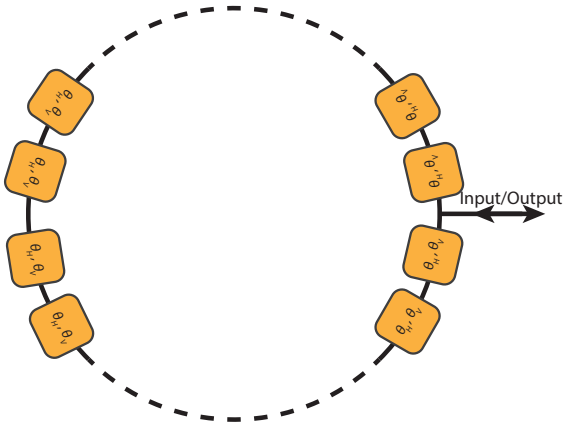

Figure 5·10: Schematic diagram of a quantum memory register. Logical bits are stored in the winding number of the state and retrieved via polarization measurement.

only simple polarization measurements. Since the input photon may be in any arbitrary superposition of polarization states, the ring can be used to store any possible qubit value. In general, an input polarization qubit $\alpha|H\rangle + \beta|V\rangle$ is stored in a winding-number/polarization qubit, $\alpha|0_H\rangle + \beta|1_V\rangle$, where 0 and 1 are winding number. Since photons at normal energies do not mutually interact to a significant degree, multiplexing is possible. Multiple qubits can be stored on a single ring by using photons of different frequency; addressing the desired qubit then simply requires opening an exit channel from the ring and using a filter or dichroic mirror with the appropriate frequency-transmission range. Reading out a qubit value consists of measuring the polarization.

Notice that the register of Fig. 5·10 consists of one strand of the structure of Fig. 5·9 wrapped into a circle; the compactification to a circle makes its use in a larger system more practical, but is not necessary for operation. Each strand of Fig. 5·9 is already capable of serving as a quantum memory. One could use both strands of Fig. 5·9 (either in the original linear configuration or compactified to a double-circle structure); for the polarization entangled input of equation (2) the result would be two entangled quantum memory registers,

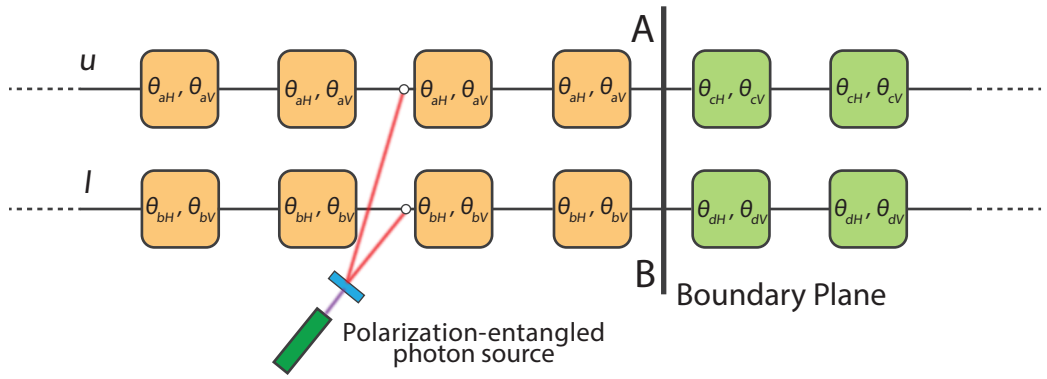

Figure 5·11: Entangled edge states. The points A and B form a boundary between bulk regions of different winding number. Polarization-entangled input states lead to winding-number entangled states at A and B.

with error suppression provided by the winding number entanglement.

5.7 Topologically-Protected Entangled Boundary States

The setup of Fig. 5·9 can be generalized to produce one further effect related to an entanglement. First, the polarization-dependent phase can be made different in the upper and lower branches (θ_{aH}, θ_{aV} in upper branch and θ_{bH}, θ_{bV} in lower). Then, a boundary plane can be introduced perpendicular to the chains, such that the polarization-dependent phase will change suddenly when the plane is crossed ($\theta_{aV} \rightarrow \theta_{cV}$ in upper branch and $\theta_{bV} \rightarrow \theta_{dV}$ in lower), as shown in Fig. 5·11. As discussed in (Simon et al., 2017b), if the phase values on the two sides of the boundary are chosen correctly, then topologically protected states appear that are tightly localized on the boundary point. Unlike the approximate winding number preservation in the bulk, the topological protection of the boundary state is exact and has been demonstrated in a number of different solid state and optical systems. Taking the simplest case, suppose $\theta_{aH} = \theta_{bH}$ and $\theta_{cH} = \theta_{dH}$ (same relationship holds for V), so that the upper and lower chains are identical. Then for polarization-entangled input (Eq. 5.24), the boundary state will be in a superposition of two positions (points A and B). These entangled boundary states will be vertically polarized and would be topologically protected.

Considering just the state at the boundary, let $|e\rangle$ and $|\rangle$ represent, respectively, the presence or absence of a localized edge state. Then the state on the boundary plane will be of the form

$$\frac{1}{\sqrt{2}}(|e_V\rangle_u |H\rangle_l \pm |H\rangle_l |e_V\rangle_u). \tag{5.26}$$

where we assume as before that vertical polarizations see different winding numbers on the two sides of the boundary and horizontal polarizations do not. Here, as before, u and l label whether the spatial mode is in the upper and lower branch. Note that this entanglement is distinct from path entanglement; photons exist simultaneously in both branches, even if edge states are absent from a given branch. Another possibility is to take $\theta_{aV} \neq \theta_{cV}$ for the vertical polarization in the upper chain, but in contrast to take $\theta_{bH} \neq \theta_{dH}$ for horizontal polarization in the lower chain; in this case, there would be an entangled state which is a superposition of having either localized boundary states at both A and B or at neither:

$$\frac{1}{\sqrt{2}}(|e_V\rangle_u |e_H\rangle_l \pm |H\rangle_l |V\rangle_u). \tag{5.27}$$

The states of Eq. 5.26 and 5.27 are maximally entangled, with entropy of entanglement equal to 1, and may be thought of as topologically-stable implementations of Bell states; these states can also be used to store entangled qubits. Edge states appear due to interference between various amplitudes for quantum walks through each chain; they should survive as long as the photons remain contained inside the system, coherent and unmeasured. Small perturbations in the refractive index or in path lengths along the photon trajectories should not disturb the results. For example, numerical results are displayed in Sec. 5.4 that show the boundary state persists over some range of quantum walk phase parameters, as long as the winding numbers do not change.

5.8 Conclusion

We have proposed a hybrid strategy for quantum information processing, in which local and global properties (polarization and winding number) are jointly-entangled, allowing one to simultaneously exploit the benefits of both: discreteness of global, topological properties affords stability and error suppression, while local properties are easy to manipulate and measure. This has applications in producing entangled topological states and in designing quantum registers (possibly in entangled pairs) with topologically-assisted reduction of bit-flip errors.

Besides reducing bit-flip errors, the use of discrete topological quantities also helps maintain loss of entanglement through the same mechanism: if there are no non-entangled joint states that a photon pair can scatter into, then the entanglement will remain robust. This can help avoid some of the problems that occur in many approaches to quantum computing as a result of the fragility of entangled states. Efficient measurement of topological quantum numbers has been a longstanding problem. Although other methods of measuring topological variables in photonic systems have been proposed or carried out (Longhi, 2013; Ozawa and Carusotto, 2014; Hafezi, 2014; Tarasinski et al., 2014; Barkhofen et al., 2017), they require determination of probability amplitudes by measurements on multiple photons. The method given here has the advantage of being able to operate at the single photon level.

Chapter 6

Multiphoton State Manipulation

6.1 Introduction

Global properties of a photonic system were used to perform quantum information processing in the previous chapter. In this chapter, we present information processing using local photonic state manipulation by utilizing the clustering effect of photons. The Hong-Ou-Mandel (HOM) effect (Hong et al., 1987) shown in Sec. 2.3 is arguably the best known two-photon interference effect. Two identical photons are simultaneously incident on different inputs of a 50/50 beam splitter (BS) as in Fig. 6·1. Each photon could exit either output port, so naively one expects nonzero amplitudes for three possible outcomes: both exiting at port 3, both exiting at port 4, or one photon each at ports 3 and 4. But in fact, no coincidences are seen between 3 and 4; the two photons always leave at the same port. *Which* port the pair exits is entirely random. Coincidences between the two output ports are absent because of cancellations between the two indistinguishable processes. As a result, the two photons always remain clustered together in the same output spatial mode. This gives a method for measuring time intervals to sub-picosecond level accuracy: as a delay between the photons varies, the coincidence rate exhibits a sharp dip (the HOM dip) when the wavefunctions briefly overlap on the BS.

Similarly, various types of studies on quantum state transformations in multiport devices have been performed such as two photon propagation in a multimode system (Weihs et al., 1996b; Żukowski et al., 1997), quantum interference effects using a few photons (Meany et al., 2012; de Guise et al., 2014; Tichy et al., 2011; Campos, 2000), and propagation of

multi-photons (Lim and Beige, 2005; Tillmann et al., 2015; Menssen et al., 2017). Internal degrees of freedom are also incorporated to enhance communication capacity (Walborn et al., 2003; Poem et al., 2012; Zhang et al., 2016). Systems and procedures using multi-photon states, such as boson sampling, have been analyzed using multiport beam splitters both theoretically and experimentally (Aaronson and Arkhipov, 2011; Tillmann et al., 2013; Spring et al., 2013; Bentivegna et al., 2015; He et al., 2017; Wang et al., 2019). The HOM effect plays an important role in the field of quantum metrology when two-photon $|2002\rangle$-type states are extended to N-photon $N00N$ state (Dowling, 2008; Motes et al., 2015).

Additionally, coherent transport of quantum states has been attracting attention, where single- and two-photon discrete-time quantum walk schemes are employed to transfer and process quantum states (Bose, 2003; Perez-Leija et al., 2013; Lovett et al., 2010; Chapman et al., 2016; Nitsche et al., 2016). A quantum routing approach has been proposed to transfer unknown states in 1D and 2D structures to assist quantum communication protocols (Zhan et al., 2014; Štefaňák and Skoupỳ, 2016; Bartkiewicz et al., 2018). Photon propagation control is especially crucial in a large optical network to distribute quantum states between

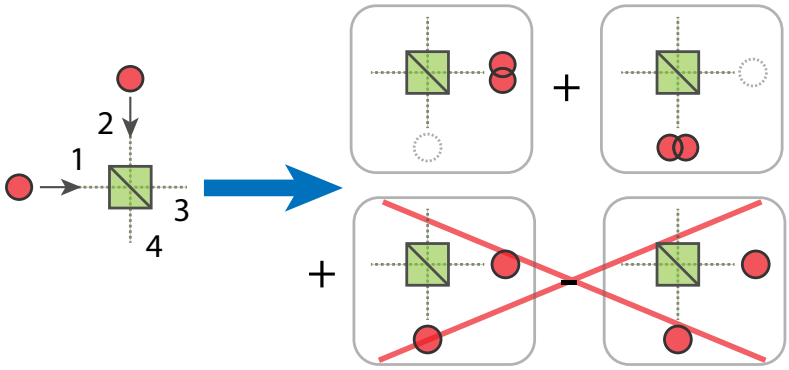

Figure 6·1: Two photons entering a beam splitter at different ports. Although exiting at a random output port, both photons are always found to cluster together in the *same* port.

two parties. The network can be formed by combining multiple copies of four-port devices.

Here, we look at an arrangement in which two indistinguishable bosons undergo a discrete-time quantum walk along a dual rail or ladder type system (Fig. 6·2), with a four-dimensional Grover matrix at each vertex. Such a chain could be considered as a pair of quantum wires (representing a pair of states), with the Grover matrix serving as directional couplers (Fan et al., 1998; Nikolopoulos, 2008) between them; more pertinently to our purposes here, we may also think of the system as a single double-stranded quantum wire in which we care only about the horizontal location of the particle, not whether it is on the upper or lower strand.

The Grover matrix can be implemented using a linear-optical four-port, which is a special case of the directionally-unbiased multiports studied in Chap. 3. We use the reversible four-ports in this specific setup which can be implemented using any of the four-port device in Chap. 3. The system is based entirely on linear optics, with no interactions between the photons. In particular, if the photons are *distinguishable*, then each exhibits an independent quantum walk and can later be detected in widely separated spatial regions. However, once the photons become *indistinguishable*, the two-photon interference alters the picture: it displayed below that for a particular input state the two photons remain spatially clustered and are always found at the *same* horizontal location at each moment. Moreover, the two-photon amplitude shows no sign of the randomness normally associated with random walks: it splits into a quantum superposition of two localized packets that each move deterministically over time with the two photons always remaining clustered in one packet or the other.

These effects depend only on indistinguishable photons being inserted into the same Grover matrix vertex simultaneously; entanglement is not required. Experimentally, the most practical realization of the structures described here are on integrated optical chips. Losses, decoherence, and chip imperfections will of course limit the possible walk lengths

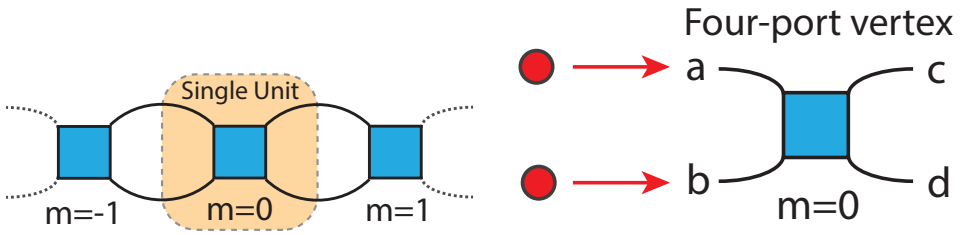

(a) Single unit. **(b)** A chain of four-ports.

Figure 6·2: (a) A chain of four-ports connected by pairs of edges. Each edge pair is thought of as a single double-stranded connection line, and vertex positions are labeled by integers. (b) The initial state consists of two indistinguishable, right-moving photons injected into two ports from the left side of $m = 0$ multiport, in the middle of the chain.

of experimental implementations. Up to this point, quantum walks of both single photons and of entangled photon pairs have typically been implemented using integrated optics for walks of lengths on the order of five to ten time steps (for example, (Peruzzo et al., 2010; Sansoni et al., 2012; Crespi et al., 2013b; Su et al., 2019)), although proposals have been made for arrangements that may allow longer walks (Geraldi et al., 2019). In what follows, we assume an idealized system, neglecting losses and other imperfections.

6.2 System Setup

Consider a directionally-unbiased four-port acting as the Grover matrix (Moore and Russell, 2002; Carneiro et al., 2005) indicated in Fig. 6·2 (b). The action of the four-port is given by the unitary matrix

$$M = \frac{1}{2}\begin{pmatrix} -1 & 1 & 1 & 1 \\ 1 & -1 & 1 & 1 \\ 1 & 1 & -1 & 1 \\ 1 & 1 & 1 & -1 \end{pmatrix}, \tag{6.1}$$

where rows and columns represent the four-ports. Regardless of which port a photon enters, exit amplitudes at all outputs are real and equal in magnitude. Importantly, the amplitude to reflect back to the input port has an extra minus sign relative to all other transitions. In

general, photons in modes a and b are transformed in the following manner,

$$a \xrightarrow{M} \frac{1}{2}(-a+b+c+d) \text{ and } b \xrightarrow{M} \frac{1}{2}(a-b+c+d). \tag{6.2}$$

We simplify creation operator by dropping the hat and dagger notations.

Consider two photons entering the linear chain of Fig. 6·2 simultaneously. Assume one enters port a and the other enters port b of the same multiport, somewhere in the middle of the chain, far enough from the ends that we do not need to worry about the photons leaving the system during the time duration of the experiment. Experimentally, two photons can be produced simultaneously using spontaneous parametric down conversion (Boyd, 2020) and then coupled into the chain by means of an electro-optical or magneto-optical switch. Horizontal positions are specified by an integer m corresponding to the multiport label, and discrete time $t = nT$ by integer n, where T is the photon travel time between multiports. At time $n = 0$, the photons are moving rightward, entering the $m = 0$ multiport.

Then, if the locations of the two photons at any later time $n > 0$ are measured, two striking things are found. First, the photons cluster spatially: if the two parallel input/output edges between adjacent multiports are treated as a single double-stranded connecting line, then the photons are always found on the *same* double line. Assuming no loss and ideal measuring devices, measurement at any horizontal location always finds either two photons or none. This can be seen as a quantum walk analog of the HOM effect: amplitudes for indistinguishable outcomes in which the photons move apart always cancel among themselves. However, the HOM quantum interference effect occurs just once, whereas clustering of the walk persists indefinitely, over an arbitrarily long sequence of steps.

Second, this clustered two-photon amplitude behaves in an unusual manner. It breaks after the first step into a *sustainable superposition of two distinct localized states*. One two-photon cluster in the superposition moves away from the starting point ballistically, exhibiting no randomness. The other cluster stays near $m = 0$, bouncing back and forth

between two adjacent locations (a phenomenon dubbed oscillatory localization (Ambainis et al., 2016)).

For comparison, imagine a *single* photon entering the present system, initially localized on one input port. This can be seen as the sum of two states: one symmetric over the upper and lower lines and one antisymmetric,

$$\begin{aligned} |1\rangle &= a|0\rangle = \frac{1}{2}(a+b)|0\rangle + \frac{1}{2}(a-b)|0\rangle \\ &= \frac{1}{2}(|1\rangle + |2\rangle) + \frac{1}{2}(|1\rangle - |2\rangle) \\ &= |\psi_s\rangle + |\psi_a\rangle . \end{aligned} \tag{6.3}$$

The symmetric part will always continue rightward at each step, while the antisymmetric portion reflects at each step, leading to oscillations. These single-particle behaviors have been previously discussed in (Ambainis et al., 2016) for the Grover matrix systems. What is remarkable in the two-particle case is that measurement of the two particles will always find them in the *same* part of the superposition; one will never be found in the oscillating portion and the other in the ballistic portion. Which part of the superposition the two photons are found to be clustered in is completely random, just as the output port in which the two photons are clustered in the HOM effect is purely random.

The two halves of the clustered amplitude do not spread as they propagate, exhibiting soliton-like behavior. Note that the wavepacket spread in quantum walks is of statistical origin, not a result of dispersive material properties. Therefore, cancellation of spreading occurs in the current system from linear interference processes, with no need for nonlinear interactions.

6.3 Time Evolution

6.3.1 First Time Step

We sketch the time evolution of the system in this subsection. Momentarily treating the photons as distinguishable, there are 16 possible exit outcomes from the four-ports for the input state *ab*.

Applying tensor product $U \otimes U$ to the two-photon input, each of these real exit amplitudes has absolute value $(\frac{1}{2})^2 = \frac{1}{4}$ if the photons exit at *different* ports, or $\frac{\sqrt{2}}{4} = \frac{1}{2\sqrt{2}}$ if they exit at the *same* port. (The extra $\sqrt{2}$ appears when the indistinguishability is restored, due to the normalization of two-boson Fock states, $|2\rangle = \frac{1}{\sqrt{2}} a^{\dagger 2} |0\rangle$.) Amplitudes gain one minus sign for each photon that exits back out the port through which it entered.

The initial state is $|\psi_0\rangle_{in} = a_m b_m |0\rangle_{RR}$; the notation $a_m b_m |0\rangle_{RR}$ (or $a_m b_m |0\rangle_{LL}$) means one right-moving (left-moving) photon in port a and one in port b at lattice site m. The resulting output state is

$$\begin{aligned} |\psi_1\rangle &= \frac{1}{4}(c_m c_m |0\rangle_{RR} + d_m d_m |0\rangle_{RR} - a_m a_m |0\rangle_{LL} - b_m b_m |0\rangle_{LL}) \\ &+ \frac{1}{2}(c_m d_m |0\rangle_{RR} + a_m b_m |0\rangle_{LL}), \end{aligned} \tag{6.4}$$

or simply

$$a_0 b_0 |0\rangle \xrightarrow{M} -\frac{1}{4}(a_0 - b_0)^2 |0\rangle + \frac{1}{4}(c_0 + d_0)^2 |0\rangle . \tag{6.5}$$

Assume we only want to know the exit direction of the photons (left or right), and do not care if the photon is in the upper or lower channel. Then, clustering can already be seen in the transition probabilities for the first step of the walk:

One possible outcome is for both photons entering the left side of the multiport to exit back on the left side ($LL \to LL$). The probability of this is the sum of three terms corresponding respectively to the amplitudes of both photons exiting at port 1, one photon

at each port, and both at port 2:

$$\begin{aligned} P(LL \to LL) &= P(ab \to aa) + P(ab \to ab) + P(ab \to bb) \\ &= \left(-\frac{1}{2\sqrt{2}}\right)^2 + \left(\frac{1}{2}\right)^2 + \left(-\frac{1}{2\sqrt{2}}\right)^2 = \frac{1}{2}. \end{aligned} \tag{6.6}$$

Similarly, both photons can exit right (ports 3 and 4):

$$\begin{aligned} P(LL \to RR) &= P(ab \to cc) + P(ab \to cd) + P(ab \to dd) \\ &= \left(\frac{1}{2\sqrt{2}}\right)^2 + \left(\frac{1}{2}\right)^2 + \left(\frac{1}{2\sqrt{2}}\right)^2 = \frac{1}{2}. \end{aligned} \tag{6.7}$$

Finally, one photon can exit left and one right. The appearance of extra minus signs in half the amplitudes leads to complete cancelation:

$$\begin{aligned} P(LL \to LR) &= P(ab \to ac) + P(ab \to ad) + P(ab \to bc) + P(ab \to bd) \\ &= 0. \end{aligned} \tag{6.8}$$

The result is that *even though the photons do not interact and should walk independently, they in fact always step in the same direction: both go right or both go left*. Destructive interference between indistinguishable amplitudes conspires to eliminate outcomes in which they step in opposite directions.

6.3.2 Subsequent Steps

The paragraphs above describe the first step. Transition amplitudes can again be tabulated to find the outcomes of subsequent steps. Summing over unmeasured intermediate states in previous steps, one finds the amplitude splitting into an equal superposition of two two-photon states.

The output of the first step (Eq. 6.4) can be written as

$$|\psi_1\rangle_{out} = |\psi_t; 0, RR\rangle + |\psi_r; 0, LL\rangle\,, \tag{6.9}$$

where

$$\begin{aligned} |\psi_t; m, RR\rangle &= \frac{1}{4}\left(c_m c_m |0\rangle_{RR} + d_m d_m |0\rangle_{RR}\right) + \frac{1}{2} c_m d_m |0\rangle_{RR} \\ &= \frac{1}{4}(c_m + d_m)^2 |0\rangle_{RR}, \end{aligned} \tag{6.10}$$

$$\begin{aligned} |\psi_r; m, LL\rangle &= -\frac{1}{4}\left(a_m a_m |0\rangle_{LL} + b_m b_m |0\rangle_{LL}\right) + \frac{1}{2} a_m b_m |0\rangle_{LL} \\ &= -\frac{1}{4}(a_m - b_m)^2 |0\rangle_{LL}. \end{aligned} \tag{6.11}$$

Here, we used the fact that states leaving ports c and d enter the adjacent vertex at ports a and b, respectively.

Suppressing some labels for brevity, one finds that applying $U \otimes U$ again gives

$$\begin{aligned} \frac{1}{2\sqrt{2}}(a^2 + b^2) &\to \frac{1}{4\sqrt{2}}(c^2 + d^2 + a^2 + b^2) + \frac{1}{2\sqrt{2}}(cd - ab) \\ \frac{1}{\sqrt{2}}(ab) &\to \frac{1}{4\sqrt{2}}(c^2 + d^2 - a^2 - b^2) + \frac{1}{2\sqrt{2}}(cd + ab) \end{aligned} \tag{6.12}$$

Taking the sum of these as in Eq. 6.10, one finds that the amplitudes $a^2 |0\rangle$, $b^2 |0\rangle$, and $ab |0\rangle$ cancel out at each step, so that $|\psi_t\rangle$ simply reproduces itself, but shifted one step to the right:

$$|\psi_t; m, RR\rangle \to |\psi_t; m+1, RR\rangle \to |\psi_t; m+2, RR\rangle \to \ldots. \tag{6.13}$$

This is the *ballistic* state: it is *totally transmitting* at each step. If the initiating state of the walk had been moving left ($c_m d_m |0\rangle_{LL}$ instead of $a_m b_m |0\rangle_{RR}$), similar ballistic motion occurs to the left.

The multiport action on $|\psi_r\rangle$ of Eq. 6.11 is found by taking the difference of Eqs. 6.12, leading to cancellation of $c^2 |0\rangle$, $d^2 |0\rangle$, and $cd |0\rangle$ terms. $|\psi_r; m, RR\rangle$ simply reflects at each multiport encounter, causing it to bounce back and forth indefinitely:

$$|\psi_r; m, RR\rangle \to |\psi_r; m-1, LL\rangle \to |\psi_r; m, RR\rangle \to \ldots. \tag{6.14}$$

The state is *totally reflecting* at each step, and the amplitude acts as if it is confined in a virtual cavity, oscillating between lattice sites $m = 0$ and $m = 1$.

Up to a spatial shift of one step per unit time, the states $|\psi_t\rangle$ and $|\psi_r\rangle$ are both eigenstates of $(U \otimes U)^2$, with eigenvalue $+1$, so evolution on subsequent steps is simply a repetition of what happened in the first two steps: one two-photon amplitude repeatedly reflects, the other repeatedly transmits.

Therefore, the photons remain spatially clustered as they walk along the line. This quantum walk-based analog of the HOM effect might be referred to as a *quantum-clustered two-photon walk*. In addition, the two-photon state at each moment localizes onto a quantum superposition of just two nondispersive spatial amplitudes: one moves ballistically at constant speed, while the other flips direction at each step and never moves more than one unit from its starting point. This is analogous to the single-particle Grover walk behavior, but with the unexpected feature that the two photons are always found clustered in the same localized part of the distribution and never separate from each other.

The behavior of the system is shown in Fig. 6·3 (a), where the amplitude for the position of each photon is shown. It is clearly seen that the amplitude splits into two localized portions, with one portion staying near the origin and the other moving away at constant speed. Moreover, it can be seen that the two indistinguishable photons remain together: there is no amplitude away from the diagonal. In contrast, if the two photons are distinguishable (Fig. 6·3 (b)), the lack of destructive interference leads to the appearance of nonzero off-diagonal amplitudes, indicating that the photons may become spatially separated.

We have been only considering the Grover matrix propagation. We provide four dimensional Fourier matrix propagation to demonstrate the difference in behavior (Fig. 6·4). The Grover matrix system completely localizes the photons and perfectly propagates its amplitude, however this is not the case because of the absence of the amplitude cancellation at each four-port site.

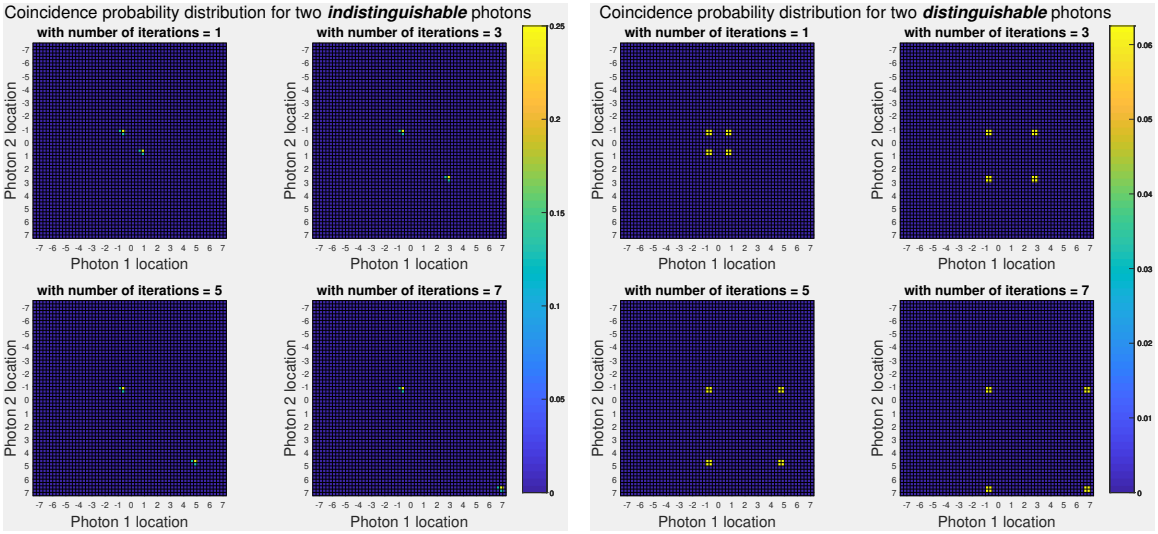

(a) Distinguishable input state

(b) Indistinguishable input state

Figure 6·3: Coincidence distribution with Grover matrix. (a) The spatial distribution of the photon amplitudes for two photons at four different times, given an initial state with two *indistinguishable* photons entering ports one and two of the four-port at position $m = 0$. The two axes give the locations of the two photons, labelled by the integer-valued four-port index. It can be observed that the amplitude splits into two localized components, but the two photons are always found clustered together within the *same* component, as indicated by the absence of amplitude away from the descending diagonal. (b) The spatial distribution of the photon amplitudes for two *distinguishable* photons. In contrast to the indistinguishable case, off-diagonal terms appear, indicating that the two photons no longer remain clustered together

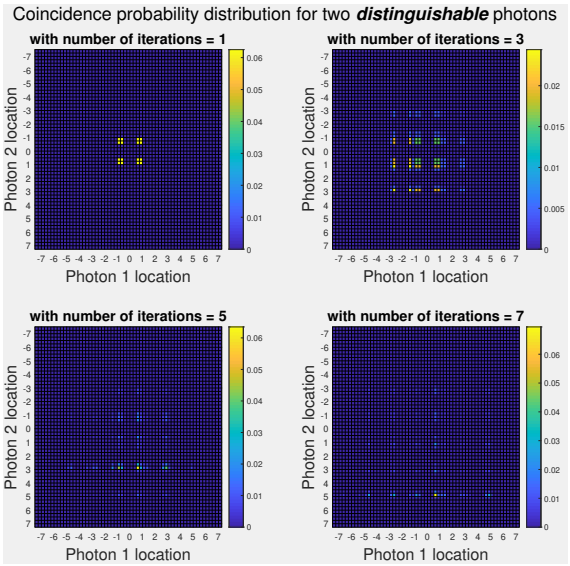

(a) Distinguishable input state

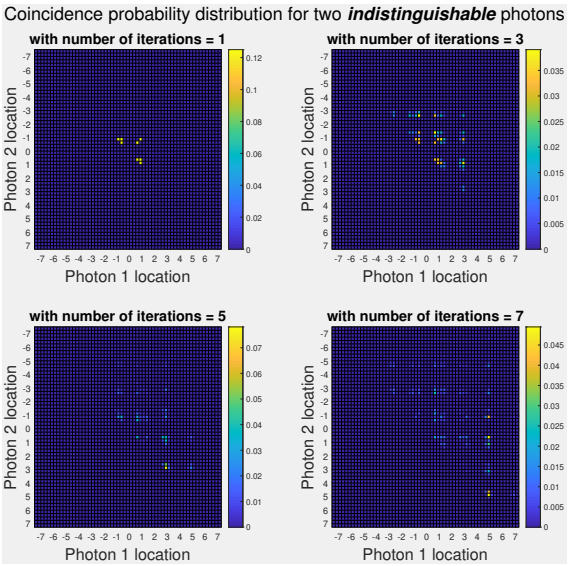

(b) Indistinguishable input state

Figure 6·4: Coincidence distribution with Fourier matrix. (a) The spatial distribution of the photon amplitudes for two photons at four different times, given an initial state with two *indistinguishable* photons entering ports one and two of the four-port at position $m = 0$. The two axes give the locations of the two photons, labelled by the integer-valued four-port index. Unlike the Grover matrix case, the amplitudes do not remain clustered. (b) The spatial distribution of the photon amplitudes for two *distinguishable* photons. The result is basically the same as (a). The amplitude spreads across the chain. The photons are indistinguishable, therefore, we cannot distinguish a pair of photon at $m = -5, 5$ and $m = 5, -5$. This indistinguishability allows to add amplitudes coherently.

6.4 State Manipulation Using Clustered Two-Photon Effect

We have investigated localized ballistic clustered two-photon effect itself in the previous section. This effect can be extended to employ state manipulation. For a photon in spatial mode a with horizontally polarized photon is denoted as a_H and horizontally polarized photon in mode b is denoted as b_H. We omit polarization degrees of freedom when identical photons are used through out the system. Consider an analogous setup as Sec. 6.2. Two indistinguishable photons are sent into a four-dimensional multiport device realization of the Grover matrix. The photons are sent from the left side of the system through out this section. The first BS multiport composite system is denoted as subscript 0 and the other half is denoted as subscript 1. The result differs depending on the input location of photons. Consider a system consisting of two multiports and two beam splitters. There are several ways to insert photons in the system, however we choose two specific ones. To be able to send a photon into the middle of the system, the setup needs to be supplied with circulators, is shown in Fig. 6·5. Another setup requires no circulators to propagate input photons. The photons experience an extra transformation by a beam splitter upon photon entrance. The system is graphically supplied in Fig. 6·6. It needs to be noted that the number of multiports in the system does not change the final outcome. We are using two multiports as an example, however, the result is identical when the system has a single multiport or more than two multiports as long as the devices are assumed to be lossless during the propagation.

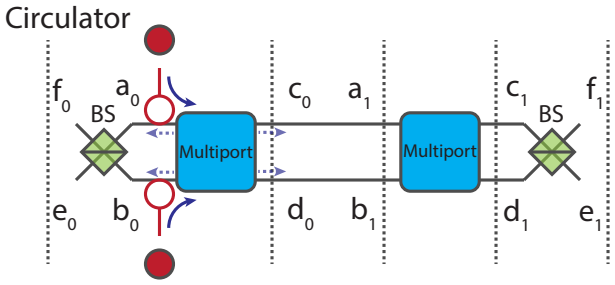

Figure 6·5: A system setup with input photons supplied by circulators. The system consists of two beam splitters, two multiport devices, and two circulators. These circulators allow us to send photons from the left side of the multiport device without experiencing a beam splitter transformation before entering the multiport device. The input state split into right moving and left moving amplitudes (shown as dotted arrows) upon multiport transformation.

6.4.1 Photon Propagation Using Circulators

This method is used to distribute HOM pair between the right and the left side of the system. Recall the transformation from Sec. 6.3.2. The original input state $a_0 b_0$ transforms to:

$$\begin{aligned} a_0 b_0 &\xrightarrow{M} \tfrac{1}{2}(-a_0 + b_0 + c_0 + d_0)\tfrac{1}{2}(a_0 - b_0 + c_0 + d_0) \\ &= -\tfrac{1}{4}(a_0^2 + b_0^2) + \tfrac{1}{2}a_0 b_0 + \tfrac{1}{4}(c_0^2 + d_0^2) + \tfrac{1}{2}c_0 d_0 \\ &= -\tfrac{1}{4}(a_0 - b_0)^2 + \tfrac{1}{4}(c_0 + d_0)^2, \end{aligned} \tag{6.15}$$

where we have used the commutation relation $ab = ba$ since the photons are identical and in different spatial locations. Eq. 6.15 shows that correlated photons are split into right moving $\frac{1}{4}(c_0 + d_0)^2$ and left moving $-\frac{1}{4}(a_0 - b_0)^2$ amplitudes, with no cross terms. This absolute separation of propagation direction without mixing of right moving and left moving amplitudes is important because the photon pairs remain distinctly localized and clustered at each step. The right moving amplitude is translated to $\frac{1}{4}(a_1 + b_1)^2$ and propagates without changing its form. $\frac{1}{4}(a_1 + b_1)^2 \xrightarrow{M} \frac{1}{4}(c_1 + d_1)^2$. The left moving amplitude $-\frac{1}{4}(a_0 - b_0)^2$

stays the same until BS transformation. We use a beam splitter matrix given by,

$$BS_{forward} = \frac{1}{\sqrt{2}} \begin{pmatrix} 1 & 1 \\ -1 & 1 \end{pmatrix}. \tag{6.16}$$

The matrix transforms the photons coming from mode e_0 and f_0. The photons are transformed in the following way.

$$e_0 \rightarrow \frac{1}{\sqrt{2}}(a_0 - b_0),\ f_0 \rightarrow \frac{1}{\sqrt{2}}(a_0 + b_0). \tag{6.17}$$

Backward propagation follows transpose of the BS matrix,

$$BS_{backward} = \frac{1}{\sqrt{2}} \begin{pmatrix} 1 & -1 \\ 1 & 1 \end{pmatrix}. \tag{6.18}$$

The back propagating photons are transformed in the following way.

$$a_0 \rightarrow \frac{1}{\sqrt{2}}(e_0 + f_0),\ b_0 \rightarrow \frac{1}{\sqrt{2}}(-e_0 + f_0). \tag{6.19}$$

The controlled HOM effect can be observed in higher-dimensional multiports assisted by extra beam splitters. Imagine beam splitters inserted in the system as in Fig. 6·5. Input state ab is now transformed into $-\frac{1}{4}(a-b)^2 + \frac{1}{4}(c+d)^2$ as indicated above, then further transformed by beam splitters to obtain HOM pairs between the right side and left side of the system. The right and left sides of the system each have two output ports. The exit port of the photon pair can be controlled by varying phase shift settings before the beam splitters. A phase shift on the left side of the system does not affect the result of the right side amplitude, and vice versa. This system, having circulators at the beginning of the system, is denoted as transformation pattern I, and the detailed discussions of its transformation are in Sec. 6.5.

6.4.2 Photon Propagation without Circulators

This method allows to redistribute input states between right and left side of the system without changing amplitudes. Consider sending two photons from the left side of the beam

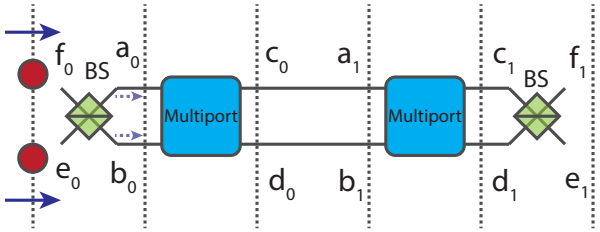

Figure 6·6: System setup without circulators. The input photons are subjected to a beam splitter before they enter the multiport. The input state is transformed and propagated in one direction (shown as dotted arrows). The BS transformed input state is transformed again by the first multiport devices.

splitter as indicated in Fig. 6·6 then transform the output state by the multiport device. We only consider the first multiport transformation here. The rest of the transformation is given in Sec. 6.6.

$$e_0 f_0 \xrightarrow{BS} -\frac{1}{2}(a_0^2 - b_0^2) \xrightarrow{M} -\frac{1}{2}(a_0 - b_0)(c_0 + d_0) \tag{6.20}$$

The final state has cross-terms, and it is different from the case with circulators in a sense that the output state is *coupled*. The state does not provide clear separation between right moving and left moving amplitudes. Even though, the state does not have clear distinction between right moving and left moving, we still refer the amplitudes right and left moving amplitudes unless special attention is required. This system having no circulators is denoted as transformation pattern II, and the detailed discussions of its transformation are in Sec. 6.6

6.5 Transformation Pattern I: Directionally-Controllable HOM Effect in Higher-Dimensional Spatial and Temporal Modes

In this section we discuss the transformation pattern I. The higher dimensional HOM effect is generated by the multiport-based linear optics system with circulators at the inputs. The propagation direction control and delays between amplitudes are discussed in subsections. We use a single multiport device to show the control effect and we introduce two multiport

devices in the system for delayed effect.

6.5.1 Control of Propagation Direction

Given that one two-photon amplitude must exit left and one right, there are four possible combinations of outgoing HOM pairs as indicated in Fig. 6·7. The combinations are, (a): (e_0^2, f_1^2), (b): (f_0^2, f_1^2), (c): (f_0^2, e_1^2), and (d): (e_0^2, f_1^2). This means, in the case of (a) for example, the left-moving two-photon amplitude leaves in mode f, and the right-moving amplitude leaves in mode e. Directional control of the four cases is readily demonstrated, as follows. In case (a) there is only a beam splitter transformation after the multiport, giving

$$\begin{aligned} -\tfrac{1}{4}(a_0 - b_0)^2 &\xrightarrow{BS} -\tfrac{1}{4\sqrt{2}}(e_0 + f_0 + e_0 - f_0)^2 = -\tfrac{1}{2}e_0^2, \\ \tfrac{1}{4}(c_1 + d_1)^2 &\xrightarrow{BS} -\tfrac{1}{4\sqrt{2}}(e_1 + f_1 - e_1 + f_1)^2 = \tfrac{1}{2}f_1^2. \end{aligned} \tag{6.21}$$

The final output state is,

$$\frac{1}{2}(-e_0^2 + f_1^2) = -\frac{1}{\sqrt{2}}(|2,0\rangle_0 + |0,2\rangle_1). \tag{6.22}$$

In case (b), a phase plate is inserted in the lower arm of the left side to switch the exit port from d to c. All the phase shifters P are set to π, therefore transforming $b \to -b$.

$$\begin{aligned} -\tfrac{1}{4}(a-b)^2 + \tfrac{1}{4}(c+d)^2 &\xrightarrow{P} -\tfrac{1}{4}(a+b)^2 + \tfrac{1}{4}(c+d)^2 \\ &\xrightarrow{BS} \tfrac{1}{2}(-f_0^2 + f_1^2) = \tfrac{1}{\sqrt{2}}(-|0,2\rangle_0 + |0,2\rangle_1). \end{aligned} \tag{6.23}$$

Compared to case (a), the exit port is switched from f to e. In (c), phase plates are inserted in the lower arms of both right and left sides. Photons in modes b and d are transformed to $-b$ and $-d$, respectively.

$$\begin{aligned} -\tfrac{1}{4}(a-b)^2 + \tfrac{1}{4}(c+d)^2 &\xrightarrow{P} -\tfrac{1}{4}(a+b)^2 + \tfrac{1}{4}(c-d)^2 \\ &\xrightarrow{BS} \tfrac{1}{2}(-f_0^2 + e_1^2) = \tfrac{1}{\sqrt{2}}(-|0,2\rangle_0 + |2,0\rangle_1). \end{aligned} \tag{6.24}$$

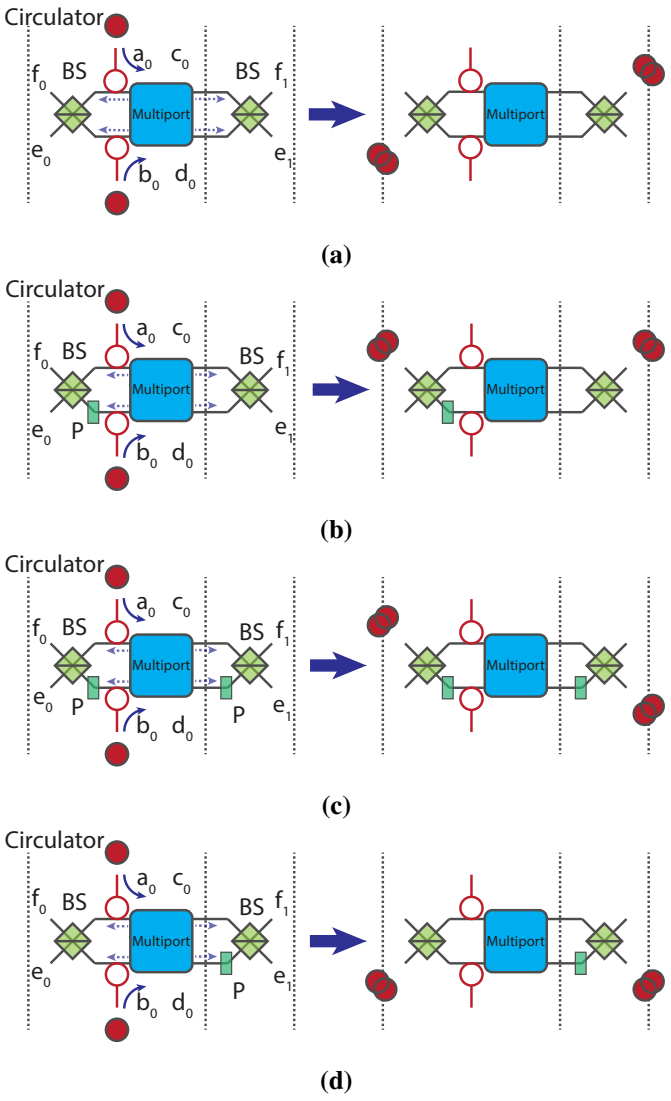

Figure 6·7: Higher dimensional HOM effect with directional control. Correlated photons, $a_0 b_0$, are sent in from the circulators into the first multiport. After the first multiport interaction, the incoming photon pair splits into right-moving and left-moving two-photon amplitudes. The separately-moving amplitudes are bunched at the beam splitters on right and left sides. We can controllably switch between four different output sites, and where the clustered output photons appear depends on the location of the phase shifter P. In (a), no phase plates are introduced, and the output biphoton amplitudes leave f_0 and e_1. The final state is $\frac{1}{\sqrt{2}}(-|2,0\rangle_0 + |0,2\rangle_1)$, meaning superposition of two photons in mode e_0 and two in mode f_1. In case (b), the phase shifter $P = \pi$ is to the left, changing the relative phase between upper and lower arms. Similarly in (c) and (d), other locations for the phase shifters cause biphotons to leave in other spatial modes.

In (d), a phase plate is inserted in the lower arm of the right side. A photon in mode d is transformed to $-d$.

$$\begin{aligned} -\tfrac{1}{4}(a-b)^2+\tfrac{1}{4}(c+d)^2 &\xrightarrow{P} -\tfrac{1}{4}(a-b)^2+\tfrac{1}{4}(c-d)^2 \\ &\xrightarrow{BS} \tfrac{1}{2}(-e_0^2+e_1^2)=\tfrac{1}{\sqrt{2}}(-|2,0\rangle_0+|2,0\rangle_1). \end{aligned} \tag{6.25}$$

This demonstrates complete directional control of biphoton propagation direction using only linear optical devices. Directional control does not require changing splitting ratios at each linear optical device (BS and multiport), and occurs in a lossless manner since no post-selection is required.

6.5.2 Delayed HOM effect

Delayed HOM Effect without Reflection

We introduce a phase shifter between two multiports as in Fig. 6·8 (b). Without the phase plate between two multiport devices, the photons behave exactly the same as in the previous subsection. However, the phase shifter can change propagation direction of right moving amplitude to the left. This reflection results in detecting HOM pairs only on the left side, but with some delay between the two exiting amplitudes. We start with the case without the phase shifter. The photon insertion is the same as the previous case, coming from the left side of the first multiport.

$$\begin{aligned} a_0 b_{0R} &\xrightarrow{M} -\tfrac{1}{4}(a_0-b_0)_L^2+\tfrac{1}{4}(c_0+d_0)_R^2 \xrightarrow{T+BS,\ T} -\tfrac{1}{2}e_{0L}^2+\tfrac{1}{4}(a_1+b_1)_R^2 \\ &\xrightarrow{M} -\tfrac{1}{2}f_{0L}^2+\tfrac{1}{4}(c_1+d_1)_R^2 \xrightarrow{BS} -\tfrac{1}{2}e_{0L}^2+\tfrac{1}{2}f_{1R}^2, \end{aligned} \tag{6.26}$$

where M, T, BS represents multiport, translation and beam splitter transformation respectively. We use subscript R and L to illustrate amplitudes propagating to the right or left. T translates a photon amplitude by a single time step (for example, $\frac{1}{4}(c_0+d_0)^2 \to \frac{1}{4}(a_1+b_1)^2$). The second transformation $T+BS$, T is read as applying $T+BS$ on the first term and T on

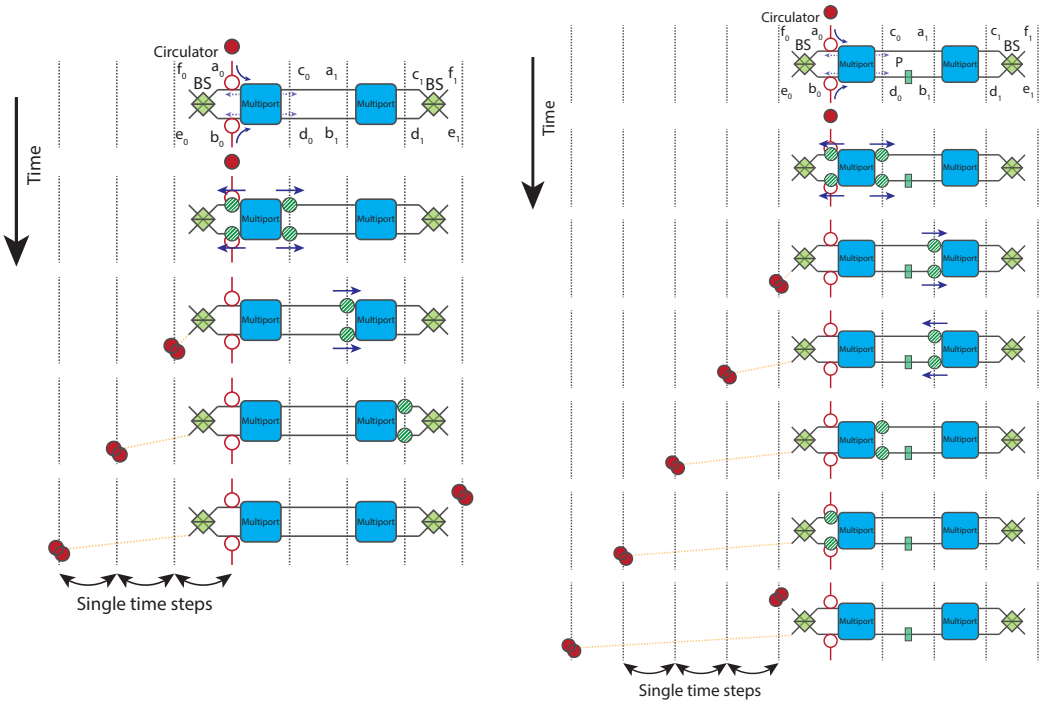

(a) Delayed HOM effect without reflection

(b) Delayed HOM effect with reflection

Figure 6·8: Delayed HOM effect. The two-photon amplitude transformation progresses in time from top to bottom. The distance traveled in a single time step is indicated by vertical dashed lines. The original photons as well as photons in the target state are indicated using red circles. The green striped circles indicate intermediate transformed state. The total number of photons are always two through out the transformations. (a) Two multiports and beam splitters *without* phase shifters between the multiports. In the first step, the behavior is the same as for a single multiport with beam splitters. The right-moving amplitude propagates through the second multiport, and left-moving amplitude propagates through the beam splitter. The right moving amplitude is delayed by one additional multiport transformation before a two-photon observation probability will become available in spatial modes on the right. (b) Two multiports and beam splitters *with* a phase shifter P set at π between multiports. When the P is present, the right-moving amplitude gains a relative phase between modes a_1 and b_1. Reflection occurs at the multiport when the relative phase between the two is π. Therefore, the transformed amplitude reflects upon a second multiport encounter, going back to the original state with opposite propagation direction. Reflection does not occur on this transformed left-moving amplitude, therefore it continues to propagate leftward. The original left-moving amplitude becomes available for detection earlier than the transformed left-moving amplitude.

the second term.

The final state is,

$$-\frac{1}{2}e_{0L}^2+\frac{1}{2}f_{1R}^2=-\frac{1}{\sqrt{2}}(|2,0\rangle_{0T_0L}-|0,2\rangle_{1T_1R}), \tag{6.27}$$

where T_0 is the time when the first biphoton amplitude leaves the system and T_1 is the exit time of the second. The right moving amplitude stays in the system longer than the left moving amplitude because of the extra multiport device in the system, leading to time delay $\Delta T = T_1 - T_0$.

Delayed HOM Effect with Reflection

When a π-phase shifter is inserted on one path between the multiports, the right-moving amplitude gets reflected upon the second multiport encounter. Instead of having two-photon amplitudes on the right and left sides of the system, both photon amplitudes end up leaving from the left. The HOM effect still occurs but now with some delay between the two amplitudes at the end of the BS. This is indicated in Fig. 6·8 (b).

$$a_0b_{0R}\xrightarrow{M}-\tfrac{1}{4}(a_0-b_0)_L^2+\tfrac{1}{4}(c_0+d_0)_R^2\xrightarrow{T+BS,\ T+P}-\tfrac{1}{2}e_{0L}^2+\tfrac{1}{4}(a_1-b_1)_R^2. \tag{6.28}$$

The second transformation $T+BS$, $T+P$ is read as applying $T+BS$ on the first term and $T+P$ on the second term. Left-moving photons leave before right-moving photons.

$$\xrightarrow{M}\quad\tfrac{1}{4}(a_1-b_1)_L^2\xrightarrow{P+T}\tfrac{1}{4}(c_0+d_0)_L^2\xrightarrow{M}\tfrac{1}{4}(a_0+b_0)_L^2\xrightarrow{BS}\tfrac{1}{2}f_{0L}^2. \tag{6.29}$$

The final state,

$$-\frac{1}{2}e_{0L}^2+\frac{1}{2}f_{0L}^2=-\frac{1}{\sqrt{2}}(|2,0\rangle_{0T_0L}-|0,2\rangle_{0T_2L}), \tag{6.30}$$

is now two HOM pair amplitudes, both on the left side of the system, at output ports e_0 and f_0, with some time delay $\Delta T = T_2 - T_0$ between them. The first amplitude leaves port e_0 at T_0, then the second leaves f_0 and the time labeled T_2.

6.6 Transformation Pattern II: State Redistribution in Higher-Dimensional Spatial and Temporal Modes

6.6.1 State Transformation and Propagation

We have considered the case where the input photon state is transformed by the multiport device right after photon insertion in the previous section. Instead of using circulators, we can transform the input state by the BS in advance and then transform the state by using the multiport device. Though the Grover matrix spreads the input state equally in four directions, the end result preserves the original form of the input state. We demonstrate a state redistribution property using distinguishable and indistinguishable photons, meaning the input state gets redistributed between right and left side without changing amplitudes. The propagation result is different from the previous case. Consider sending two indistinguishable photons in the system. The input two photons have the same polarization to make them indistinguishable. The input photons are inserted from the left side of the beam splitter. The beam splitter transforms the input state and propagates from the left side to right side of the device without any reflections. The amplitudes are transformed by the multiport device after the beam splitter transformation. This transformation splits input photons into coupled right-moving and left-moving amplitudes. The coupled left moving amplitudes reflected from the first multiport counter propagates and transformed by the first beam splitter from the right to the left. The right moving amplitude is transmitted without changes in amplitude. This amplitude gets transmitted by the right side beam splitter at the end.

Indistinguishable Photons

We examine the mathematical details on indistinguishable photons in the system without circulators first. We consider three cases by sending photons in spatial modes e and f. First,

we consider indistinguishable a pair of single photons from spatial mode e and f.

$$e_{H0}f_{H0} \xrightarrow{BS} -\frac{1}{2}(a_{H0}^2 - b_{H0}^2) \xrightarrow{M} -\frac{1}{2}(a_{H0} - b_{H0})(c_{H0} + d_{H0}) \xrightarrow{BS} -e_{H0}f_{H1}. \quad (6.31)$$

HOM state with relative phase between two amplitudes equal to +1 is considered here.

$$\begin{aligned} &\tfrac{1}{2}(e_{H0}^2 + f_{H0}^2) \xrightarrow{BS} \tfrac{1}{2}(a_{H0}^2 + b_{H0}^2) \\ &\xrightarrow{M} \tfrac{1}{4}(a_{H0} - b_{H0})^2 + \tfrac{1}{4}(c_{H0} + d_{H0})^2 \xrightarrow{BS} \tfrac{1}{2}(e_{H0}^2 + f_{H1}^2). \end{aligned} \quad (6.32)$$

The input state is redistributed in a sense that one amplitude is on the right side of the system and the other amplitude is on the left side while maintaining the original structure of the state.

HOM state with relative phase between two amplitudes equal to -1 is considered here.

$$\begin{aligned} &\tfrac{1}{2}(e_{H0}^2 - f_{H0}^2) \xrightarrow{BS} -a_{H0}b_{H0} \\ &\xrightarrow{M} \tfrac{1}{4}(a_{H0} - b_{H0})^2 - \tfrac{1}{4}(c_{H0} + d_{H0})^2 \xrightarrow{BS} \tfrac{1}{2}(e_{H0}^2 - f_{H1}^2). \end{aligned} \quad (6.33)$$

In both cases, the output state is identical to the input state except for the spatial modes.

Distinguishable Photons

Now, we examine the case of distinguishable two photon input. The procedure is identical to the the previous case. We begin with two distinguishable photons at each modes without superposition.

$$\begin{aligned} &e_{H0}f_{V1} \xrightarrow{BS} \tfrac{1}{2}(a_{H0} - b_{H0})(a_{V0} + b_{V0}) \\ &\xrightarrow{M} -\tfrac{1}{2}(a_{H0} - b_{H0})(c_{V0} + d_{V0}) \xrightarrow{BS} -e_{H0}f_{V1}. \end{aligned} \quad (6.34)$$

We look at the case of HOM states.

$$\begin{aligned}&\tfrac{1}{2}(e_{H0}^2 \pm f_{V0}^2) \xrightarrow{BS} \tfrac{1}{4}(a_{H0}-b_{H0})^2 \pm \tfrac{1}{4}(a_{V0}+b_{H0})^2 \\ &\xrightarrow{M} \tfrac{1}{4}(a_{H0}-b_{H0})^2 \pm \tfrac{1}{4}(c_{V0}+d_{H0})^2 \xrightarrow{BS} \tfrac{1}{2}(e_{H0}^2 \pm f_{V1}^2).\end{aligned} \tag{6.35}$$

The control of exit location can be performed as well in this scheme by introducing phase shifters in the system as indicated in Fig. 6·9. This procedure does not destroy the redistribution property. There are four potential spatial modes and by switching the phase shift before beam splitters, the direction of propagation switches. The combinations are, (a): $(e_0, f_0) \to (e_0, f_1)$, (b): $(e_0, f_0) \to (f_0, f_1)$, (c): $(e_0, f_0) \to (e_0, f_1)$, and (d): $(e_0, f_0) \to (e_0, e_1)$.

The result from the system with circulators is summarized in Table. 6.1, the system without them is in Table. 6.2. In the case of indistinguishable photons, the results are cyclic in a sense that all three states can be produced by using the other system. However, there is a significant difference when distinguishable photons are considered.

6.6.2 Delayed State Redistribution

We introduce the temporal delay effect as the higher dimensional HOM case by introducing a phase shifter between two multiports.

Without Reflection

When there is no phase shifter between the two multiports, the result is identical to the system with a single multiport from the previous section. The state transformation and propagation is provided schematically in Fig. 6·10 (a). The photons are initially sent from the left side of the BS. The correlated photons are transformed to HOM state through the BS.

$$e_0 f_{0R} \xrightarrow{BS} \frac{1}{2}(a_0^2 - b_0^2)_R \xrightarrow{M} -\frac{1}{2}(a_0 - b_0)_L (c_0 + d_0)_R. \tag{6.36}$$

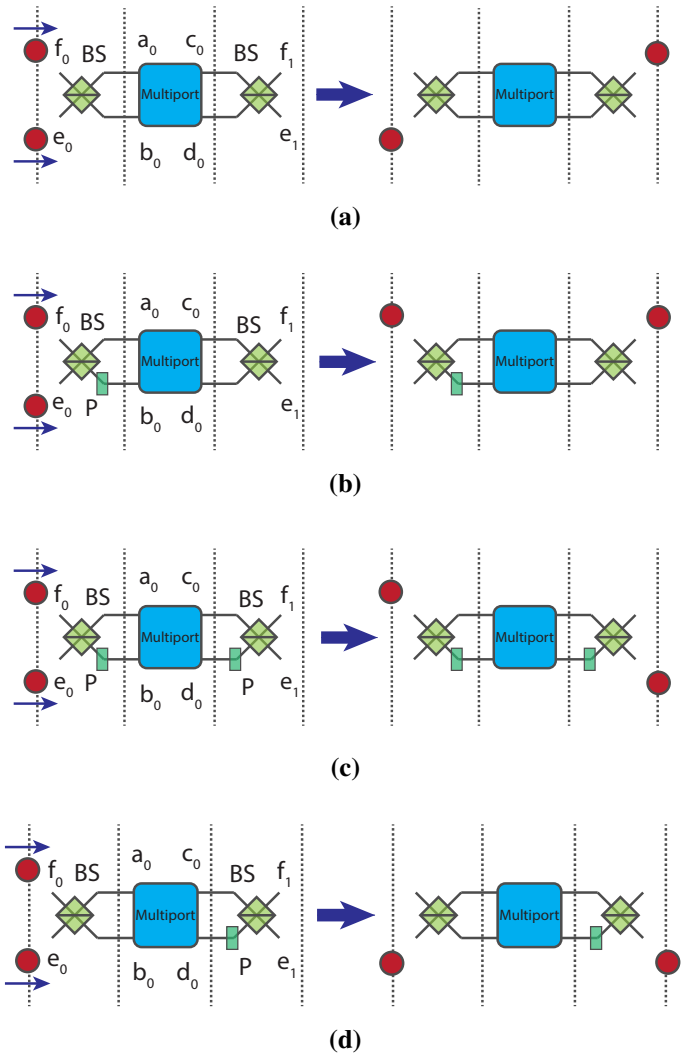

Figure 6·9: Quantum state redistribution with control of propagation direction. We performed the same analysis as the higher dimensional HOM effect with direction control. By introducing phase shifters in the system before beam splitters, we can change the exit direction of the amplitudes. The starting state is $e_0 f_0$. The first beam splitter transforms the input state, then they enter the multiport device. The multiport transformed state goes through beam splitters on the right and left side. The final outcome has the same form as the input state.

State transformation with circulators	
Indistinguishable photons	$a_{H0}b_{H0} \rightarrow -\frac{1}{2}(e_{H0}^2 - e_{H1}^2)$
HOM pair with +1 relative phase	$\frac{1}{2}(a_{H0}^2 + b_{H0}^2) \rightarrow \frac{1}{2}(e_{H0}^2 + f_{H1}^2)$
HOM pair with -1 relative phase	$\frac{1}{2}(a_{H0}^2 - b_{H0}^2) \rightarrow e_{H0}f_{H1}$
Distinguishable photons	$a_{H0}b_{V0} \rightarrow -\frac{1}{2}(e_{H0} - f_{H1})(e_{V0} + f_{V1})$
Distinguishable HOM pair	$\frac{1}{2}(a_{H0}^2 \pm b_{V0}^2) \rightarrow \frac{1}{4}\{(e_{H0} - f_{H1})^2 \pm (e_{V0} - f_{V1})^2\}$

Table 6.1: State transformations in a system with circulators. The first three states deal with indistinguishable photons by giving them the same polarization. A state consisting of two single photons will become an HOM state. We analyzed HOM states as an initial state, and they become either the HOM state or a two single-photon state. Distinguishable photons are also analyzed by introducing orthogonal polarizations. The output states become coupled states meaning the original states are not preserved.

State transformation without circulators	
Indistinguishable photons	$e_{H0}f_{H0} \rightarrow e_{H0}f_{H1}$
HOM pair with +1 relative phase	$\frac{1}{2}(e_{H0}^2 + f_{H0}^2) \rightarrow \frac{1}{2}(e_{H0}^2 + f_{H1}^2)$
HOM pair with -1 relative phase	$\frac{1}{2}(e_{H0}^2 - f_{H0}^2) \rightarrow \frac{1}{2}(e_{H0}^2 - f_{H1}^2)$
Distinguishable photons	$e_{H0}f_{V0} \rightarrow e_{H0}f_{V1}$
Distinguishable HOM pair	$\frac{1}{2}(e_{H0}^2 \pm f_{V0}^2) \rightarrow \frac{1}{2}(e_{H0}^2 \pm f_{V1}^2)$

Table 6.2: State transformations in a system without circulators. The structure of the table is the same as Table. 6.1. The first three states deal with indistinguishable photons by giving them the same polarization. The last two states handle distinguishable photons. The output states preserve the same form as the input state. We start the transformation from the system location 0, then the transformed states are redistributed between location 0 and location 1. The result shows coherent transportation of input states.

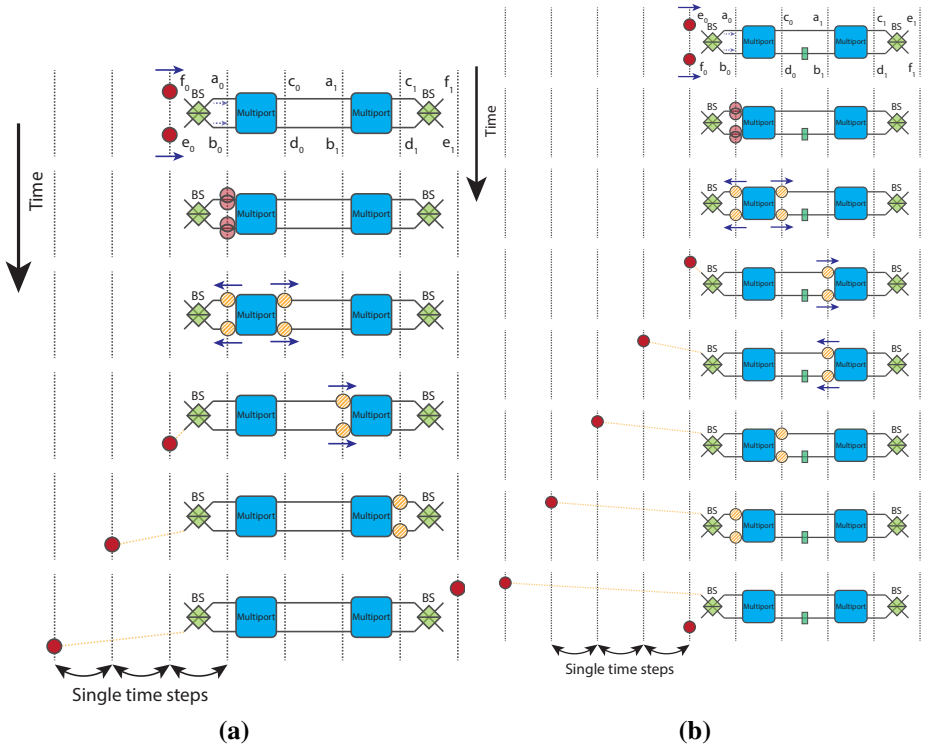

Figure 6·10: Delayed state redistribution. The two-photon amplitude transformation progresses in time from top to bottom. The distance traveled in a single time step is indicated by vertical dashed lines. The total photon numbers are two in the system through out the propagation. At the first step for both cases, the input two-photon state is transformed by the BS. The transformed state becomes the HOM state, and it is indicated as red transparent overlapped circles occupying both modes. The initial and the final transformed state are indicated using solid red circles, and intermediate states are indicated in striped yellow circles. (a) Two multiports and beam splitters *without* phase shifters between the multiports. The HOM state enters the multiport and transformed taking the form of $-\frac{1}{2}(a_0 - b_0)(c_0 + d_0)$. The amplitudes are coupled, however, they propagate without changing its amplitude. After several steps, the amplitudes occupying two rails converges to a single mode state after transformation by beam splitters. The final state has the same form as the input state. (b) Two multiports and beam splitters *with* a phase shifter P set at π between multiports. When the P is present, the right-moving coupled amplitude gains a relative phase between modes a_1 and b_1. Reflection occurs at the multiport when the relative phase between the two is π. Therefore, the transformed amplitude reflects upon a second multiport encounter, going back to the original state. Reflection does not occur on this transformed coupled left-moving amplitude, therefore it continues to propagate leftward. The original left-moving amplitude becomes available for detection earlier than the transformed left-moving amplitude.

The HOM state is transformed by the multiport device. This state is in a coupled state because right moving and left moving amplitudes are not separated. We propagate this state through the BS on the left and translate the amplitudes moving to the right.

$$\xrightarrow{BS,T} -\frac{1}{\sqrt{2}}e_{0L}(a_1+b_1)_R \xrightarrow{M} -\frac{1}{\sqrt{2}}e_{0L}(c_1+d_1)_R \xrightarrow{BS} -e_{0T_0L}f_{1T_1R} \tag{6.37}$$

The left moving amplitude is transformed by the left BS while right moving amplitude propagates to the second multiport device. We introduced temporal difference between the right moving and the left moving photons.

With Reflection

Reflection of amplitudes are introduced when there is a phase shifter between two multiport devices as indicated in fig. 6·10 (b).

$$\begin{aligned} e_0 f_{0R} \xrightarrow{BS} \tfrac{1}{2}(a_0^2-b_0^2)_R \xrightarrow{M} -\tfrac{1}{2}(a_0-b_0)_L(c_0+d_0)_R \\ \xrightarrow{BS,T+P} -\tfrac{1}{\sqrt{2}}e_{0L}(a_1-b_1)_R \end{aligned} \tag{6.38}$$

The right moving amplitude gains relative phase between upper and lower rails, and this relative phase allows the amplitude to get reflected upon multiport encounter.

$$\begin{aligned} \xrightarrow{M} -\tfrac{1}{\sqrt{2}}e_{0L}(a_1-b_1)_L \xrightarrow{T+P} -\tfrac{1}{\sqrt{2}}e_{0L}(c_0+d_0)_L \\ \xrightarrow{M} -\tfrac{1}{\sqrt{2}}e_{0L}(a_0+b_0)_L \xrightarrow{BS} -e_{0T_0L}f_{0T_2L} \end{aligned} \tag{6.39}$$

The input photons do not have any delays between the two at the beginning. The delay $\Delta T = T_2 - T_0$ is introduced from the reflection in the system.

6.7 Controllable Entangled-Photon State Distribution

The experimental setup illustrating the operation of the central unit in the proposed network, the MCU, on a polarization-entangled state is illustrated in Fig. 6·11. Throughout this paper, the figure-eight shape shown in this diagram will be used to denote entanglement between the enclosed pair of photons. The MCU will be used as a building block to enable distribution of two-photon entanglement as well as multi-photon entangled states among any desired spatial modes. In the case of an entangled-photon pair, photons enter at e_0 and f_0 and propagate towards the right (see Fig. 6·11 left).

6.7.1 Manipulation of Entangled Two-Photon States

We analyze the distribution of two-photon entangled Bell states exploiting polarization degrees of freedom. Initially, the input polarization-entangled state is transformed by a beam splitter; then the transformed input state is processed by the multiport. The multiport splits the input state into right-moving and left-moving amplitudes confined to a two-rail waveguided path (striped orange circles in Fig. 6·12).

We introduce polarization-entangled Bell states in both bra-ket and creation operator notation. We use the simplified notation for creation operators by removing hat and dagger symbols. The creation operators are always acting on vacuum state $|0\rangle$, therefore, we often omit writing the vacuum states out explicitly.

$$\begin{aligned} |\psi^{\pm}\rangle &= \frac{1}{\sqrt{2}}(|H\rangle_0|V\rangle_0 \pm |V\rangle_0|H\rangle_0) \\ &= \frac{1}{\sqrt{2}}(e_{H0}f_{V0} \pm e_{V0}f_{H0})|0\rangle, \qquad (6.40) \\ |\phi^{\pm}\rangle &= \frac{1}{\sqrt{2}}(|H\rangle_0|H\rangle_0 \pm |V\rangle_0|V\rangle_0) \\ &= \frac{1}{\sqrt{2}}(e_{H0}f_{H0} \pm e_{V0}f_{V0})|0\rangle. \qquad (6.41) \end{aligned}$$

Initially, the Bell states are transformed by a beam splitter so that their amplitudes are

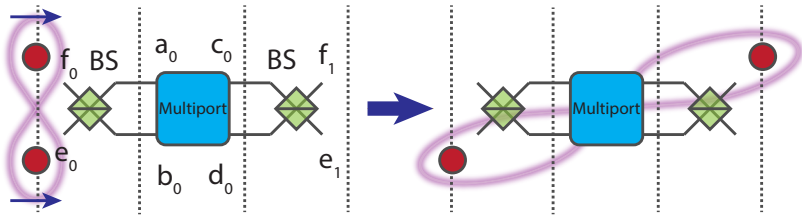

Figure 6·11: Entanglement distribution in a multiport unit. Two polarization-entangled photons occupying spatial modes e_0 and f_0 are inserted with the propagation direction to the right. The photons leave through different ports e_0 and f_1 after the linear-optical transformation at the multiport unit and sustain their polarization entanglement. The figure-eight shape is used here and throughout the rest of the paper to show entanglement between pairs of photons.

spread between two spatial waveguides:

$$|\phi^{\pm}\rangle \xrightarrow{BS} \frac{1}{2\sqrt{2}}({a_{H0}}^2 \pm {a_{V0}}^2 - {b_{H0}}^2 \mp {b_{V0}}^2)\,|0\rangle\,, \tag{6.42}$$

$$|\psi^{+}\rangle \xrightarrow{BS} \frac{1}{\sqrt{2}}(a_{H0}a_{V0} - b_{H0}b_{V0})\,|0\rangle\,, \tag{6.43}$$

$$|\psi^{-}\rangle \xrightarrow{BS} \frac{1}{\sqrt{2}}(a_{H0}b_{V0} - a_{V0}b_{H0})\,|0\rangle\,. \tag{6.44}$$

Then two input state amplitudes occupying spatial modes a_0 and b_0 enter the Grover multiport from the left and get distributed between the right side and left side of the multiport without any losses in the system. The final amplitude transformation is performed by two beam-splitters on either side of the Grover multiport. A detailed description of the quantum amplitude transformation at the beam splitter and at the Grover multiport could be found in (Osawa et al., 2020). We provide detailed calculation on the transformation of $|\phi^{+}\rangle$.

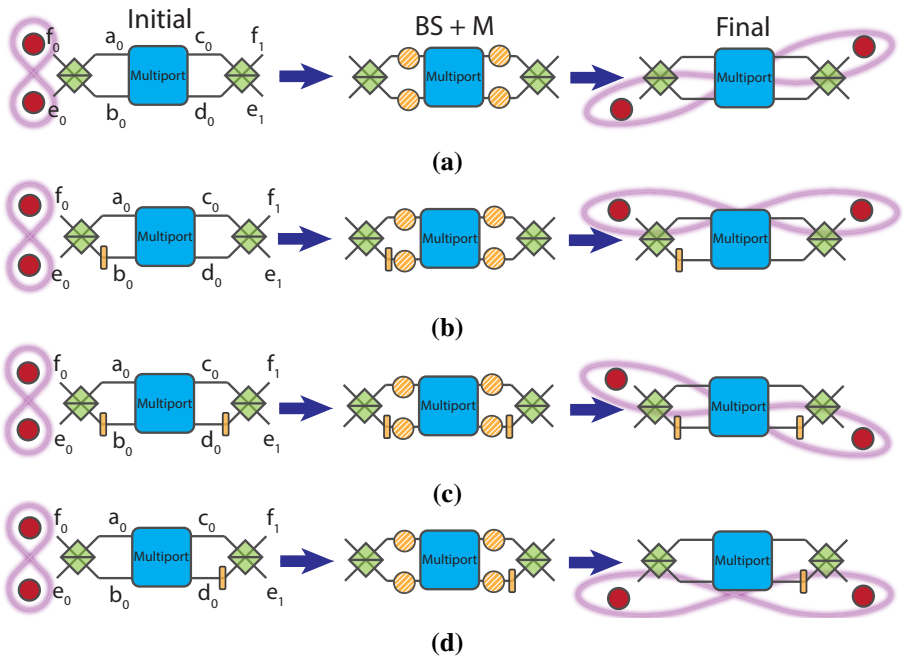

Figure 6·12: Entangled photon exit amplitude control. The input photons enter from ports e_0 and f_0. Depending on the placement of the phase shifters, the photon pair could emerge at four different spatial modes.

$$
\begin{aligned}
|\phi^+\rangle \xrightarrow{BS} & \frac{1}{2\sqrt{2}}(a_{H0}^2 + a_{V0}^2 - b_{H0}^2 - b_{V0}^2)\,|0\rangle \\
\xrightarrow{M} & -\frac{1}{2\sqrt{2}}((a_{H0} - b_{H0})(c_{H0} + d_{H0}) \\
& \quad +(a_{V0} - b_{V0})(c_{V0} + d_{V0}))\,|0\rangle \\
\xrightarrow{BS} & -\frac{1}{\sqrt{2}}(e_{H0}f_{H1} + e_{V0}f_{V1})\,|0\rangle
\end{aligned}
\tag{6.45}
$$

The original input entanglement between e_0 and f_0 modes is now redistributed between two modes e_0 and f_1. These new modes become entangled as a result of the multiport-based control unit (MCU) action. Such a distribution feature is valid for all four polarization Bell states and can be demonstrated by engaging the same quantum amplitude transformation

procedure.

$$\begin{aligned} |\phi^-\rangle &\xrightarrow{MCU} \frac{1}{\sqrt{2}}(e_{H0}f_{H1} - e_{V0}f_{V1})\,|0\rangle\,, \\ |\psi^\pm\rangle &\xrightarrow{MCU} \frac{1}{\sqrt{2}}(e_{H0}f_{V1} \pm e_{V0}f_{H1})\,|0\rangle\,. \end{aligned} \tag{6.46}$$

6.7.2 Control of Exit Modes

The final spatial location of exit photons belonging to the same entangled pair after their manipulation by the linear-optical multiport unit could be controlled by imposing a π phase shift denoted as P on a particular communication waveguide (Osawa et al., 2020). This enables one to control the propagation of entangled state amplitudes and guides its energy to the desired network nodes.

Consider $|\phi^+\rangle$ Bell state again and the state is introduced in the multiport unit from the left at $e_0 f_0$ ports. The input output relationship is give in Fig. 6·12 (a). We show the propagation amplitude can be changed by introducing the π phase shift (P) on the right side of the multiport unit indicated in Fig. 6·12 (d).

$$\begin{aligned} & |\phi^+\rangle = \tfrac{1}{\sqrt{2}}(e_{H0}f_{H0} + e_{V0}f_{V0})\,|0\rangle \\ \xrightarrow{BS+M} \quad & -\tfrac{1}{2\sqrt{2}}((a_{H0} - b_{H0})(c_{H0} + d_{H0}) \\ & +(a_{V0} - b_{V0})(c_{V0} + d_{V0}))\,|0\rangle\,. \end{aligned} \tag{6.47}$$

This state is now a superposition illustrating coupled right-moving and left-moving amplitudes. Each term is transformed once more by the final beam splitter interaction,

$$(a_0 - b_0) \xrightarrow{BS} e_0, \tag{6.48}$$

$$(a_0 + b_0) \xrightarrow{BS} f_0, \tag{6.49}$$

$$(c_0 - d_0) \xrightarrow{BS} e_1, \tag{6.50}$$

$$(c_0 + d_0) \xrightarrow{BS} f_1. \tag{6.51}$$

We dropped scaling coefficients since they are irrelevant for this discussion of relative phase effects.

If the relative phase between the two rails on both sides of the multiport is positive, as in Eq. 6.49 and Eq. 6.51, then both photons leave the unit at ports f. Similarly, if the relative phase between the two rails on both sides of the multiport is negative, as in Eq. 6.48 and Eq. 6.50, then both photons leave at ports e. We can establish the following correspondence between the phase shifts between upper and lower rails on a particular part of the multiport (left phase, right phase) and exit ports for a particular portion of the entangled state:

$$(+,+) = (f_0, f_1), \qquad (+,-) = (f_0, e_1), \tag{6.52}$$

$$(-,+) = (e_0, f_1), \qquad (-,-) = (e_0, e_1). \tag{6.53}$$

The choice of phase shifts therefore provides complete control over the output distribution of the entangled state spatial modes.

We take the final line of Eq. 6.47 and obtain a state $|\xi\rangle$ amplitude distribution prior to encountering final beam splitters,

$$\begin{aligned} |\xi\rangle \equiv -\frac{1}{2\sqrt{2}}((a_{H0} - b_{H0})(c_{H0} + d_{H0}) \\ +(a_{V0} - b_{V0})(c_{V0} + d_{V0}))\,|0\rangle \end{aligned} \tag{6.54}$$

Eq. 6.54 has a form of (-,+) for the first term, and (-,+) for the second term. The final BS transformation on both sides provides

$$|\xi\rangle \xrightarrow{BS} \frac{1}{\sqrt{2}}(e_{H0} f_{H1} + e_{V0} f_{V1})\,|0\rangle\,. \tag{6.55}$$

A phase shift in the right side (see Fig. 6·12 (d)) can alter Eq. 6.54 from (-,+) to (-,-) for the first term and from (-,+) to (-,-) for the second term thus resulting in entangled quantum amplitudes exiting from different ports of the apparatus. The result after the phase alteration

is

$$|\xi\rangle \xrightarrow{P+BS} \frac{1}{\sqrt{2}}(e_{H0}e_{H1} + e_{V0}e_{V1})\,|0\rangle\,. \tag{6.56}$$

In other words, the exiting photon in spatial mode f_{H1} is switched now to the mode e_{H1} and f_{V1} is switched with e_{V1}. The result indicates we can actively redirect the quantum amplitude propagation direction without disturbing the entanglement.

6.8 Scalability of Entangled-State Distribution Network

To further increase the number of spatial modes, we can link several multiport-based control units together. A network could be composed of several units of the type previously discussed, each encompassing two beam splitters and a multiport device, possibly with phase shifters. Such units can be arranged in a network structure by connecting their ports using on-chip waveguides or by fiber links when it is desirable to cover longer distances. A schematic setup in Fig. 6·13 illustrates the two-photon quantum-entangled state transportation between 8 user nodes (16 modes) using multiport units. For the illustration purpose, this network is separated into five sections. C, UL, BL, UR, and BR are central upper left, bottom left, upper right, and bottom right multiport unit locations, respectively.

A two-photon entangled state is introduced from the left side into the central network portion using optical isolators.

$$\begin{aligned} e_{0C}f_{0C} &\xrightarrow{BS} -\frac{1}{2}(a_{0C}^2 - b_{0C}^2) \\ &\xrightarrow{M} -\frac{1}{2}(a_{0C} - b_{0C})(c_{0C} + d_{0C}) \\ &\xrightarrow{BS} e_{0C}f_{1C} \end{aligned} \tag{6.57}$$

This equation illustrates a two-photon state distribution between spatial modes at the end of the central part of the system action. Such transformed photons are now entering the bottom

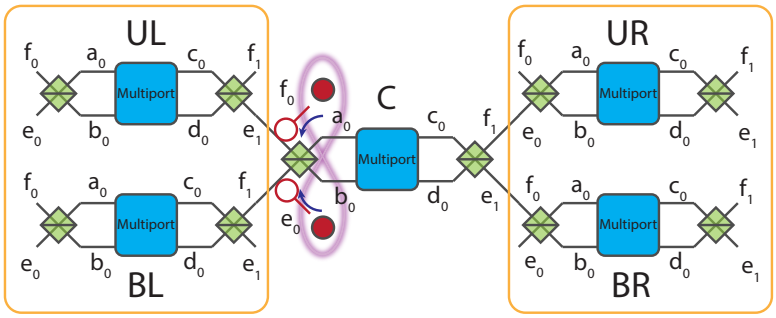

(a) Network schematic and initial conditions

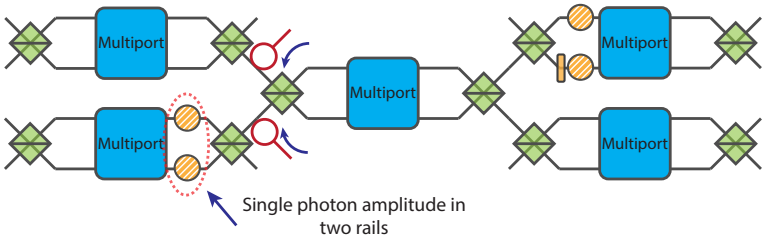

(b) Quantum amplitude propagation after the first round of multiport transformation

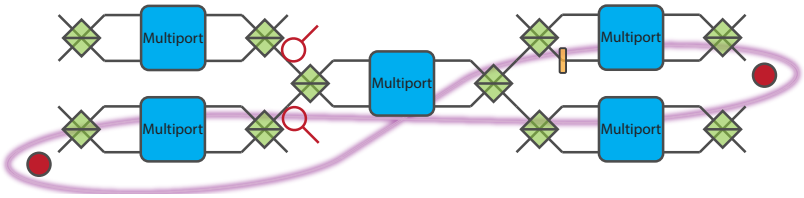

(c) Final outcome for the two-photon entanglement propagation through the network structure

Figure 6·13: Two-photon entanglement distribution in a network. (a) The network consists of five multiport-based units. Entangled photons are inserted at the central unit C. After the transformation in the first multiport unit, the photons are propagated farther to the second layer of the network. (b) Second layer of the network. The photons leaving C enter UL and BR units in this case and get transformed by beam splitters. The two-photon amplitudes (yellow striped circles) travel through the second layer of multiport devices. (c) Quantum amplitudes are transformed again by final beam splitters resulting in the distribution of the original entangled state energy between the right and left side of the system.

left and the upper right second layer units because e_{0C} is propagating to the left and f_{1C} is propagating to the right.

$$\begin{aligned} &\xrightarrow{BS} && \frac{1}{2}(c_{0UL}+d_{0UL})(a_{0BR}-b_{0BR}) \\ &\xrightarrow{P+M} && \frac{1}{2}(a_{0UL}+b_{0UL})(c_{0BR}+d_{0BR}) \\ &\xrightarrow{BS} && e_{0UL}e_{1BR}. \end{aligned} \tag{6.58}$$

e_{0C} indicates a photon in the central multiport region occupying spatial mode e_0. Subscripts UL, BL, UR, and BR are given for appropriate creation operators.

The photon propagation direction can be controlled by inserting phase shifters, as described in Sec. 6.7.2. This capability holds for both photon polarizations. The quantum state transformation pattern (photon $\rightarrow$ distributed two-rails amplitudes $\rightarrow$ photon) repeats every time a photon leaves the multiport unit and enters another one. Fig. 6·13 illustrates the transition of the two-photon state energy from the central multiport to the bottom left and top right multiports (Fig. 6·13 (c)). The form of the quantum state is preserved along its propagation, and the entanglement distribution between any of the two exit locations of the entire system can be performed. We can choose any of the four outputs on the right side for the right moving amplitude and any of the four outputs on the left side for the left moving amplitude by utilizing fixed phase shifters.

6.8.1 Entanglement Distribution Control Using Passive Phase Shifters

The network scalability is illustrated in Fig. 6·14 by a three-layered configuration of multiport units. We can impose additional control to direct entangled photons towards specific outgoing spatial modes in the network by inserting fixed phase shifters at each multiport location.

One specific example of this network operation is provided in Fig. 6·14. After leaving the first multiport unit, the photon enters the next multiport unit either from the top side

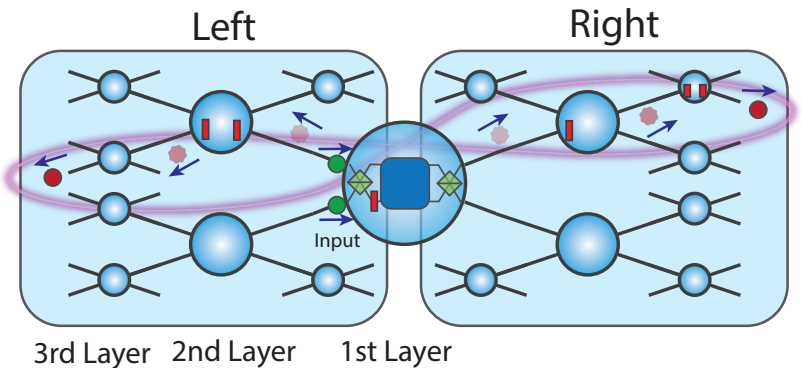

Figure 6·14: Amplitude control using passive phase shifters. Two photons are sent from the left side of the central multiport device (green circles). The red square in the circle indicates phase shifters embedded in the multiport unit. The phase shifters change the propagation direction in transverse direction as described in Section IIB. The final outgoing photon locations are illustrated by solid red circles. The quantum amplitude distribution during internal transport though the network is shown by faded red circles.

mode or the bottom side mode. When the photon enters from the bottom, the relative phase difference between the two output modes is -1 (a-b). This means that the amplitude is going to be reflected at the second multiport back to the original location if no phase shifter is introduced in the path. The introduction of π phase shift allows the amplitude to keep propagating forward. If the photon enters from the top mode of the beam splitter then, the relative phase remains +1 (a+b), therefore the photon propagates forward without any additional phase shifts.

Let us consider the amplitude evolution on the right side. The detailed discussion of the quantum amplitude propagation control using phase shifts is provided earlier in Sec. 6.7.2. The photon departs the first unit from the bottom side and enters the next unit from the top side of the BS. The transformed amplitude has a negative relative phase, hence the phase must be altered to make sure the photon propagates forward. Then, the propagated amplitude can leave the second layer either from the upper or lower side of the unit depending on the relative phase settings.

Assume that the amplitude leaves the second layer at the upper mode since the photon

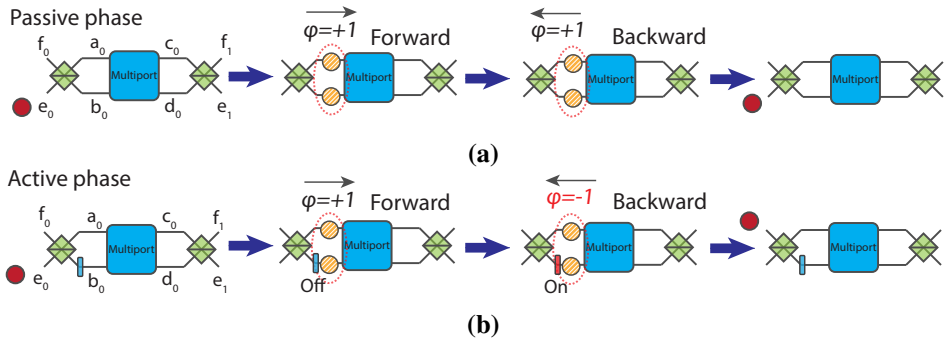

Figure 6·15: Passive and active phase shift altering propagation direction of reflected amplitude. (a) Passive phase shifts. In this case, we do not need to apply any phases therefore there is no phase shifters in the unit. A single photon is entering from the mode e_0. The photon is transformed by the BS into a superposition of forward propagating quantum amplitudes towards the multiport device. Depending on the relative phase shift between the two rails, the amplitude gets either transmitted or reflected at the multiport. The original amplitude transformation done by the input BS for the input mode e has negative relative phase, therefore it will reflect back from the multiport device if one apply zero phase shift (denoted as $\phi = +1$). The second passage through the passive $\phi = +1$ passive phase shifter dictates the photon will exit at the same entrance mode e_0. (b) The active switch of the phase shifter to $\phi = -1$ only for the backward propagating amplitudes changes the relative phase between two rails and switches the outgoing photon energy to the f_0 mode. The active phase shifter allows switching spatial propagation modes $e_0 \rightarrow f_0$ while the passive phase shift only allows a full return $e_0 \rightarrow e_0$. Additional π phase is added to all phase shifters if the photon is entering from the port f_0 and is getting switched to e_0.

has a positive relative phase. The same procedure is repeated at the third layer of multiport units except for the final phase shift. The final phase shift in the third stage is set to guide the photon energy to emerge from the lower outgoing port of the unit. The same procedure applies to the left side amplitude as well.

6.9 Reconfigurable Networks and Controllable Entanglement Distribution

6.9.1 Redirection of Quantum Amplitude Propagation Using Active Phase Shifters

We have described state manipulation methods by using only passive phase shifters up to this point. The passive phase shifter scheme is limited in performance and does not allow for an arbitrary redirection of photons in the multi-user network. Each photon from an entangled pair may independently experience multiport unit transformations while traveling in a complex network. Consider the passive phase shifter based network again (see. Fig. 6·14) and focus on the left side of the network. In the passive network (constant phase shifts), the second layer branches out into four outputs, two in forward direction and two for a backward direction.

When a passive network is used, it is impossible for the input photon to exit from the mode f_0 in order to modify the general propagation path in the network. This makes 20 out of 36 nodes in such passive network unattainable. One must engage active phase shifters (phase shifts that can be controllably changed during the operation of the network) in order to reverse the photon propagation direction from mode e_0 to f_0 as well as from mode f_0 to e_0. A single-photon transformation using active phase shifters is presented that enables a fully reconfigurable network infrastructure.

We focus on the propagation of one part of the two-photon entangled state traveling over the network and its active amplitude manipulation (see Fig. 6·15). A single photon entering port e_0 can leave either at e_0 or f_0 depending on the phase manipulation. We compare the quantum amplitude manipulation using both passive shifts and active shifts.

The system introduces zero forward passive phase shift and zero backward phase shift as indicated in Fig. 6·15 (a). The photon is sent from mode e, therefore there is no need for a phase shift to experience reflection at the multiport device in this case.

This can be seen explicitly by looking at the transformation of the state operators. The

beam splitter transformation on a single photon from mode e_0 is,

$$e_0 \xrightarrow{BS} \frac{1}{\sqrt{2}}(a_0 - b_0). \tag{6.59}$$

The transformed amplitude experiences zero phase shift to keep the relative phase equal to -1.

$$\xrightarrow{P} \frac{1}{\sqrt{2}}(a_0 - b_0). \tag{6.60}$$

The amplitude gets reflected at the multiport device,

$$\xrightarrow{M} \frac{1}{\sqrt{2}}(a_0 - b_0). \tag{6.61}$$

A passive phase shifter cannot change the amount of phase in a time dependent manner, therefore the backward propagation experiences the same amount of phase (zero in this case). Finally, the reflected amplitude is transformed again by the BS resulting in the same location as the initial input location.

$$\xrightarrow{P} \frac{1}{\sqrt{2}}(a_0 - b_0) \xrightarrow{BS} e_0. \tag{6.62}$$

Consider the action of an active phase shifter as provided in Fig. 6·15 (b). Now the system introduces zero phase shift for a forward amplitude and π phase shift after the multiport reflection thus allowing to switch the photon propagation from e_0 to f_0. The first three operations are the same as the passive phase shifter case,

$$e_0 \xrightarrow{BS+P+M} \frac{1}{\sqrt{2}}(a_0 - b_0). \tag{6.63}$$

After the multiport transformation, the exit mode will be different from the input mode if π phase shift is introduced. The time-dependent active phase manipulation is required to

execute different phase shifts.

$$\xrightarrow{P} \frac{1}{\sqrt{2}}(a_0 + b_0) \xrightarrow{BS} f_0. \tag{6.64}$$

The amplitude is redirected to mode f_0 using active phase shifters.

6.9.2 Centralized Network

When passive phase shifters are used, the reflected amplitudes simply propagate back to its original input location. Active phase shifters enable full propagation control of reflected amplitudes as well as transmitted ones.

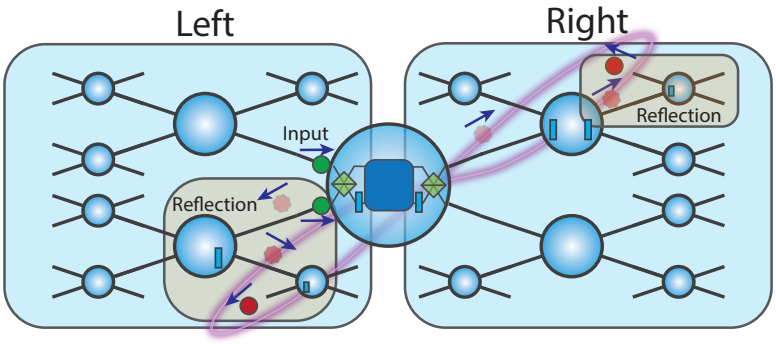

Figure 6·16: Full amplitude distribution control using active phase shifters. Two photons (green circles) are inserted from the left side of the multiport device. The blue square in the circle indicates active phase shifters embedded in the unit. The time-dependent phase shifters change the propagation direction when it is required. The final photon location is illustrated as solid red circles. The path towards the final destination is traced by faded red circles. The reflection to any desired port is now available in an active network. The reflection occurs in sections indicated by gray boxes.

Consider an example of the entangled state distribution illustrated in Fig. 6·16. The network configuration is similar to the one in Fig. 6·14 but all passive phase shifters are replaced by active phase shifters now. The initial state is split into right moving and left moving amplitudes by the central multiport unit. The left moving amplitude leaving port f_0 while the right moving amplitude leaves port e_1 of the central unit. The amplitude leaving f_0 enters one of the second layer unit from the port e. The active phase shifter is now

required in the second layer to switch the photon direction from port e to f on the same side after its reflection at the multiport unit. The photon proceed to the third layer after an appropriate phase shift at the second layer. Unlike the passive network, all inner third layer ports become accessible now. The photon entering the third layer from port e leaves the system after reflection again. The right moving amplitude can be controlled in a similar way as the left moving amplitude. The right moving amplitude leaves from port e of the central unit. The amplitude enters a unit in the second layer from the port f. Unlike the left moving amplitude, the relative phase between two rails is positive since the amplitude is entered from f. The photon amplitude passes though the second layer multiport unit and leaves it from the e port. One more reflection is introduced in the third layer by applying an active phase shift as described above.

With the use of active phase shifters embedded in the system, the number of output ports increases to 36 from 16 in a three-layer setup. The scalability can be generalized to 4×3^n where n is the number of layers. In this subsection, we only considered the centralized configuration of the network where independent amplitudes travel over the right side and the left side of the network. In general, the right side amplitude can be redirected back to the left side of the device so that the two amplitude can reach end nodes positioned on the same side of the system.

6.9.3 Decentralized Fully Reconfigurable Entanglement Distribution Network

A completely flexible and reconfigurable network design can be implemented using the technical approach introduced above. One can insert two entangled photons at any part of the network indicated in Fig. 6·17. In this setup, we assume again that active phase shifters are available. There is no need for circulators at the insertion point now due to the active phase shifter availability.

The first photon of an entangled pair (labeled as 1 and displayed as a green circle) follows the green path, the second photon (labeled as 2, with a red circle) follows the red

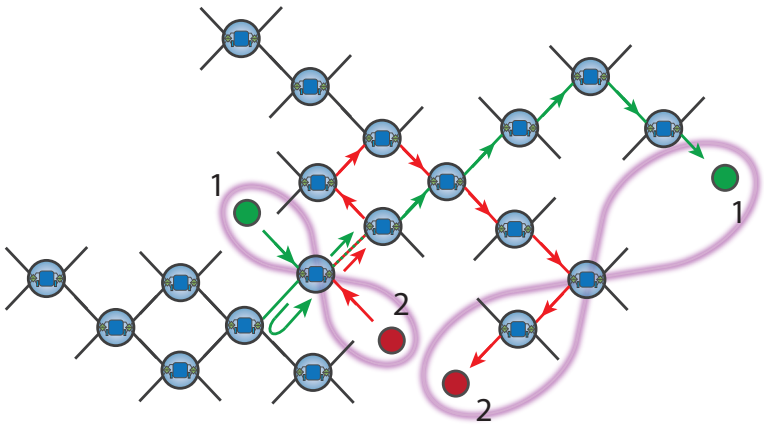

Figure 6·17: Decentralized fully reconfigurable entanglement distribution network. Two entangled photons (red and green circles) are inserted from two ports of the multiport unit. The propagation path of the first photon (labeled as 1) is indicated in green color and the second photon (labeled as 2) is indicated in red. They are following colored arrows in the diagram and finally entangle quantum devices at two remote nodes.

path. The first photon gets reflected at the first multiport unit, and the photon is sent to a unit in the opposite direction of the second photon. We set the active phase shifter so that the first photon is then reflected at the second multiport unit making the green photon to come back to the first unit. The rest of the propagation follows the same rule as the centralized network. Likewise, the second red photon gets reflected at the first multiport device and travels to the destination following the red arrows. The second photon experiences reflection with change in propagation direction by active phase shifters three times. The input state is traveling to two distinct locations and the output state remains entangled. We assumed the system is lossless, and the entanglement transportation is only done by phase shifts. The scheme does not require any post-selection, hence there is no reduction of amplitudes. We chose this specific travel path as an example. However the setup allows the users to engage any desired propagation pattern by introducing corresponding active phase mapping and redirecting entangled photons to different remote locations.

Note that the u-turn on the second and third time steps was added for the green photon in Fig. 6·17 in order to ensure that the two photons were not on the same edge at the same time. This allowed them to be controlled independently: by making sure they traverse any common links in their trajectories at different times, the two photons can be made to encounter different phase shifts at those locations and thereby be directed in different directions.

6.10 Multiphoton Transportation

We introduce multiphoton transformation in a network. Now, we consider sending a BS pre-processed four-photon state into the multiport as indicated in Fig. 6·18.

$$\begin{aligned} e_0 f_0 e_1 f_1 &\xrightarrow{BS} \tfrac{1}{4}(a_0-b_0)(a_0+b_0)(c_0-d_0)(c_0+d_0) \\ &\xrightarrow{M} \tfrac{1}{4}(a_0^2c_0^2 - a_0^2d_0^2 - b_0^2c_0^2 + b_0^2d_0^2) \\ &\xrightarrow{BSleft} \tfrac{1}{2}(c_0^2 e_0 f_0 - d_0^2 e_0 f_0) \xrightarrow{BSright} e_0 f_0 e_1 f_1 \end{aligned} \tag{6.65}$$

The input and output states are identical except for the propagation direction. The result implies that we can introduce a multiphoton entangled state.

Consider a four-photon GHZ state. We follow the state transformations given in Fig. 6·18.

$$\frac{1}{\sqrt{2}}(|HHHH\rangle + |VVVV\rangle) \propto \frac{1}{\sqrt{2}}(e_{0H} f_{0H} e_{1H} f_{1H} + e_{0V} f_{0V} e_{1V} f_{1V})\,|0\rangle\,. \tag{6.66}$$

We insert the GHZ state from all four spatial modes in the central portion of the network. We focus on the first horizontally polarized term of the equation.

$$e_{0HC} f_{0HC} e_{0HC} f_{0HC} \xrightarrow{Multiportunit} f_{1HUL} e_{1HBL} f_{0HUR} e_{0HBR}. \tag{6.67}$$

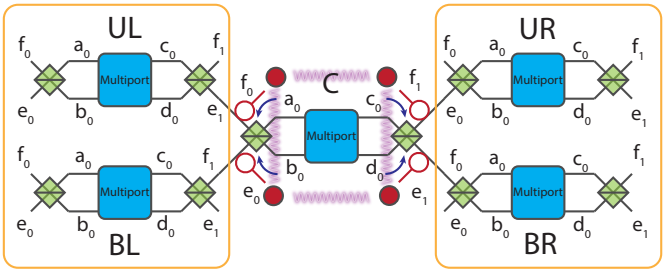

(a) System setup

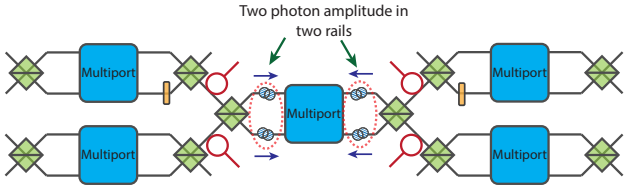

(b) State propagation after the first beam splitter transformations

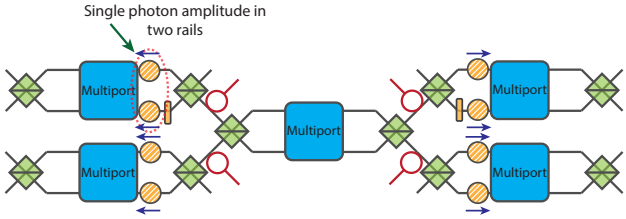

(c) Entering the second layer

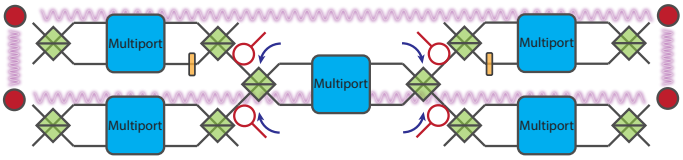

(d) Final result for the propagation from the network structure

Figure 6·18: (a) Four-photon insertion. We insert photons from the left and right side of the central multiport devices indicated as e_0, f_0, e_1, and f_1. (b) Initial photon transformation by the beam splitters. The transformed photons are sent to the multiport device simultaneously. (c) The photons are propagated in four distinct multiport units. (d) The photons in (c) are transformed by multiports and beam splitters. The photons from the central portion of the network is redistributed to the end of four different multiport units.

After the first transformation, the amplitudes are sent to all four second layer individually.

$$\xrightarrow{Multiportunit} e_{0HUL}e_{0HBL}e_{1HUR}e_{1HBR}. \tag{6.68}$$

The same is true for the other polarization, and the form does not change even though the actual state is in a superposition of two polarization. We chose four separate locations here, but it is possible to redistribute the photons in the same unit by utilizing active phase shifters (such state would be $e_{0HUL}f_{0HUL}e_{1HUR}f_{1HUR}$ meaning two photons in UL, two photons in UR).

6.11 Conclusion

We have shown that two-particle quantum interference allows two non-interacting, indistinguishable walkers to remain clustered as they walk along a chain of directionally-unbiased Grover four-ports. The resulting state is a superposition of two spatially-localized two-photon clusters, one confined near the origin, the other moving monotonically away. If the particles are entangled, the pair moves as a single unit, with undiminished entanglement. Whereas perfect state transport (PST) has been demonstrated for single photon states in various systems (Bellec et al., 2012; Perez-Leija et al., 2013; Chapman et al., 2016), this system demonstrates the existence of PST for entangled multi-particle states as well, with 50% arrival probability.

Potential applications are readily envisioned. Entangled pairs can be delivered in a controllable manner to distant locations for standard applications like entanglement swapping, quantum repeaters, or to control the flow of entanglement for two-photon interference effects in quantum networks (McMillan et al., 2013). Since the ballistic part moves with constant speed, these locations are addressable simply by waiting the appropriate amount of time for the amplitude to arrive.

One reason why utilizing the clustering effect can be useful in such applications, rather

than simply sending a photon pair along a fiber or through free space, is that by adding phase shifts in the lines between the multiports the flow of the photon pairs can be controlled; they can be stopped at a desired location (oscillating between two adjacent multiports) or their direction of motion can be reversed. This sort of control is something that cannot by done with a simple optical fiber, and here it can be done without damaging any entanglement between the photons. The means of such control is readily seen: inserting phase shifts of $\frac{\pi}{2}$ to an upper line and $-\frac{\pi}{2}$ to the corresponding lower line converts the reflecting and transmitting states of Eqs. 6.10 and 6.11 into each other, allowing the experimenter to controllably switch back and forth between ballistic and oscillating behavior.

Furthermore, the fact that there are two spatially-separated two-photon amplitudes means that those amplitudes can be brought back together and interfered with each other. This provides a means of probing the region that the ballistic portion has traveled through, allowing new two-photon sensing methods.

Additionally, we demonstrated higher dimensional quantum state manipulation such as the HOM effect and state redistribution by applying linear-optical four-ports realizing the four-dimensional Grover matrix accompanied by beam splitters and phase shifters. Identical photons are sent into two of the four input-output ports and split into right-moving and left-moving amplitudes, with no cross terms to observe the HOM effect. This absolute separation of propagation direction without mixing of right-moving and left-moving amplitudes insures the photons remain clustered as they propagate through the system. Variable phase shifts in the system allow the HOM photon pairs to switch between four spatial output destinations, which can increase information capacity. Time delays between emerging parts of the clustered two-photon state illustrating "delayed" HOM effect can be engineered using two multiports. Depending on the phase shifter position, the propagation direction can be reversed so that the right moving amplitude can get reflected at the second multiport, resulting in HOM pairs always leaving only from the left side of the system and with a

particular time-bin delay. The same situations have been investigated in a system without circulators. This system allows to redistribute the input state between the right and the left side of the system without changing amplitudes. The HOM effect and clustered photon pairs are widely used in quantum information science. The approach introduced here adds extra degrees of freedom, and paves the way for new applications that require control over the spatial and temporal modes of the HOM amplitudes as they move through one- and two-dimensional networks. We have demonstrated two photon amplitude control in both spatial and temporal modes. This two photon system can be extended to multiphoton input states, and manipulation of more complex entangled states have been explored as well.

The number of spatial modes can also be increased by connecting the multiple multiport units forming a network. We have demonstrated some theoretical framework to realize the entanglement distribution schemes. Experimental demonstration of such state transportation would be the next milestone to be achieved.

Chapter 7

Conclusions

7.1 Summary

We have introduced photonics based quantum information processing devices and their usage through potential applications in this dissertation. This dissertation is divided into three sections. The first section introduces a new device called directionally-unbiased linear-optical multiports which consists of multiple beam splitters and multiple mirrors. The operation of the devices is based on multipath interference effect and we integrated input and output ports together to perform certain quantum information processing efficiently. We used bulk optics to demonstrate tabletop experimental operation of the three-ports.

In later chapters, we introduced applications using such devices. We focused on quantum walk based applications. We provided some overview on quantum walks in a photonic platform and we show that the multiport devices we introduced can be used to form quantum walk systems. Topological photonics has been attracting attention due to the capability of protecting certain states against perturbation. It is known that linear optics based quantum walk systems can host topologically protected edge states which is robust against some perturbations in the system. In addition to the edge state protection, we demonstrate propagation suppression of bulk states as well using the multiport devices. By utilizing the bulk state suppression, we can introduce propagation suppression of polarized photons by inserting photons in topologically distinct bulks.

Topological photonics is global in the sense that the system requires significant amount of devices to demonstrate topological effects. Instead of using the global feature, we can

also look at the localized effect when multiple multiport devices are connected. Quantum walks are known for their ballistic spread of amplitude meaning one can find probability in an extended region. When the Grover four-port matrix is used to propagate amplitudes, we see state propagation without spreading amplitude meaning the photons remain localized while propagating. This localization can be used to introduce higher dimensional Hong-Ou-Mandel effect in spatial modes. This is further extended to quantum state redistribution where the input state can be redistributed between two different spatial modes without changing its final form. Not only we introduce HOM effect, we can apply the effect to entangled states and higher dimensional states as well. We formed an network system using the multiport based units consisting of a multiport with two beam splitters for some routing applications.

7.2 Future Work

7.2.1 Miniaturization of Multiport Devices

A directionally-unbiased three-port has been experimentally demonstrated on an optical table with bulk optical devices. The bulk implementation faced multiple obstacles need to be solved.

1. Phase sensitivity. Photon based experiments rely on interference in nature, therefore, precise control of relative phase is essential. This particular multiport system is based on multipath interference, and bulk optics has limitations in terms of precise phase locking. It is manageable for a single multiport device, however, this becomes an issue as soon as we introduce multiple copies of the multiport devices.

2. Scalability. To implement the applications introduced throughout this dissertation, it is necessary to prepare multiple devices and put them together. Having multiple copies of the multiports implies that phase sensitivity issue needs to be solved, and it can be

circumvented by miniaturize the device itself through an on-chip implementation. This result in the scalability of the device.

Direct implementation of the directionally-unbiased linear-optical multiport on a chip or fiber based optical tritter with mirrors can introduce flexible amplitude control. They would be suitable candidates for quantum walk and topological photonics. Another approach to introduce a robust photonic device would be by making use of an inverse design approach (Molesky et al., 2018). Inverse design based photonic chip is useful for the higher-dimensional HOM effect and state transfer due to the fact that they require a highly stable device realizing the 4 by 4 Grover matrix.

7.2.2 Topological Photonics

Two-dimensional Models

It is possible to form a mesh type of system by connecting multiple multiport systems in sequence. The transition from 1D and 2D systems changes several things in terms of topological invariance. A physical system can be classified topologically based on discrete symmetries. A 1D quantum walk system belongs to one of these topological classes AIII, BDI, D, DIII, and CII can provide topological invariance. A simple Hadamard 1D quantum walk system we investigated belongs to BDI, which satisfies all time-reversal, particle-hole, and chiral symmetry criteria according to the periodic table of topological insulator (Kitaev, 2009; Ryu et al., 2010; Morimoto and Furusaki, 2013). Other topological classes are available by increasing alternation steps such as four-step quantum walk (Asbóth and Obuse, 2013). In class BDI (see Table. 7.1), integer valued topological invariance would appear, however this is not the case for 2D system. Therefore, we need to look at some other symmetries or even no symmetries to have topological invariance. The periodic table in Table. 7.1 does not cover the Floquet topological insulators. Therefore, the extended version in (Roy and Harper, 2017) needs to be used. The applications we have introduced in this dissertation are using a Hermitian system.

Symmetry				Dimension							
Class	T	P	C	d = 1	2	3	4	5	6	7	8
A	0	0	0	0	$\mathbb{Z}$	0	$\mathbb{Z}$	0	$\mathbb{Z}$	0	$\mathbb{Z}$
AIII	0	0	1	$\mathbb{Z}$	0	$\mathbb{Z}$	0	$\mathbb{Z}$	0	$\mathbb{Z}$	0
AI	1	0	0	0	0	0	$\mathbb{Z}$	0	$\mathbb{Z}_2$	$\mathbb{Z}_2$	$\mathbb{Z}$
BDI	1	1	1	$\mathbb{Z}$	0	0	0	$\mathbb{Z}$	0	$\mathbb{Z}_2$	$\mathbb{Z}_2$
D	0	1	0	$\mathbb{Z}_2$	$\mathbb{Z}$	0	0	0	$\mathbb{Z}$	0	$\mathbb{Z}_2$
DIII	-1	1	1	$\mathbb{Z}_2$	$\mathbb{Z}_2$	$\mathbb{Z}$	0	0	0	$\mathbb{Z}$	0
AII	-1	0	0	0	$\mathbb{Z}_2$	$\mathbb{Z}_2$	$\mathbb{Z}$	0	0	0	$\mathbb{Z}$
CII	-1	-1	1	$\mathbb{Z}$	0	$\mathbb{Z}_2$	$\mathbb{Z}_2$	$\mathbb{Z}_2$	0	0	0
C	0	-1	0	0	$\mathbb{Z}$	0	$\mathbb{Z}_2$	$\mathbb{Z}_2$	$\mathbb{Z}$	0	0
CI	1	-1	1	0	0	$\mathbb{Z}$	0	$\mathbb{Z}_2$	$\mathbb{Z}_2$	$\mathbb{Z}$	0

Table 7.1: Periodic table for topological insulators. T, P, and C represent time-reversal, particle-hole, and chiral symmetry respectively. In the symmetry columns, value 0 shows no symmetry in the system. When operators T,P, and C, are introduced, the squares of the operators would be $T^2 = \pm 1$, $P^2 = \pm 1$, and $C^2 = 1$. Associated operators for time-reversal and particle-hole symmetry can be anti-unitary operators, therefore they can take -1 value as well. Dimension d is for the spatial dimension of a system. If the system is one dimensional, then topological invariance would appear when the system belongs to any of the topological classes AIII, BDI, D, DIII, and CII.

Bulk State Propagation Suppression in Different Quantum Walk Systems

In chapter 5, we introduced bulk state suppression for quantum information processing. It is possible to examine the same analysis for some other 1D systems (i.e. split-step quantum walk and extended long-range hopping based quantum walk). They can provide interesting features because they have more parameters to tune. We have briefly performed the same analysis using the split-step quantum walk model (see Appendix B). The result is not as simple as the two-phase Hadamard quantum walk model. Some topological amplitude suppression is present in the split-step model as well, but it has not been generalized, and the similar analysis can be performed in a different system to understand when exactly the bulk state suppression would occur.

Appendix A

Directionally-Unbiased Linear-Optical Multiports Matrix Method

We introduce a matrix method to construct the input-output transformation matrix of the three-port. Consider a three-port device with labels in Fig. A·1.

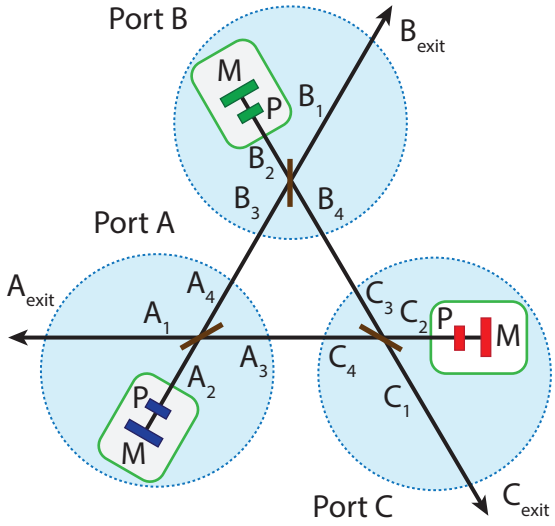

Figure A·1: Directionally-unbiased three-ports with labels at each vertex. A mirror unit is indicated in green squares.

The vertex consists of a beam splitter and a mirror with a phase shifter. The inputs and outputs are labeled as A_1, A_2, A_3, A_4, and A_{exit}. A_1 is used as an input port and A_{exit} is used as an exit port. A photon from the vertex A travels to vertex B and/or vertex C after the first BS encounter. We calculate the final propagation probability of a photon in the system by repeating some internal procedures. For the three-port device, it requires 15 by 15 matrices

to reconstruct the final matrix because a beam splitter has four ports and the exit is separated from the input, therefore each vertex consists of five entries. We have three sequential steps for the matrix reconstruction. 1. Photon insertion and the first BS encounter. 2. Amplitude transformation after a BS encounter (the photon either leaves the system or enters the mirror unit). 3. Amplitude transformation after a mirror unit.

We start with the first operation, using the photon labels, the photon travels from A_1 to A_3 and A_4. Second, the photon in A_3, A_4 travels to vertex B and/or C. At each vertex, the photon can either leave the system or stay in the system. If the photon stays in the system, we continue the calculation using the third step otherwise we keep the exit amplitudes for coherent amplitude summation until the end. The remaining photon travels from B_2 to B_3 and B_4 (C_2 to C_3 and C_4). We repeat this procedure of applying the second operation followed by the third operation until we reach the desired accuracy. For example, we can repeat the operation until the cumulative probability approaches to near 100%. After enough number of iterations, we extract some entries from the final 15 by 15 matrix to reconfigure the 3 by 3 matrix.

We show the full form of the initial step as well as the compact representation by using block matrices.

$$
\mathrm{U}_1 = \frac{1}{\sqrt{2}}
\begin{array}{c}
\\
A_1 \\ A_2 \\ A_3 \\ A_4 \\ A_{exit} \\ B_1 \\ B_2 \\ B_3 \\ B_4 \\ B_{exit} \\ C_1 \\ C_2 \\ C_3 \\ C_4 \\ C_{exit}
\end{array}
\begin{array}{c}
\begin{array}{ccccccccccccccc}
A_1 & A_2 & A_3 & A_4 & A_{exit} & B_1 & B_2 & B_3 & B_4 & B_{exit} & C_1 & C_2 & C_3 & C_4 & C_{exit}
\end{array} \\
\begin{pmatrix}
0 & 0 & 0 & 0 & 0 & 0 & 0 & 0 & 0 & 0 & 0 & 0 & 0 & 0 & 0 \\
0 & 0 & 0 & 0 & 0 & 0 & 0 & 0 & 0 & 0 & 0 & 0 & 0 & 0 & 0 \\
1 & 0 & 0 & 0 & 0 & 0 & 0 & 0 & 0 & 0 & 0 & 0 & 0 & 0 & 0 \\
i & 0 & 0 & 0 & 0 & 0 & 0 & 0 & 0 & 0 & 0 & 0 & 0 & 0 & 0 \\
0 & 0 & 0 & 0 & 0 & 0 & 0 & 0 & 0 & 0 & 0 & 0 & 0 & 0 & 0 \\
0 & 0 & 0 & 0 & 0 & 0 & 0 & 0 & 0 & 0 & 0 & 0 & 0 & 0 & 0 \\
0 & 0 & 0 & 0 & 0 & 0 & 0 & 0 & 0 & 0 & 0 & 0 & 0 & 0 & 0 \\
0 & 0 & 0 & 0 & 0 & 1 & 0 & 0 & 0 & 0 & 0 & 0 & 0 & 0 & 0 \\
0 & 0 & 0 & 0 & 0 & i & 0 & 0 & 0 & 0 & 0 & 0 & 0 & 0 & 0 \\
0 & 0 & 0 & 0 & 0 & 0 & 0 & 0 & 0 & 0 & 0 & 0 & 0 & 0 & 0 \\
0 & 0 & 0 & 0 & 0 & 0 & 0 & 0 & 0 & 0 & 0 & 0 & 0 & 0 & 0 \\
0 & 0 & 0 & 0 & 0 & 0 & 0 & 0 & 0 & 0 & 0 & 0 & 0 & 0 & 0 \\
0 & 0 & 0 & 0 & 0 & 0 & 0 & 0 & 0 & 0 & 1 & 0 & 0 & 0 & 0 \\
0 & 0 & 0 & 0 & 0 & 0 & 0 & 0 & 0 & 0 & i & 0 & 0 & 0 & 0 \\
0 & 0 & 0 & 0 & 0 & 0 & 0 & 0 & 0 & 0 & 0 & 0 & 0 & 0 & 0
\end{pmatrix}
\end{array}
\quad .(A.1)
$$

This matrix represents the initial operation. Top labels represent input and left labels

represent output. In the initial operation, a photon can enter the system from A1, B1, or C1. The photon entered from A1 leaves port A3 and/or A4. The same rule applies to a photon entering vertex B and C. In a mathematical form, the operation is given by $|A_1\rangle = \frac{1}{\sqrt{2}}(|A_3\rangle + i|A_4\rangle), |B_1\rangle = \frac{1}{\sqrt{2}}(|B_3\rangle + i|B_4\rangle), |C_1\rangle = \frac{1}{\sqrt{2}}(|C_3\rangle + i|C_4\rangle)$. It is possible to simplify the notation of the 15 by 15 matrix through block matrix representation. U_{Input} matrix represents a general transformation by a beam splitter.

$$U_{Input} = \begin{array}{c} \\ A_1 \\ A_2 \\ A_3 \\ A_4 \\ A_{exit} \end{array} \begin{array}{c} \begin{array}{ccccc} A_1 & A_2 & A_3 & A_4 & A_{exit} \end{array} \\ \begin{pmatrix} 0 & 0 & 0 & 0 & 0 \\ 0 & 0 & 0 & 0 & 0 \\ 1 & 0 & 0 & 0 & 0 \\ i & 0 & 0 & 0 & 0 \\ 0 & 0 & 0 & 0 & 0 \end{pmatrix} \end{array}. \tag{A.2}$$

$$U_1 = \frac{1}{\sqrt{2}} \begin{array}{c} \\ A \\ B \\ C \end{array} \begin{array}{c} \begin{array}{ccc} \text{A} & \text{B} & \text{C} \end{array} \\ \begin{pmatrix} U_{Input} & 0 & 0 \\ 0 & U_{Input} & 0 \\ 0 & 0 & U_{Input} \end{pmatrix} \end{array}. \tag{A.3}$$

U_1 is simplified using U_{Input} matrix. U_1 is still a 15 by 15 matrix. In a similar manner, the second operation can be simplified.

$$U_2 = \frac{1}{\sqrt{2}} \begin{array}{c} \\ A \\ B \\ C \end{array} \begin{array}{c} \begin{array}{ccc} \text{A} & \text{B} & \text{C} \end{array} \\ \begin{pmatrix} 0 & U_{BA} & U_{CA} \\ U_{AB} & 0 & U_{CB} \\ U_{AC} & U_{BC} & 0 \end{pmatrix} \end{array}. \tag{A.4}$$

An amplitude transition from A to B is described as U_{AB}, in the same way, transition from B to A is described as U_{BA}. U_{AB} describes the amplitude transformation of the second beam splitter encounter. After leaving the first beam splitter, the photon leaves the system or travels to the mirror unit. The extra phase ϕ_A is imposed at the mirror unit.

$$U_{AB} = \begin{array}{c} \\ B_1 \\ B_2 \\ B_3 \\ B_4 \\ B_{exit} \end{array} \begin{array}{c} \begin{array}{ccccc} A_1 & A_2 & A_3 & A_4 & A_{exit} \end{array} \\ \begin{pmatrix} 0 & 0 & 0 & 0 & 0 \\ 0 & 0 & 0 & ie^{i\phi_B} & 0 \\ 0 & 0 & 0 & 0 & 0 \\ 0 & 0 & 0 & 0 & 0 \\ 0 & 0 & 0 & 1 & 0 \end{pmatrix} \end{array}. \tag{A.5}$$

$$U_{AB} = \begin{array}{c} \\ A_1 \\ A_2 \\ A_3 \\ A_4 \\ A_{exit} \end{array} \begin{array}{c} \begin{array}{ccccc} B_1 & B_2 & B_3 & B_4 & B_{exit} \end{array} \\ \begin{pmatrix} 0 & 0 & 0 & 0 & 0 \\ 0 & 0 & e^{i\phi_A} & 0 & 0 \\ 0 & 0 & 0 & 0 & 0 \\ 0 & 0 & 0 & 0 & 0 \\ 0 & 0 & i & 0 & 0 \end{pmatrix} \end{array}. \tag{A.6}$$

The third operation describes the photon leaving the mirror unit. This operation represents a propagation within the same vertex.

$$U_3 = \frac{1}{\sqrt{2}} \begin{array}{c} \\ A \\ B \\ C \end{array} \begin{array}{c} \begin{array}{ccc} \text{A} & \text{B} & \text{C} \end{array} \\ \begin{pmatrix} U_{third} & 0 & 0 \\ 0 & U_{third} & 0 \\ 0 & 0 & U_{third} \end{pmatrix} \end{array}. \tag{A.7}$$

$$U_{Third} = \begin{array}{c} \\ A_1 \\ A_2 \\ A_3 \\ A_4 \\ A_{exit} \end{array} \begin{array}{c} \begin{array}{ccccc} A_1 & A_2 & A_3 & A_4 & A_{exit} \end{array} \\ \begin{pmatrix} 0 & 0 & 0 & 0 & 0 \\ 0 & 0 & 0 & 0 & 0 \\ 0 & i & 0 & 0 & 0 \\ 0 & 1 & 0 & 0 & 0 \\ 0 & 0 & 0 & 0 & 0 \end{pmatrix} \end{array}. \tag{A.8}$$

These three operations are the unit operations and we repeat operation 2 and 3 to describe photon propagation in the system.

$N = 2 : U_{Multiport} = U_2 U_1,$

$N = 4 : U_{Multiport} = U_2 U_3 U_2 U_1,$

$N = 6 : U_{Multiport} = U_2 U_3 U_2 U_3 U_2 U_1,$

$N = 8 : U_{Multiport} = U_2 U_3 U_2 U_3 U_2 U_3 U_2 U_1,$

where N represents the numbers of beam splitter encounter. We can reconstruct the 3 by 3 matrix by choosing the transition from A_1, B_1, and C_1 to A_{exit}, B_{exit}, and C_{exit} from the 15 by 15 matrix. After large enough number of iterations, we obtain the final matrix below.

$$
\mathrm{U}_{Multiport} = \begin{array}{c|ccccc|ccccc|ccccc}
 & A_1 & A_2 & A_3 & A_4 & A_{exit} & B_1 & B_2 & B_3 & B_4 & B_{exit} & C_1 & C_2 & C_3 & C_4 & C_{exit} \\
\hline
A_1 & 0 & 0 & 0 & 0 & 0 & 0 & 0 & 0 & 0 & 0 & 0 & 0 & 0 & 0 & 0 \\
A_2 & 0 & 0 & 0 & 0 & 0 & \frac{-i}{3} & 0 & 0 & 0 & 0 & \frac{i}{3} & 0 & 0 & 0 & 0 \\
A_3 & 0 & 0 & 0 & 0 & 0 & 0 & 0 & 0 & 0 & 0 & 0 & 0 & 0 & 0 & 0 \\
A_4 & 0 & 0 & 0 & 0 & 0 & 0 & 0 & 0 & 0 & 0 & 0 & 0 & 0 & 0 & 0 \\
\hline
A_{exit} & \frac{-i}{3} & 0 & 0 & 0 & 0 & \frac{2i}{3} & 0 & 0 & 0 & 0 & \frac{2i}{3} & 0 & 0 & 0 & 0 \\
\hline
B_1 & 0 & 0 & 0 & 0 & 0 & 0 & 0 & 0 & 0 & 0 & 0 & 0 & 0 & 0 & 0 \\
B_2 & \frac{i}{3} & 0 & 0 & 0 & 0 & 0 & 0 & 0 & 0 & 0 & \frac{-i}{3} & 0 & 0 & 0 & 0 \\
B_3 & 0 & 0 & 0 & 0 & 0 & 0 & 0 & 0 & 0 & 0 & 0 & 0 & 0 & 0 & 0 \\
B_4 & 0 & 0 & 0 & 0 & 0 & 0 & 0 & 0 & 0 & 0 & 0 & 0 & 0 & 0 & 0 \\
\hline
B_{exit} & \frac{2i}{3} & 0 & 0 & 0 & 0 & \frac{-i}{3} & 0 & 0 & 0 & 0 & \frac{2i}{3} & 0 & 0 & 0 & 0 \\
\hline
C_1 & 0 & 0 & 0 & 0 & 0 & 0 & 0 & 0 & 0 & 0 & 0 & 0 & 0 & 0 & 0 \\
C_2 & \frac{-i}{3} & 0 & 0 & 0 & 0 & \frac{i}{3} & 0 & 0 & 0 & 0 & 0 & 0 & 0 & 0 & 0 \\
C_3 & 0 & 0 & 0 & 0 & 0 & 0 & 0 & 0 & 0 & 0 & 0 & 0 & 0 & 0 & 0 \\
C_4 & 0 & 0 & 0 & 0 & 0 & 0 & 0 & 0 & 0 & 0 & 0 & 0 & 0 & 0 & 0 \\
\hline
C_{exit} & \frac{2i}{3} & 0 & 0 & 0 & 0 & \frac{2i}{3} & 0 & 0 & 0 & 0 & \frac{-i}{3} & 0 & 0 & 0 & 0
\end{array}
\quad .(A.9)
$$

We are interested in the relationship between input ports and output ports, therefore we select the specific entries to reconstruct the desired matrix.

$$
U_{out} = \begin{array}{c} \\ A_{exit} \\ B_{exit} \\ C_{exit} \end{array} \begin{array}{c} \begin{array}{ccc} A_1 & B_1 & C_1 \end{array} \\ \begin{pmatrix} A_1 \to A_{exit} & B_1 \to A_{exit} & C_1 \to A_{exit} \\ A_1 \to B_{exit} & B_1 \to B_{exit} & C_1 \to B_{exit} \\ A_1 \to C_{exit} & B_1 \to C_{exit} & C_1 \to C_{exit} \end{pmatrix} \end{array} \tag{A.10}
$$

The final matrix is

$$
U_{out} = \begin{array}{c} \\ A_{exit} \\ B_{exit} \\ C_{exit} \end{array} \begin{array}{c} \begin{array}{ccc} A_1 & B_1 & C_1 \end{array} \\ \begin{pmatrix} \frac{-i}{3} & \frac{2i}{3} & \frac{2i}{3} \\ \frac{2i}{3} & \frac{-i}{3} & \frac{2i}{3} \\ \frac{2i}{3} & \frac{2i}{3} & \frac{-i}{3} \end{pmatrix} \end{array}. \tag{A.11}
$$

N-port can be constructed using the same procedure. We used a specific splitting ratio for a beam splitter, but it can be changed to arbitrary values.

Appendix B

Split-Step Quantum Walk

In the main text, we have focused on the simple Hadamard walk to demonstrate the topological suppression of bulk state and topological protection of edge states. Instead of using a single operator, we can introduce two operators and periodically alternate between the two. In a split step quantum walk model, the coin operators are alternated every single step. The single unitary operator consists of $U = SC_2(\theta_2)SC_1(\theta_1)$ where θ_1 and θ_2 are coin operator angles respectively. Having two angle tuning parameters allows to introduce more topological classifications based on winding numbers. We follow the derivation of winding number in split-step quantum walk by (Obuse et al., 2015). Using the equations below, we can draw the winding number diagram given in Fig. B·2.

$$\nu_\pi = \frac{(sign[-sin(\theta_1) - sin(\theta_2)] + 1)}{2}, \nu_0 = \frac{(sign[sin(\theta_1) - sin(\theta_2)] + 1)}{2} \tag{B.1}$$

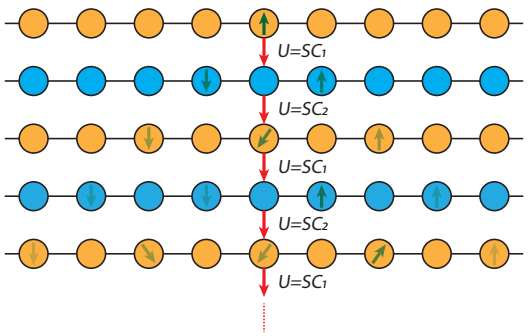

Figure B·1: Split-step quantum walk. The unitary transformation alternates between two steps. The first step uses SC_1 and the second step uses SC_2.

In the simple quantum walk model, zero or two isolated values exist depending on the topological property of the system in the eigenvalue diagram. In the case of split-step walk, we would see four patterns.

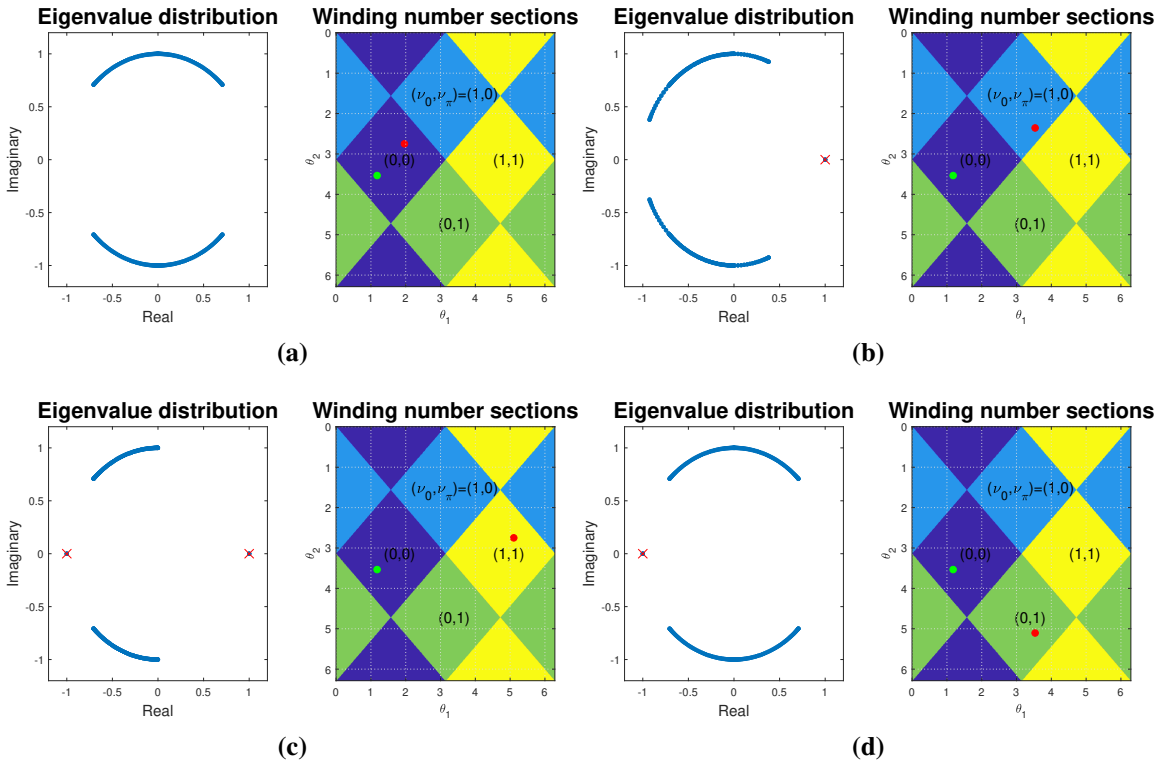

Figure B·2: Eigenvalue distribution of split-step quantum walk system. The system consists of two bulk regions. The red dot in the winding number sections corresponds to coin angles for the right region and the green dot is responsible for the left region. The coin operator angle for the left region is fixed to have winding number equal to $(\nu_0,\nu_\pi) = (0,0)$. We examine four distinct topological regions and show distinct isolated eigenvalues. (a) Both angles stay in region $(\nu_0,\nu_\pi) = (0,0)$. Since they are both in the same region, there is no topologically protected state. (b) Right winding number is $(\nu_0,\nu_\pi) = (1,0)$. $\Delta\nu_0 = 1, \Delta\nu_\pi = 0$ and there is one isolated eigenvalue. (c) Right winding number is $(\nu_0,\nu_\pi) = (1,1)$. $\Delta\nu_0 = 1, \Delta\nu_\pi = 1$ and there are two isolated eigenvalues. (d) Right winding number is $(\nu_0,\nu_\pi) = (0,1)$. $\Delta\nu_0 = 0, \Delta\nu_\pi = 1$ and there is one isolated eigenvalue.

When a photon is inserted at the boundary with topologically distinct regions, we observe topologically protected state similar to the single-step quantum walk case. We perform the same probability distribution analysis as the single-step case for completeness. We fix the

left coin angles so that we have $(\nu_0, \nu_\pi) = (0, 0)$ for the left bulk. The figures show the remaining probability distribution when all the coin angles on the right side are exhausted. We observe leakage of amplitude when $\Delta\nu_0 = 1$ while $\Delta\nu_\pi = 0$ is maintained. The result is not as straight forward as the single-step quantum walk, however, the result could be utilized for quantum information processing applications.

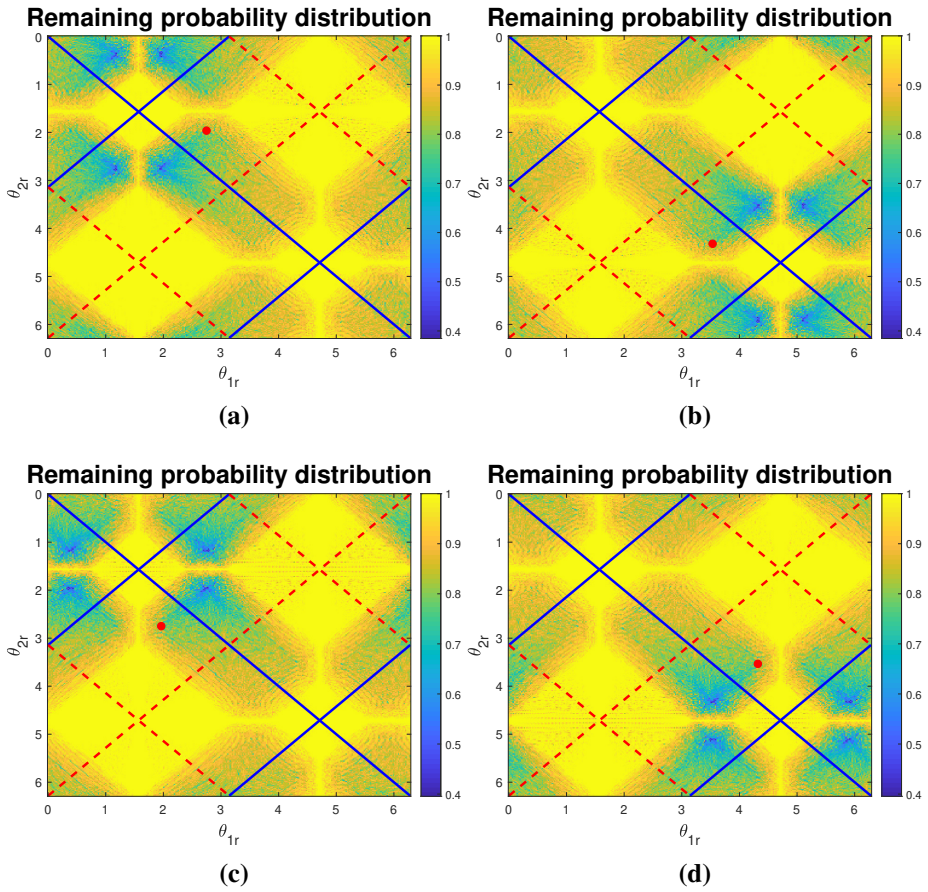

Figure B·3: Probability distribution for each topologically distinct regions. The system has four parameters to tweak around. Left side phases are fixed as indicated as a red dot for each figure. Right side phase parameters are translated from 0 to 2π. Blue solid line indicates gap closure at $E = \pi$ and red dashed line indicates gap closure at $E = 0$ (a) Non-topological region. (b) Topological region. The red box shows strongly suppressed region compared to the non-topological bulks. The side length of the box is $\frac{\pi}{4}$.

Appendix C

MATLAB Codes Used for Simulations

MATLAB code used for topological quantum walks.

```
%Author Shuto Osawa
clear all
close all
%Phase settings
theta1l = 7*pi/4;
theta1r = pi/4;
%Length of the chain
ln = 100;
ln2 = 50;
SC1 = zeros(ln*2);
input = zeros(ln*2,1);
input(ln) = 1;


for i = 1:ln
    Z = zeros(1,ln);
    Z(i) = 1;
        if i+1 > ln
            Zp = zeros(1,ln);
            Zp(1) = 1;
        else
            Zp = zeros(1,ln);
            Zp(i+1) = 1;
        end
        if i-1 == 0
            Zm = zeros(1,ln);
            Zm(ln) = 1;
        else
            Zm = zeros(1,ln);
            Zm(i-1) = 1;
        end
```

```
        if i <= ln/2
            mat1 = [cos(theta1l) sin(theta1l); 0 0];
            mat2 = [0 0 ;sin(theta1l) -cos(theta1l)];
        else
            mat1 = [cos(theta1r) sin(theta1r); 0 0];
            mat2 = [0 0 ;sin(theta1r) -cos(theta1r)];
        end
        SC1 = SC1+kron(kron(Zp',Z),mat1)+kron(kron(Zm',Z),mat2);
end

QW = input;
array0 = zeros(ln*2);
array = zeros(ln2,ln+1);
array2 = zeros(ln/2);

for j = 1:ln2
    QW = SC1*QW;
    QWP = QW.*conj(QW);
    odd = QWP(1:2:end);
    even = QWP(2:2:end-1);
    even = [even; 0];
    fin = odd+even;
    fintrans = fin';
    array(j,:) = [0 fintrans(1:end)];
end

%probr = sum(QWP(ln+1:end));
%probl = sum(QWP(1:ln));

figure(1)
set(gcf, 'Position',  [400, 100, 600, 500])
imagesc(linspace(-ln/2,ln/2,ln),linspace(0,ln2,ln2),array)
colormap(jet)
caxis([0 1])
ylabel('QW steps','FontSize',14)
xlabel('QW lattice site','FontSize',14)
title(['Quantum walk probability distribution'],'FontSize',24)
set(gcf,'color','w');
```

MATLAB code used for eigenvalues of quantum walk unitary matrix.

```
%Author Shuto Osawa
clear all
```

```
close all

ln =100
SC = zeros(ln*2);
theta = pi/8
theta2 = pi/8
input = zeros(ln*2,1)
input(ln) = 1
bar(input)
for i = 1:ln
    Z = zeros(1,ln);
    Z(i) = 1;

    if i+1 > ln
        Zp = zeros(1,ln);
        Zp(1) = 1;
    else
        Zp = zeros(1,ln);
        Zp(i+1) = 1;
    end
    if i-1 == 0
        Zm = zeros(1,ln);
        Zm(ln) = 1;
    else
        Zm = zeros(1,ln);
        Zm(i-1) = 1;
    end
    if i <= ln/2
        mat1 = [cos(theta) sin(theta); 0 0];
        mat2 = [0 0 ;sin(theta) -cos(theta)];
    else
        mat1 = [cos(theta2) sin(theta2); 0 0];
        mat2 = [0 0 ;sin(theta2) -cos(theta2)];
    end
    SC = SC+kron(kron(Zp',Z),mat1)+kron(kron(Zm',Z),mat2);
end
[V,D] = eig(SC);
e = diag(D);
e.*conj(e);
figure(1)
set(gcf,'color','w');
set(gcf, 'Position',  [400, 400, 450, 400])
```

```
%subplot(1,2,1)
plot(exp(1i*pi/2)*e,'.','MarkerSize',10)
hold on
%plot(exp(1i*pi/2)*1i,'xr','MarkerSize',10)
hold on
%plot(-exp(1i*pi/2)*1i,'xr','MarkerSize',10)
title(['Eigenvalue distribution'],'Fontsize',16)
xlabel('Real')
ylabel('Imaginary')
xlim([-1.2 1.2])
ylim([-1.2 1.2])
```

MATLAB code used for probability distribution based on topological quantum walks.

```
%Author Shuto Osawa
clear all
close all

rep = 51
ln = 100;


probplot = zeros(rep);
probc = zeros(rep);

ref = 1
for l = 1:rep
    for m = 1:rep

SC1 = zeros(ln*2);

theta1l = 2*pi*(l-1)/(rep-1);
theta1r = 2*pi*(m-1)/(rep-1);

input = zeros(ln*2,1);
input(ln+ln/2) = 1;

for i = 1:ln

    Z = zeros(1,ln);
    Z(i) = 1;

        if i+1 > ln
```

```
            Zp = zeros(1,ln);
            Zp(1) = 1;
        else
            Zp = zeros(1,ln);
            Zp(i+1) = 1;
        end
        if i-1 == 0
            Zm = zeros(1,ln);
            Zm(ln) = 1;
        else
            Zm = zeros(1,ln);
            Zm(i-1) = 1;
        end
        if i <= ln/2
            mat1 = [cos(theta1l) sin(theta1l); 0 0];
            mat2 = [0 0 ;sin(theta1l) -cos(theta1l)];
        else
            mat1 = [cos(theta1r) sin(theta1r); 0 0];
            mat2 = [0 0 ;sin(theta1r) -cos(theta1r)];
        end
        SC1 = SC1+kron(kron(Zp',Z),mat1)+kron(kron(Zm',Z),mat2);

end

ln2 = 1001;
array = [];

QW = (SC1^(ln2-1))*input;
QWP = abs(QW.*conj(QW));
odd = QWP(1:2:end);
even = QWP(2:2:end-1);
even = [0; even];
fin = odd+even;

probr = sum(fin(ln/2+1:end));
probl = sum(fin(1:ln/2));


probplot(l,m) = probr;
probc(l,m) = fin(ln/2);

ref = ref+1;
```

```
waitbar(ref/(rep*rep))
    end
end

figure(1)
imagesc(linspace(0,2*pi,rep),linspace(0,2*pi,rep),probplot)
set(gcf,'color','w')
xlabel('\theta_R','FontSize',14)
ylabel('\theta_L','FontSize',14)

title(['Remaining probability distribution'],'FontSize',16)
hold on
line([0,2*pi], [pi,pi], 'Color', 'r','LineWidth',2);
hold on
line( [pi,pi],[0,2*pi], 'Color', 'r','LineWidth',2);
colorbar
```

References

Aaronson, S. and Ambainis, A. (2003). Quantum search of spatial regions. In *FOCS '03: Proceedings of the 44th Annual IEEE Symposium on Foundations of Computer Science*, pages 200–209. IEEE.

Aaronson, S. and Arkhipov, A. (2011). The computational complexity of linear optics. In *Proceedings of the forty-third annual ACM symposium on Theory of computing*, pages 333–342.

Abal, G., Donangelo, R., Forets, M., and Portugal, R. (2012). Spatial quantum search in a triangular network. *Mathematical Structures in Computer Science*, 22(3):521–531.

Abal, G., Donangelo, R., Marquezino, F. L., and Portugal, R. (2010). Spatial search on a honeycomb network. *Mathematical Structures in Computer Science*, 20(6):999–1009.

Agarwal, G. S. (2012). *Quantum optics*. Cambridge University Press.

Aharonov, Y., Davidovich, L., and Zagury, N. (1993). Quantum random walks. *Physical Review A*, 48(2):1687.

Altepeter, J. B., Branning, D., Jeffrey, E., Wei, T., Kwiat, P. G., Thew, R. T., O'Brien, J. L., Nielsen, M. A., and White, A. G. (2003). Ancilla-assisted quantum process tomography. *Physical Review Letters*, 90(19):193601.

Ambainis, A. (2007). Quantum walk algorithm for element distinctness. *SIAM Journal on Computing*, 37(1):210–239.

Ambainis, A., Prūsis, K., Vihrovs, J., and Wong, T. G. (2016). Oscillatory localization of quantum walks analyzed by classical electric circuits. *Physical Review A*, 94(6):062324.

Armstrong, J., Bloembergen, N., Ducuing, J., and Pershan, P. S. (1962). Interactions between light waves in a nonlinear dielectric. *Physical Review*, 127(6):1918.

Asbóth, J. K. and Obuse, H. (2013). Bulk-boundary correspondence for chiral symmetric quantum walks. *Physical Review B*, 88(12):121406.

Asbóth, J. K., Oroszlány, L., and Pályi, A. (2016). *A short course on topological insulators*, volume 919. Springer.

Bachmayr, M., Schneider, R., and Uschmajew, A. (2016). Tensor networks and hierarchical tensors for the solution of high-dimensional partial differential equations. *Foundations of Computational Mathematics*, 16(6):1423–1472.

Barkhofen, S., Nitsche, T., Elster, F., Lorz, L., Gábris, A., Jex, I., and Silberhorn, C. (2017). Measuring topological invariants in disordered discrete-time quantum walks. *Physical Review A*, 96(3):033846.

Barreiro, J. T., Langford, N. K., Peters, N. A., and Kwiat, P. G. (2005). Generation of hyperentangled photon pairs. *Physical Review Letters*, 95(26):260501.

Bartkiewicz, K., Černoch, A., and Lemr, K. (2018). Implementation of an efficient linear-optical quantum router. *Scientific Reports*, 8(1):1–8.

Bell, J. S. (1964). On the einstein podolsky rosen paradox. *Physics Physique Fizika*, 1(3):195.

Bellec, M., Nikolopoulos, G. M., and Tzortzakis, S. (2012). Faithful communication hamiltonian in photonic lattices. *Optics letters*, 37(21):4504–4506.

Benioff, P. (2000). Space searches with a quantum robot. *arXiv preprint quant-ph/0003006*.

Bennett, C. H. and Brassard, G. (1984). Quantum cryptography: Public key distribution and coin tossing. In *Proceedings of the International Conference on Computers, Systems and Signal Processing*.

Bentivegna, M., Spagnolo, N., Vitelli, C., Flamini, F., Viggianiello, N., Latmiral, L., Mataloni, P., Brod, D. J., Galvão, E. F., Crespi, A., Ramponi, R., Osellame, R., and Sciarrino, F. (2015). Experimental scattershot boson sampling. *Science Advances*, 1(3):e1400255.

Bernevig, B. A. and Hughes, T. L. (2013). *Topological insulators and topological superconductors*. Princeton university press.

Bose, S. (2003). Quantum communication through an unmodulated spin chain. *Physical Review Letters*, 91(20):207901.

Bouwmeester, D., Marzoli, I., Karman, G. P., Schleich, W., and Woerdman, J. (1999a). Optical galton board. *Physical Review A*, 61(1):013410.

Bouwmeester, D., Pan, J.-W., Daniell, M., Weinfurter, H., and Zeilinger, A. (1999b). Observation of three-photon greenberger-horne-zeilinger entanglement. *Physical Review Letters*, 82(7):1345.

Boyd, R. W. (2020). *Nonlinear optics*. Academic press.

Briegel, H.-J., Dür, W., Cirac, J. I., and Zoller, P. (1998). Quantum repeaters: the role of imperfect local operations in quantum communication. *Physical Review Letters*, 81(26):5932.

Bromberg, Y., Lahini, Y., Morandotti, R., and Silberberg, Y. (2009). Quantum and classical correlations in waveguide lattices. *Physical Review Letters*, 102(25):253904.

Broome, M. A., Fedrizzi, A., Lanyon, B. P., Kassal, I., Aspuru-Guzik, A., and White, A. G. (2010). Discrete single-photon quantum walks with tunable decoherence. *Physical Review Letters*, 104(15):153602.

Broome, M. A., Fedrizzi, A., Rahimi-Keshari, S., Dove, J., Aaronson, S., Ralph, T. C., and White, A. G. (2013). Photonic boson sampling in a tunable circuit. *Science*, 339(6121):794–798.

Buhrman, H. and Špalek, R. (2006). Quantum verification of matrix products. In *SODA '06: Proceedings of the seventeenth annual ACM-SIAM symposium on Discrete algorithm*, pages 880–889. Society for Industrial and Applied Mathematics.

Campos, R. A. (2000). Three-photon hong-ou-mandel interference at a multiport mixer. *Physical Review A*, 62(1):013809.

Cardano, F., D'Errico, A., Dauphin, A., Maffei, M., Piccirillo, B., de Lisio, C., De Filippis, G., Cataudella, V., Santamato, E., Marrucci, L., et al. (2017). Detection of zak phases and topological invariants in a chiral quantum walk of twisted photons. *Nature Communications*, 8(1):1–7.

Cardano, F., Massa, F., Qassim, H., Karimi, E., Slussarenko, S., Paparo, D., de Lisio, C., Sciarrino, F., Santamato, E., Boyd, R. W., et al. (2015). Quantum walks and wavepacket dynamics on a lattice with twisted photons. *Science Advances*, 1(2):e1500087.

Carneiro, I., Loo, M., Xu, X., Girerd, M., Kendon, V., and Knight, P. L. (2005). Entanglement in coined quantum walks on regular graphs. *New Journal of Physics*, 7(1):156.

Carolan, J., Harrold, C., Sparrow, C., Martín-López, E., Russell, N. J., Silverstone, J. W., Shadbolt, P. J., Matsuda, N., Oguma, M., Itoh, M., Marshall, Graham D.and Thompson, M. G., Matthews, J. C. F., Hashimoto, T., O'Brien, J. L., and Laing, A. (2015). Universal linear optics. *Science*, 349(6249):711–716.

Chapman, R. J., Santandrea, M., Huang, Z., Corrielli, G., Crespi, A., Yung, M. H., Osellame, R., and Peruzzo, A. (2016). Experimental perfect state transfer of an entangled photonic qubit. *Nature Communications*, 7:11339.

Childs, A. M. (2009). Universal computation by quantum walk. *Physical Review Letters*, 102(18):180501.

Childs, A. M., Cleve, R., and Deotto, E. (2003). Exponential algorithmic speedup by a quantum walk. In *STOC '03: Proceedings of the thirty-fifth annual ACM symposium on Theory of computing.*, pages 59–68. ACM.

Childs, A. M., Farhi, E., and Gutmann, S. (2002). An example of the difference between quantum and classical random walks. *Quantum Information Processing*, 1(1-2):35–43.

Childs, A. M. and Goldstone, J. (2004). Spatial search by quantum walk. *Physical Review A*, 70(2):022314.

Chuang, I. L. and Nielsen, M. A. (1997). Prescription for experimental determination of the dynamics of a quantum black box. *Journal of Modern Optics*, 44(11-12):2455–2467.

Clements, W. R., Humphreys, P. C., Metcalf, B. J., Kolthammer, W. S., and Walmsley, I. A. (2016). Optimal design for universal multiport interferometers. *Optica*, 3(12):1460–1465.

Crespi, A., Osellame, R., Ramponi, R., Brod, D. J., Galvao, E. F., Spagnolo, N., Vitelli, C., Maiorino, E., Mataloni, P., and Sciarrino, F. (2013a). Integrated multimode interferometers with arbitrary designs for photonic boson sampling. *Nature Photonics*, 7(7):545.

Crespi, A., Osellame, R., Ramponi, R., Giovannetti, V., Fazio, R., L.Sansoni, Nicola, F. D., Sciarrino, F., and Mataloni, P. (2013b). Anderson localization of entangled photons in an integrated quantum walk. *Nature Photonics*, 7(4):322.

Crownover, R. M. (1995). *Introduction to fractals and chaos*. Jones and Bartlett Books in Mathematics.

de Guise, H., Di Matteo, O., and Sánchez-Soto, L. L. (2018). Simple factorization of unitary transformations. *Physical Review A*, 97(2):022328.

de Guise, H., Tan, S. H., Poulin, I. P., and Sanders, B. C. (2014). Coincidence landscapes for three-channel linear optical networks. *Physical Review A*, 89(6):063819.

De Nicola, F., Sansoni, L., Crespi, A., Ramponi, R., Osellame, R., Giovannetti, V., Fazio, R., Mataloni, P., and Sciarrino, F. (2014). Quantum simulation of bosonic-fermionic noninteracting particles in disordered systems via a quantum walk. *Physical Review A*, 89(3):032322.

Dowling, J. P. (2008). Quantum optical metrology–the lowdown on high-n00n states. *Contemporary Physics*, 49(2):125–143.

Dür, W., Vidal, G., and Cirac, J. I. (2000). Three qubits can be entangled in two inequivalent ways. *Physical Review A*, 62(6):062314.

Einstein, A., Podolsky, B., and Rosen, N. (1935). Can quantum-mechanical description of physical reality be considered complete? *Physical Review*, 47(10):777.

Ekert, A. K. (1991). Quantum cryptography based on bell's theorem. *Physical Review Letters*, 67(6):661.

Endo, T., Konno, N., and Obuse, H. (2015). Relation between two-phase quantum walks and the topological invariant. *arXiv preprint arXiv:1511.04230*.

Fan, S., Villeneuve, P. R., Joannopoulos, J. D., and Haus, H. A. (1998). Channel drop tunneling through localized states. *Physical Review Letters*, 80(5):960.

Feldman, E. and Hillery, M. (2004). Scattering theory and discrete-time quantum walks. *Physics Letters A*, 324(4):277–281.

Feldman, E. and Hillery, M. (2007). Modifying quantum walks: a scattering theory approach. *Journal of Physics A*, 40(37):11343.

Feynman, R. P. (1982). Simulating physics with computers. *International Journal of Theoretical Physics*, 21(6/7).

Francisco, D., Iemmi, C., Paz, J., and Ledesma, S. (2006). Simulating a quantum walk with classical optics. *Physical Review A*, 74(5):052327.

Franson, J. D. (1989). Bell inequality for position and time. *Physical Review Letters*, 62(19):2205.

Geraldi, A., Bonavena, L. D., Liorni, C., Mataloni, P., and Cuevas, Á. (2019). A novel bulk-optics scheme for quantum walk with high phase stability. *Condensed Matter*, 4(1):14.

Gerry, C., Knight, P., and Knight, P. L. (2005). *Introductory quantum optics*. Cambridge university press.

Gottesman, D. (1998). The heisenberg representation of quantum computers. *arXiv preprint quant-ph/9807006*.

Goyal, S. K., Roux, F. S., Forbes, A., and Konrad, T. (2013). Implementing quantum walks using orbital angular momentum of classical light. *Physical Review Letters*, 110(26):263602.

Greenberger, D. M., Horne, M. A., and Zeilinger, A. (1989). Going beyond bell's theorem. In *Bell's theorem, quantum theory and conceptions of the universe*, pages 69–72. Springer.

Grover, L. K. (1996). A fast quantum mechanical algorithm for database search. In *Proceedings of the Twenty-Eighth Annual ACM Symposium on the Theory of Computing, Philadelphia, Pennsylvania*, pages 212–219.

Hafezi, M. (2014). Measuring topological invariants in photonic systems. *Physical Review Letters*, 112(21):210405.

Hamel, D. R., Shalm, L. K., Hübel, H., Miller, A. J., Marsili, F., Verma, V. B., Mirin, R. P., Nam, S. W., Resch, K. J., and Jennewein, T. (2014). Direct generation of three-photon polarization entanglement. *Nature Photonics*, 8(10):801–807.

Hasan, M. Z. and Kane, C. L. (2010). Colloquium: topological insulators. *Reviews of Modern Physics*, 82(4):3045.

He, Y., Ding, X., Su, Z. E., Huang, H. L., Qin, J., Wang, C., Unsleber, S., Chen, C., Wang, H., He, Y. M., Wang, X. L., Zhang, W., Chen, S. J., Schneider, C., Kamp, M., You, L. X., Wang, Z., Höfling, S., Lu, C., and Pan, J. W. (2017). Time-bin-encoded boson sampling with a single-photon device. *Physical Review Letters*, 118(19):190501.

Hillery, M., Bergou, J., and Feldman, E. (2003). Quantum walks based on an interferometric analogy. *Physical Review A*, 68(3):032314.

Holthaus, M. (2015). Floquet engineering with quasienergy bands of periodically driven optical lattices. *Journal of Physics B: Atomic, Molecular and Optical Physics*, 49(1):013001.

Hong, C. K., Ou, Z., and Mandel, L. (1987). Measurement of subpicosecond time intervals between two photons by interference. *Physical Review Letters*, 59(18):2044.

Horodecki, P. (1997). Separability criterion and inseparable mixed states with positive partial transposition. *Physics Letters A*, 232(5):333–339.

Kempe, J. (2003). Quantum random walks: an introductory overview. *Contemporary Physics*, 44(4):307–327.

Kempe, J. (2005). Discrete quantum walks hit exponentially faster. *Probability Theory and Related Fields*, 133(2):215–235.

Kiess, T., Shih, Y., Sergienko, A., and Alley, C. (1993). Einstein-podolsky-rosen-bohm experiment using pairs of light quanta produced by type-ii parametric down-conversion. *Physical Review Letters*, 71(24):3893.

Kim, T., Fiorentino, M., and Wong, F. N. (2006). Phase-stable source of polarization-entangled photons using a polarization sagnac interferometer. *Physical Review A*, 73(1):012316.

Kitaev, A. (2009). Periodic table for topological insulators and superconductors. In *AIP conference proceedings*, volume 1134, pages 22–30. American Institute of Physics.

Kitagawa, T. (2012). Topological phenomena in quantum walks: elementary introduction to the physics of topological phases. *Quantum Information Processing*, 11(5):1107–1148.

Kitagawa, T., Berg, E., Rudner, M., and Demler, E. (2010a). Topological characterization of periodically driven quantum systems. *Physical Review B*, 82(23):235114.

Kitagawa, T., Broome, M. A., Fedrizzi, A., Rudner, M. S., Berg, E., Kassal, I., Aspuru-Guzik, A., Demler, E., and White, A. G. (2012). Observation of topologically protected bound states in photonic quantum walks. *Nature Communications*, 3:882.

Kitagawa, T., Rudner, M. S., Berg, E., and Demler, E. (2010b). Exploring topological phases with quantum walks. *Physical Review A*, 82(3):033429.

Klitzing, K. v., Dorda, G., and Pepper, M. (1980). New method for high-accuracy determination of the fine-structure constant based on quantized hall resistance. *Physical Review Letters*, 45(6):494.

Klyshko, D. N., Penin, A. N., and Polkovnikov, B. F. (1970). Parametric luminescence and light scattering by polaritons. *JETP Letters*, 11:5.

Knight, P. L., Roldán, E., and Sipe, J. (2003a). Quantum walk on the line as an interference phenomenon. *Physical Review A*, 68(2):020301.

Knight, P. L., Roldán, E., and Sipe, J. E. (2003b). Optical cavity implementations of the quantum walk. *Optics Communications*, 227(1-3):147–157.

Knill, E., Laflamme, R., and Milburn, G. J. (2001). A scheme for efficient quantum computation with linear optics. *Nature*, 409(6816):46.

Kowalevicz, A., Sharma, V., Ippen, E., Fujimoto, J. G., and Minoshima, K. (2005). Three-dimensional photonic devices fabricated in glass by use of a femtosecond laser oscillator. *Optics Letters*, 30(9):1060–1062.

Krovi, H. and Brun, T. A. (2006). Hitting time for quantum walks on the hypercube. *Physical Review A*, 73(3):032341.

Kwiat, P. G., Mattle, K., Weinfurter, H., Zeilinger, A., Sergienko, A. V., and Shih, Y. (1995). New high-intensity source of polarization-entangled photon pairs. *Physical Review Letters*, 75(24):4337.

Laughlin, R. B. (1981). Quantized hall conductivity in two dimensions. *Physical Review B*, 23(10):5632.

Laughlin, R. B. (1983). Anomalous quantum hall effect: an incompressible quantum fluid with fractionally charged excitations. *Physical Review Letters*, 50(18):1395.

Lim, Y. L. and Beige, A. (2005). Generalized hong–ou–mandel experiments with bosons and fermions. *New Journal of Physics*, 7(1):155.

Longhi, S. (2013). Zak phase of photons in optical waveguide lattices. *Optics letters*, 38(19):3716–3719.

Loudon, R. (2000). *The quantum theory of light*. OUP Oxford.

Lovett, N. B., Cooper, S., Everitt, M., Trevers, M., and Kendon, V. (2010). Universal quantum computation using the discrete-time quantum walk. *Physical Review A*, 81(4):042330.

Lu, C.-Y., Zhou, X.-Q., Gühne, O., Gao, W.-B., Zhang, J., Yuan, Z.-S., Goebel, A., Yang, T., and Pan, J.-W. (2007). Experimental entanglement of six photons in graph states. *Nature physics*, 3(2):91–95.

Lu, L., Joannopoulos, J. D., and Soljačić, M. (2014). Topological photonics. *Nature photonics*, 8(11):821–829.

Lu, L., Joannopoulos, J. D., and Soljačić, M. (2016). Topological states in photonic systems. *Nature Physics*, 12(7):626–629.

Magniez, F. and Nayak, A. (2007). Quantum complexity of testing group commutativity. *Algorithmica*, 48(3):221–232.

Magniez, F., Santha, M., and Szegedy, M. (2007). Quantum algorithms for the triangle problem. *SIAM Journal on Computing*, 37(2):413–424.

Mair, A., Vaziri, A., Weihs, G., and Zeilinger, A. (2001). Entanglement of the orbital angular momentum states of photons. *Nature*, 412(6844):313–316.

McMillan, A., Labonté, L., Clark, A., Bell, B., Alibart, O., Martin, A., Wadsworth, W., Tanzilli, S., and Rarity, J. (2013). Two-photon interference between disparate sources for quantum networking. *Scientific reports*, 3(1):1–5.

Meany, T., Delanty, M., Gross, S., Marshall, G. D., Steel, M. J., and Withford, M. J. (2012). Non-classical interference in integrated 3d multiports. *Optics Express*, 20(24):26895–26905.

Menssen, A. J., Jones, A. E., Metcalf, B. J., Tichy, M. C., Barz, S., Kolthammer, W. S., and Walmsley, I. A. (2017). Distinguishability and many-particle interference. *Physical Review Letters*, 118(15):153603.

Metcalf, B. J., Thomas-Peter, N., Spring, J. B., Kundys, D., Broome, M. A., Humphreys, P. C., Jin, X.-M., Barbieri, M., Kolthammer, W. S., Gates, J. C., Smith, B. J., Langford, N. K., Smith, P. G. R., and Walmsley, I. A. (2013). Multiphoton quantum interference in a multiport integrated photonic device. *Nature Communications*, 4:1356.

Molesky, S., Lin, Z., Piggott, A. Y., Jin, W., Vucković, J., and Rodriguez, A. W. (2018). Inverse design in nanophotonics. *Nature Photonics*, 12(11):659–670.

Moore, C. and Russell, A. (2002). Quantum walks on the hypercube. In *RANDOM 2002: Randomization and Approximation Techniques in Computer Science*, pages 164–178. Springer.

Morimoto, T. and Furusaki, A. (2013). Topological classification with additional symmetries from clifford algebras. *Physical Review B*, 88(12):125129.

Motes, K. R., Olson, J. P., Rabeaux, E. J., Dowling, J. P., Olson, S. J., and Rohde, P. P. (2015). Linear optical quantum metrology with single photons: exploiting spontaneously generated entanglement to beat the shot-noise limit. *Physical Review Letters*, 114(17):170802.

Motwani, R. and Raghavan, P. (1996). Randomized algorithms. *ACM Computing Surveys*, 28(1):33–37.

Moulieras, S., Lewenstein, M., and Puentes, G. (2013). Entanglement engineering and topological protection by discrete-time quantum walks. *Journal of Physics B: Atomic, Molecular and Optical Physics*, 46(10):104005.

Murnaghan, F. D. (1962). *The unitary and rotation groups*, volume 3. Lectures on Applied Mathematics. Washington, DC: Spartan Books.

Nielsen, M. A. and Chuang, I. (2002). *Quantum computation and quantum information*. Cambridge University Press, New York.

Nikolopoulos, G. M. (2008). Directional coupling for quantum computing and communication. *Physical Review Letters*, 101(20):200502.

Nitsche, T., Elster, F., Novotnỳ, J., Gábris, A., Jex, I., Barkhofen, S., and Silberhorn, C. (2016). Quantum walks with dynamical control: graph engineering, initial state preparation and state transfer. *New Journal of Physics*, 18(6):063017.

Obuse, H., Asbóth, J. K., Nishimura, Y., and Kawakami, N. (2015). Unveiling hidden topological phases of a one-dimensional hadamard quantum walk. *Physical Review B*, 92(4):045424.

Osawa, S., Simon, D. S., and Sergienko, A. V. (2018). Experimental demonstration of a directionally-unbiased linear-optical multiport. *Optics Express*, 26(21):27201–27211.

Osawa, S., Simon, D. S., and Sergienko, A. V. (2019). Directionally-unbiased unitary optical devices in discrete-time quantum walks. *Entropy*, 21(9):853.

Osawa, S., Simon, D. S., and Sergienko, A. V. (2020). Higher-dimensional hong-ou-mandel effect and state redistribution with linear-optical multiports. *Physical Review A*, 102(6):063712.

Ou, Z. and Mandel, L. (1988). Violation of bell's inequality and classical probability in a two-photon correlation experiment. *Physical Review Letters*, 61(1):50.

Ozawa, T. and Carusotto, I. (2014). Anomalous and quantum hall effects in lossy photonic lattices. *Physical Review Letters*, 112(13):133902.

Pandey, D., Satapathy, N., Meena, M., and Ramachandran, H. (2011). Quantum walk of light in frequency space and its controlled dephasing. *Physical Review A*, 84(4):042322.

Perets, H. B., Lahini, Y., Pozzi, F., Sorel, M., Morandotti, R., and Silberberg, Y. (2008). Realization of quantum walks with negligible decoherence in waveguide lattices. *Physical Review Letters*, 100(17):170506.

Perez-Leija, A., Keil, R., Kay, A., Moya-Cessa, H., Nolte, S., Kwek, L.-C., Rodríguez-Lara, B. M., Szameit, A., and Christodoulides, D. N. (2013). Coherent quantum transport in photonic lattices. *Physical Review A*, 87(1):012309.

Peruzzo, A., Laing, A., Politi, A., Rudolph, T., and O'brien, J. L. (2011). Multimode quantum interference of photons in multiport integrated devices. *Nature Communications*, 2:224.

Peruzzo, A., Lobino, M., Matthews, J. C., Matsuda, N., Politi, A., Poulios, K., Zhou, X.-Q., Lahini, Y., Ismail, N., Wörhoff, K., et al. (2010). Quantum walks of correlated photons. *Science*, 329(5998):1500–1503.

Poem, E., Gilead, Y., and Silberberg, Y. (2012). Two-photon path-entangled states in multimode waveguides. *Physical Review Letters*, 108(15):153602.

Portugal, R. (2013). *Quantum walks and search algorithms*. Springer Science & Business Media.

Poyatos, J., Cirac, J. I., and Zoller, P. (1997). Complete characterization of a quantum process: the two-bit quantum gate. *Physical Review Letters*, 78(2):390.

Rakovszky, T. and Asboth, J. K. (2015). Localization, delocalization, and topological phase transitions in the one-dimensional split-step quantum walk. *Physical Review A*, 92(5):052311.

Rechtsman, M. C., Lumer, Y., Plotnik, Y., Perez-Leija, A., Szameit, A., and Segev, M. (2016). Topological protection of photonic path entanglement. *Optica*, 3(9):925–930.

Reck, M., Zeilinger, A., Bernstein, H. J., and Bertani, P. (1994). Experimental realization of any discrete unitary operator. *Physical Review Letters*, 73(1):58.

Ribeiro, P. S., Walborn, S., Raitz Jr, C., Davidovich, L., and Zagury, N. (2008). Quantum random walks and wave-packet reshaping at the single-photon level. *Physical Review A*, 78(1):012326.

Roy, R. and Harper, F. (2017). Periodic table for floquet topological insulators. *Physical Review B*, 96(15):155118.

Ryu, S. and Hatsugai, Y. (2002). Topological origin of zero-energy edge states in particle-hole symmetric systems. *Physical Review Letters*, 89(7):077002.

Ryu, S., Schnyder, A. P., Furusaki, A., and Ludwig, A. W. (2010). Topological insulators and superconductors: tenfold way and dimensional hierarchy. *New Journal of Physics*, 12(6):065010.

Saleh, A. and Kogelnik, H. (1988). Reflective single-mode fiber-optic passive star couplers. *Journal of Lightwave Technology*, 6(3):392–398.

Saleh, B. E., Teich, M. C., and Saleh, B. E. (1991). *Fundamentals of photonics*. Wiley New York.

Sansoni, L., Sciarrino, F., Vallone, G., Mataloni, P., Crespi, A., Ramponi, R., and Osellame, R. (2012). Two-particle bosonic-fermionic quantum walk via integrated photonics. *Physical Review Letters*, 108(1):010502.

Schreiber, A., Cassemiro, K. N., Potoček, V., Gábris, A., Mosley, P. J., Andersson, E., Jex, I., and Silberhorn, C. (2010). Photons walking the line: a quantum walk with adjustable coin operations. *Physical Review Letters*, 104(5):050502.

Schreiber, A., Gábris, A., Rohde, P. P., Laiho, K., Štefaňák, M., Potoček, V., Hamilton, C., Jex, I., and Silberhorn, C. (2012). A 2d quantum walk simulation of two-particle dynamics. *Science*, 336(6077):55–58.

Schwelb, O. (1998). Generalized analysis for a class of linear interferometric networks. i. analysis. *IEEE Transactions on Microwave Theory and Techniques*, 46(10):1399–1408.

Shi, Z.-Y., Tang, H., Feng, Z., Wang, Y., Li, Z.-M., Gao, J., Chang, Y.-J., Wang, T.-Y., Dou, J.-P., Zhang, Z.-Y., et al. (2020). Quantum fast hitting on glued trees mapped on a photonic chip. *Optica*, 7(6):613–618.

Shor, P. W. (1994). Algorithms for quantum computation: discrete logarithms and factoring. In *Proceedings 35th annual symposium on foundations of computer science*, pages 124–134. Ieee.

Shor, P. W. (1999). Polynomial-time algorithms for prime factorization and discrete logarithms on a quantum computer. *SIAM review*, 41(2):303–332.

Simon, D., Osawa, S., and Sergienko, A. V. (2020). Quantum-clustered two-photon walks. *Physical Review A*, 101(3):032118.

Simon, D. S. (2018). *Tying Light in Knots*. Morgan & Claypool Publishers.

Simon, D. S., Fitzpatrick, C. A., Osawa, S., and Sergienko, A. V. (2017a). Quantum simulation of discrete-time hamiltonians using directionally unbiased linear optical multiports. *Physical Review A*, 95(4):042109.

Simon, D. S., Fitzpatrick, C. A., Osawa, S., and Sergienko, A. V. (2017b). Quantum simulation of topologically protected states using directionally unbiased linear-optical multiports. *Physical Review A*, 96(1):013858.

Simon, D. S., Fitzpatrick, C. A., and Sergienko, A. V. (2016). Group transformations and entangled-state quantum gates with directionally unbiased linear-optical multiports. *Physical Review A*, 93(4):043845.

Simon, D. S., Osawa, S., and Sergienko, A. V. (2018a). Joint entanglement of topology and polarization enables error-protected quantum registers. *New Journal of Physics*, 20(9):093032.

Simon, D. S., Osawa, S., and Sergienko, A. V. (2018b). Topological boundaries and bulk wavefunctions in the su–schreiffer–heeger model. *Journal of Physics: Condensed Matter*, 31(4):045001.

Spagnolo, N., Aparo, L., Vitelli, C., Crespi, A., Ramponi, R., Osellame, R., Mataloni, P., and Sciarrino, F. (2012). Quantum interferometry with three-dimensional geometry. *Scientific Reports*, 2:862.

Spagnolo, N., Vitelli, C., Aparo, L., Mataloni, P., Sciarrino, F., Crespi, A., Ramponi, R., and Osellame, R. (2013a). Three-photon bosonic coalescence in an integrated tritter. *Nature Communications*, 4:1606.

Spagnolo, N., Vitelli, C., Sansoni, L., Maiorino, E., Mataloni, P., Sciarrino, F., Brod, D. J., Galvão, E. F., Crespi, A., Ramponi, R., and Osellame, R. (2013b). General rules for bosonic bunching in multimode interferometers. *Physical Review Letters*, 111(13):130503.

Spring, J. B., Metcalf, B. J., Humphreys, P. C., Kolthammer, W. S., Jin, X. M., Barbieri, M., Datta, A., Thomas-Peter, N., Langford, N. K., Kundys, D., Gates, J. C., Smith, B. J., Smith, P. G. R., and Walmsley, I. A. (2013). Boson sampling on a photonic chip. *Science*, 339(6121):798–801.

Stanescu, T. D. (2016). *Introduction to topological quantum matter & quantum computation*. CRC Press.

Štefaňák, M. and Skoupỳ, S. (2016). Perfect state transfer by means of discrete-time quantum walk search algorithms on highly symmetric graphs. *Physical Review A*, 94(2):022301.

Su, Q.-P., Zhang, Y., Yu, L., Zhou, J.-Q., Jin, J.-S., Xu, X.-Q., Xiong, S.-J., Xu, Q., Sun, Z., Chen, K., et al. (2019). Experimental demonstration of quantum walks with initial superposition states. *npj Quantum Information*, 5(1):1–7.

Su, W., Schrieffer, J., and Heeger, A. J. (1979). Solitons in polyacetylene. *Physical Review Letters*, 42(25):1698.

Su, W.-P., Schrieffer, J., and Heeger, A. (1980). Soliton excitations in polyacetylene. *Physical Review B*, 22(4):2099.

Suzuki, K., Sharma, V., Fujimoto, J. G., Ippen, E. P., and Nasu, Y. (2006). Characterization of symmetric [3× 3] directional couplers fabricated by direct writing with a femtosecond laser oscillator. *Optics Express*, 14(6):2335–2343.

Tang, H., Di Franco, C., Shi, Z.-Y., He, T.-S., Feng, Z., Gao, J., Sun, K., Li, Z.-M., Jiao, Z.-Q., Wang, T.-Y., and Kim, M. S.and Jin, X.-M. (20018). Experimental quantum fast hitting on hexagonal graphs. *Nature Photonics*, 12:754–758.

Tang, H., Lin, X.-F., Feng, Z., Chen, J.-Y., Gao, J., Sun, K., Wang, C.-Y., Lai, P.-C., Xu, X.-Y., Wang, Y., et al. (2018). Experimental two-dimensional quantum walk on a photonic chip. *Science Advances*, 4(5):eaat3174.

Tarasinski, B., Asbóth, J., and Dahlhaus, J. (2014). Scattering theory of topological phases in discrete-time quantum walks. *Physical Review A*, 89(4):042327.

Thouless, D. (1983). Quantization of particle transport. *Physical Review B*, 27(10):6083.

Tichy, M., Lim, H. T., Ra, Y. S., Mintert, F., Kim, Y. H., and Buchleitner, A. (2011). Four-photon indistinguishability transition. *Physical Review A*, 83(6):062111.

Tillmann, M., Dakić, B., Heilmann, R., Nolte, S., Szameit, A., and Walther, P. (2013). Experimental boson sampling. *Nature Photonics*, 7(7):540.

Tillmann, M., Tan, S., Stoeckl, S. E., Sanders, B. C., de Guise, H., Heilmann, R., Nolte, S., Szameit, A., and Walther, P. (2015). Generalized multiphoton quantum interference. *Physical Review X*, 5(4):041015.

Tregenna, B., Flanagan, W., Maile, R., and Kendon, V. (2003). Controlling discrete quantum walks: coins and initial states. *New Journal of Physics*, 5(1):83.

Tsui, D. C., Stormer, H. L., and Gossard, A. C. (1982). Two-dimensional magnetotransport in the extreme quantum limit. *Physical Review Letters*, 48(22):1559.

Tulsi, A. (2008). Faster quantum-walk algorithm for the two-dimensional spatial search. *Physical Review A*, 78(1):012310.

Vance, R. and Barrow, R. (1995). General linear differential interferometers. *Journal of the Optical Society of America A*, 12(2):346–353.

Venancio, B., Andrade, F., and da Luz, M. (2013). Unveiling and exemplifying the unitary equivalence of discrete time quantum walk models. *Journal of Physics A*, 46(16):165302.

Venegas-Andraca, S. E. (2012). Quantum walks: a comprehensive review. *Quantum Information Processing*, 11(5):1015–1106.

Walborn, S. P., Oliveira, A. N. D., Pádua, S., and Monken, C. H. (2003). Multimode hong-ou-mandel interference. *Physical Review Letters*, 90(14):143601.

Wang, H., Qin, J., Ding, X., Chen, M. C., Chen, S., You, X., He, Y. M., Jiang, X., You, L., Wang, Z., Schneider, C., Jelmer, J. R., Höfling, S., Lu, C. Y., and Pan, J. W. (2019). Boson sampling with 20 input photons and a 60-mode interferometer in a 1 0 14-dimensional hilbert space. *Physical Review Letters*, 123(25):250503.

Wang, J. Paesani, S., Ding, Y., Santagati, R., Skrzypczyk, P., Salavrakos, A., Tura, J., Augusiak, R., Mančinska, L., Bacco, D., et al. (2018). Multidimensional quantum entanglement with large-scale integrated optics. *Science*, page eaar7053.

Weihs, G., Reck, M., Weinfurter, H., and Zeilinger, A. (1996a). All-fiber three-path mach–zehnder interferometer. *Optics Letters*, 21(4):302–304.

Weihs, G., Reck, M., Weinfurter, H., and Zeilinger, A. (1996b). Two-photon interference in optical fiber multiports. *Physical Review A*, 54(1):893.

Werner, A. H., Jaschke, D., Silvi, P., Kliesch, M., Calarco, T., Eisert, J., and Montangero, S. (2016). Positive tensor network approach for simulating open quantum many-body systems. *Physical Review Letters*, 116(23):237201.

Wootters, W. K. and Zurek, W. H. (1982). A single quantum cannot be cloned. *Nature*, 299(5886):802–803.

Zak, J. (1989). Berry's phase for energy bands in solids. *Physical Review Letters*, 62(23):2747.

Zeilinger, A., Horne, M. A., Weinfurter, H., and Żukowski, M. (1997). Three-particle entanglements from two entangled pairs. *Physical Review Letters*, 78(16):3031.

Zhan, X., Qin, H., Bian, Z., Li, J., and Xue, P. (2014). Perfect state transfer and efficient quantum routing: A discrete-time quantum-walk approach. *Physical Review A*, 90(1):012331.

Zhang, J.-G., Sharma, A., Ni, Y.-D., and Li, Z. (2000). Investigation into network architecture and modulation scheme for mil-std-1773 optical fiber data buses. *Aircraft Engineering and Aerospace Technology*, 72(2):126–137.

Zhang, P., Ren, X.-F., Zou, X.-B., Liu, B.-H., Huang, Y.-F., and Guo, G.-C. (2007). Demonstration of one-dimensional quantum random walks using orbital angular momentum of photons. *Physical Review A*, 75(5):052310.

Zhang, Y., Roux, F. S., Konrad, T., Agnew, M., Leach, J., and Forbes, A. (2016). Engineering two-photon high-dimensional states through quantum interference. *Science Advances*, 2(2):e1501165.

Zhao, Z., Du, J., Li, H., Yang, T., Chen, Z.-B., and Pan, J.-W. (2002). Implement quantum random walks with linear optics elements. *arXiv preprint quant-ph/0212149*.

Zhong, H.-S., Li, Y., Li, W., Peng, L.-C., Su, Z.-E., Hu, Y., He, Y.-M., Ding, X., Zhang, W., Li, H., et al. (2018). 12-photon entanglement and scalable scattershot boson sampling with optimal entangled-photon pairs from parametric down-conversion. *Physical Review Letters*, 121(25):250505.

Żukowski, M., Zeilinger, A., and Horne, M. (1997). Realizable higher-dimensional two-particle entanglements via multiport beam splitters. *Physical Review A*, 55(4):2564.

CURRICULUM VITAE